

Computational Fluid Dynamics Based Optimisation of Emergency Response Vehicles

Ali Reza Taherkhani

Submitted in accordance with the requirements for the degree of
Doctor of Philosophy

The University of Leeds
School of Mechanical Engineering

March, 2015

The candidate confirms that the work submitted is his own and that appropriate credit has been given where reference has been made to the work of others.

This copy has been supplied on the understanding that it is copyright material and that no quotation from the thesis may be published without proper acknowledgement.

Acknowledgements

The research documented within this thesis would not have been possible without the contribution of a number of people. Firstly, I would like to acknowledge the tremendous input of my four supervisors, Harvey Thompson, Vassili Toropov, Phil Gaskell and Dr Rob Hewson. Their support, encouragement, experience and vision were instrumental in giving me the confidence and direction to achieve the objectives of the work described herein.

All the way through the project, from start to the end, Professor Harvey Thompson was very supportive, understanding and caring. His enthusiasm, expertise and insight led to the successful application of this fascinating field of engineering to the problem described shortly. I will forever be thankful to him. He was and will be my best role model in my life. I would like to thank my brother, Hamid for his incredible support over many years, including those dedicated to this thesis. He made my life so much easier as I undertook the tremendous challenge of working towards the PhD and for this I am extremely grateful.

A number of friends including Carl Gilkeson, Andrey Polynkin, Zinedine Khatir, Gregory de Boer, Amirul Khan and James Eves, were fantastic throughout. They have been very helpful and supportive. They always provided suggestions and answered many questions that I had over the course this project. I really feel blessed to have such people around me.

In the final months of writing this thesis whilst doing a postdoctoral fellowship in the School of Mechanical Engineering, my Supervisors, professor Harvey Thompson and professor Nik Kapur were tremendously supportive and patient. This allowed me to produce the best possible piece of work.

Abstract

Formal optimisation studies of the aerodynamic design of Emergency Response Vehicles, typically encountered within the United Kingdom, were undertaken. The objectives of the study were to optimise the aerodynamics of the Emergency Response Vehicles such as Ambulance and Police cars, in terms of drag force.

A combination of wind tunnel tests and the Computational Fluid Dynamics (CFD) simulations were used to analyse the flow field and aerodynamic characteristics of Emergency Response Vehicles. The experimental data were used to validate the computer simulations and the good agreement observed gave confidence in the results obtained. Results from computer simulations on the scale models and full-scale models, were also characteristically similar to those of the validated scale model.

Computational Fluid Dynamics (CFD) was combined with an efficient optimisation framework to minimize the drag force of three different types of Emergency Response Vehicles, Ambulance Van Conversion, Police Van Conversion and Police Sedan car Conversion. The benefits of employing an airfoil-based roof design and Bezier curve fitting approach which minimizes the deleterious aerodynamic effects of the required front and rear light-bars, were investigated. Optimal Latin Hypercube (OLH) Design of Experiments, the Multipoint Approximation Method (MAM) and surrogate modelling were used for the optimisation.

Optimisation results demonstrated a clear improvement of the aerodynamic design of the Emergency Response Vehicles named above. It was also clearly demonstrated that improving the aerodynamic design of Emergency Response Vehicles roof offers a significant opportunity for reducing the fuel consumption and emissions for Emergency Response Vehicles.

Contents

Acknowledgements.....	ii
Abstract.....	iii
Tables.....	ix
Figures.....	xi
Abbreviations.....	xvii
Nomenclature.....	xix
1. Introduction.....	1
2. State of The Art.....	4
2.1. Background.....	4
2.2. Literature Review.....	6
2.3. Main Focus.....	23
3. Vehicle Aerodynamics.....	25
3.1. Fundamentals.....	25
3.1.1. Governing Equations.....	25
3.1.2. Reynolds Number.....	26
3.1.3. Energy Cascade.....	27
3.1.4. Laminar and Turbulent flow.....	27
3.1.5. Boundary layers.....	29
3.1.6. Pressure Gradient and Flow Separation.....	30
3.1.7. Drag or shape factor.....	31
3.2. Flow Separation Control.....	37
3.2.1. Flow Control Methods.....	37
3.2.2. Advantage of Flow Control.....	39
3.2.3. Passive drag reduction.....	39
3.3. Fuel Consumptions.....	41
3.4. Three-Dimensional Flow (Airflow Pattern).....	41
3.4.1. Pressure Distribution.....	42
3.5. Summary.....	43
4. Computational Fluid Dynamics.....	44
4.1. CFD.....	44
4.1.1. Discretisation.....	45
4.1.2. The Finite Difference Method.....	45
4.1.3. The Finite Element Method.....	45
4.1.4. The Finite Volume Method.....	46

4.1.5.	Pressure-Velocity Coupling.....	47
4.1.6.	Differencing Schemes and Accuracy.....	48
4.2.	Grid Generation.....	48
4.2.1.	Body-fitted Grids.....	49
4.2.2.	Structured Grids.....	49
4.2.3.	Unstructured Grids.....	50
4.2.4.	Good Practice.....	51
4.3.	CAD Models.....	51
4.4.	Boundary Conditions.....	52
4.4.1.	Inlet, Outlet and Symmetry Planes.....	52
4.4.2.	Walls.....	53
4.4.3.	Turbulence Intensity.....	56
4.4.4.	Turbulence Length Scale.....	57
4.5.	Turbulence Modelling.....	57
4.5.1.	Direct Numerical Simulation (DNS).....	58
4.5.2.	Large Eddy Simulation (LES).....	59
4.5.3.	Detached Eddy Simulations (DES).....	59
4.5.4.	Reynolds-Averaged Navier-Stokes (RANS) Equation.....	59
4.5.5.	Efficiency vs. Accuracy.....	63
4.5.6.	The $k-\omega$ Model.....	64
4.5.7.	The Spalart-Allmaras Model.....	65
4.5.8.	The Standard $k-\varepsilon$ Model.....	66
4.5.9.	Realisable $k-\varepsilon$ Model.....	68
4.5.10.	The RNG $k-\varepsilon$ Model.....	69
4.6.	Numerical Noise and Convergence Tolerance.....	69
4.7.	Error and Uncertainty in CFD.....	71
4.8.	Verification and Validation.....	72
5.	Design Optimisation.....	74
5.1.	Optimisation process.....	74
5.2.	Design of Experiments (DoEs).....	74
5.2.1.	Design vector.....	75
5.2.2.	Sampling.....	76
5.2.3.	Random Sampling.....	77
5.2.4.	Full Factorial Sampling.....	77
5.2.5.	Latin Hypercube Sampling.....	78

5.3.	Response Surface Methods (RSM)	81
5.3.1.	Kriging	83
5.3.2.	Least Square Method.....	84
5.3.3.	Moving Least Square Method.....	85
5.4.	Optimisation Techniques	87
5.4.1.	Design constraints	88
5.4.2.	Objective function.....	89
5.5.	Optimisation Approaches	90
5.5.1.	Deterministic optimisation approaches	91
5.5.2.	Stochastic optimisation approaches	91
5.6.	Optimisation Methods.....	92
5.6.1.	Sequential Quadratic programming (SQP)	92
5.6.2.	Multi Approximation Method (MAM).....	92
5.6.3.	Genetic Algorithm.....	93
6.	CFD and Experimental Validation Study of Emergency Response	
	Vehicles	98
6.1.	Experimental techniques.....	98
6.1.1.	Wind Tunnel Approach	98
6.1.2.	Different Types of Wind Tunnels.....	98
6.2.	Factors affecting the accuracy of the wind tunnel testing.....	100
6.2.1.	The Scale or Reynolds number effect	100
6.2.2.	Road moves relative to the car instead of car moving.....	102
6.2.3.	The ground board method	102
6.2.4.	The moving belt method	103
6.2.5.	Blockage effects.....	104
6.2.6.	Importance of Modelling Fine Detail.....	105
6.3.	Flow Measurement and Visualisation.....	105
6.4.	Wind Tunnel Experiment.....	107
6.4.1.	The Queen Mary Wind Tunnel	109
6.4.2.	Experimental Methodology	110
6.5.	Experimental Results	111
6.5.1.	Flow Visualisation	115
6.6.	CFD Validations.....	116
6.6.1.	Inlet and outlet sensitivity	118
6.6.2.	Grid Independence Study.....	119
6.6.3.	Y ⁺ analysis	120

6.6.4.	Turbulence Model Performance	120
6.6.5.	CFD Simulation Flow Behaviour	124
6.7.	Conclusion	126
7.	Design Optimisation of Emergency Response Vehicle	128
7.1.	Problem Formulation	129
7.1.1.	Objective function and Parameterisation	129
7.2.	Ambulance Van-conversion	129
7.2.1.	CFD Optimisation Methodology	130
7.2.2.	CFD Modelling	131
7.2.3.	Boundary Conditions	132
7.2.4.	Ambulance Conversion Schemes	133
7.2.5.	Optimisation Problem Formulation	134
7.2.6.	Definition of the Design Variables	136
7.2.7.	Optimisation Method	137
7.2.8.	Optimisation Results	138
7.2.9.	Practical Application	139
7.2.10.	New Roof Design and Aerodynamic Performance	140
7.3.	Police Van-conversion	142
7.3.1.	CFD Modelling	143
7.3.2.	Boundary Condition and Mesh Generation	144
7.3.3.	Model Configuration	144
7.3.4.	Model Parameterisation	145
7.3.5.	Optimisation Method and Strategies	145
7.3.6.	Optimisation Results	146
7.4.	Police BMW 5series-conversion	150
7.4.1.	CFD Modelling	150
7.4.2.	Turbulence Model Comparison	151
7.4.3.	Model ConFfiguration	152
7.4.4.	Parametric Study	153
7.4.5.	Model Parameterisation	156
7.4.6.	Optimisation method and Results	157
7.6.	Concluding Remarks	165
8.	Discussion and Conclusions	166
8.1.	Validation	166
8.2.	Emergency Response Vehicles Design Optimisation	167

8.3. Optimization Techniques.....	167
8.4. Results	168
8.5. Fuel Consumption.....	169
8.6. Future work	170
8.7. Conclusion.....	171
9. References	173

Tables

- Table 3.1 Relationship between drag reductions and fuel economy improvement for tractor trailer trucks [16]
- Table 4.1 Summary of turbulence strategies for the 3D flow past an aeroplane or vehicle [43]
- Table 6.1 Different velocities with the corresponding Reynolds numbers
- Table 6.2 Average drag force for all models for 13 m/s
- Table 6.3 Average drag force for all models for 20.55 m/s
- Table 6.4 Average drag force for all models for 22.51 m/s
- Table 6.5 Average drag force for all models for 26.64 m/s
- Table 6.6 Drag force results of the mesh grid size and turbulent models comparison for baseline model for 26m/s
- Table 6.7 Comparison of the drag force and coefficients of the fine mesh density for different turbulent models for all models with add-ons for 26m/s.
- Table 6.8 Comparison of the drag force results of the medium mesh density for different turbulent models for all models with add-ons for 26 m/s.
- Table 6.9 Comparison of the experimental drag coefficient
- Table 7.1 Boundary conditions applied for the generic ambulance model
- Table 7.2 Boundary constraints on the design variables
- Table 7.3 Drag comparison for the original and optimised designs
- Table 7.4 Aerodynamic performance for the original and optimised conversion designs
- Table 7.5 Comparison of the responses obtained from the optimisation and CFD
- Table 7.6 Drag comparison for the original and optimised design
- Table 7.7 Drag coefficients for different turbulent models
- Table 7.8 Drag forces comparison for car with and without light bar
- Table 7.9 Results of parametric study
- Table 7.10 Results for the height of light bar study
- Table 7.11 Comparison of the responses obtained from the optimisation and CFD
- Table 7.12 Drag comparison for the original and optimised design
- Table 7.13 Drag force and coefficient for different Velocities for optimum design

Table 7.14 Comparison of the Drag force results of the medium mesh density for different turbulent models for the optimised model for 26 m/s.

Table 7.15 Comparison of the experimental drag coefficient

Table 8.1 Drag comparison of base-line, original and optimized Fiat ambulance van conversion

Table 8.2 Drag comparison of base-line, original and optimized Fiat ambulance van conversion

Table 8.3 Drag comparison of base-line, original and optimized Fiat ambulance van conversion

Table 8.4 Relationship between drag reductions and fuel economy improvement for tractor-trailer trucks [16]

Table 8.5 Drag and Fuel consumption reductions for optimised Emergency Response Vehicles

Figures

- Figure 1.1 Side view of a Fiat ambulance (courtesy of P. Occardi)
- Figure 1.2 Side view of a Vauxhall Police van [4]
- Figure 1.3 BMW Police car [13]
- Figure 2.1 Resistance force requirement versus vehicle speed for HGV [16]
- Figure 2.2 Graphic depicting the distribution of aerodynamic drag for a heavy vehicle tractor-trailer truck, with and without aerodynamic fairings, operating in a zero crosswind condition [16]
- Figure 2.3 Sketch of a side view of the vortex strake trailer base wake flow characteristics for a typical tractor-trailer truck with the base treatment installed [16]
- Figure 2.4 Description of the VGs geometry with the typical dimensions characterizing the device used in the experiments, angle α is 60° in the sketch which will be varied in the study [27]
- Figure 2.5 Streamline of time and space averaged flow over a curved ramp a) without VG's b) with VG's. Dotted point is the position of the separation [28]
- Figure 2.6 Overall drag comparison between the benchmark and new design at different speeds [7]
- Figure 2.7 Time-averaged velocity fields in the vertical mid-plane for a) coarse and b) fine grids [36]
- Figure 2.8 PIV velocity field measurements in the vertical mid-plane [36]
- Figure 2.9 Depiction of slat optimisation parameters [39]
- Figure 2.10 Wake region without (Left) and with GA optimised slat (Right) [39]
- Figure 2.11 Illustration of the three design variables shaping the headboard fairing. A) Side view b) and aerial view [40]
- Figure 2.12 Surface contour plots of the pressure coefficient for the baseline trailer and the optimum fairing predicted by met model [40]
- Figure 2.13 Comparison between predicted and Measured aerodynamic drag [42].
- Figure 2.14 Comparison of the drag between CFD and test for new Lavidia [42].
- Figure 2.15 Bezier curves of various degree [44]
- Figure 2.16 Computational domain and boundary condition for railway analysis [77]
- Figure 2.17 Geometry of the nose [77]

- Figure 2.18 Influence of the parameter θ_{top} [77]
- Figure 2.19 Influence of the total nose length $a + b$ [77]
- Figure 2.20 Shape of the front of the train including the parameters [78].
- Figure 3.1 Example of turbulence (Visualisation of jet flow) [91]
- Figure 3.2 Illustration showing the structure of the boundary layer [92]
- Figure 3.3 Profile of boundary layer separation
- Figure 3.4 Drag force [98]
- Figure 3.5 Shear and pressure force on a vehicle [85]
- Figure 3.6 The variation of the velocity in a boundary layer [85]
- Figure 3.7 The effects of viscosity [85] (a) Theoretical flow pattern obtained when the effect of viscosity are ignored; (b) typical actual pattern for a real air flow.
- Figure 3.8 Illustrations showing the vortex structure around a vehicle [85]
- Figure 3.9 Image demonstrating the pressure recovery in the wake of the Don-Bur 'teardrop' design (Right) relative to a standard trailer (Left) [102]
- Figure 3.10 Effect of shape of the truck on the drag coefficient [29]
- Figure 3.11 Illustration showing the surface pressure distribution along the centreline of a vehicle [85]
- Figure 4.1 Illustration of the finite volume method for a two-dimensional grid [64].
- Figure 4.2 Schematic of (a) a simple body-fitted grid for flow past cylinders and (b) the computational grid onto which it is mapped (Own Figure)
- Figure 4.3 Illustration of a typical block structured grid (Own Figure)
- Figure 4.4 Illustration of triangular unstructured elements for a fluid domain surrounding an ellipse (Own Figure)
- Figure 4.5 Illustration of good practice meshing (Own Figure)
- Figure 4.6 Examples of CAD model geometry before and after repair
- Figure 4.7 Representation of Wall Function approach vs fully resolving the boundary layer [111]
- Figure 4.8 y^+ definition [113]
- Figure 4.9 Dimensionless velocity distribution for the inner region of a boundary layer [114]
- Figure 4.10 Instantaneous velocity measurements in laminar and turbulent flow [107]
- Figure 4.11 Graphical representation of the terms that appear on the right hand side of the equation [91]
- Figure 4.12 Comparison of computed flow fields around a cylinder for $Re = 50,000$ using various turbulence treatments. Experimental $C_D = 1.2$ [43]. Courtesy of Philippe Spalart, Boeing Commercial Airplanes.

- Figure 5.1 Optimisation process [124]
- Figure 5.2 Simple Full Factorial Designs [123]
- Figure 5.3 Latin Hypercube Sampling [123]
- Figure 5.4 Correlation reduction in Latin Hypercube Sampling [123]
- Figure 5.5 Comparison between LHS and OLHS for 100 design variables [97]
- Figure 5.6 Second order Response Surface Plot [9]
- Figure 5.7 Examples of Kriging and least square quadratic regression model [93]
- Figure 5.8 Constraint surface in a hypothetical two-dimensional design space [124]
- Figure 5.9 Contours of objective function [124]
- Figure 5.10 example of binary and real-number chromosome representation [144]
- Figure 5.11 Example of crossover operation for two different representations[144]
- Figure 5.12 Example of mutation operation for two chromosomes [144]
- Figure 5.13 Illustration of global and local maxima [94]
- Figure 6.1 Open Return Wind Tunnel [62]
- Figure 6.2 Closed Return Wind Tunnel [63]
- Figure 5.3 Schematic showing scale effects in vehicle aerodynamics [85]
- Figure 6.4 Principle of experiment, with stationary ground and wheel [18]
- Figure 6.5 Principle of the moving belt [148]
- Figure 6.6 Full-Scale Wind Tunnel Tests of Production and Prototype, Second-Generation Aerodynamic Drag-reducing Devices for Tractor-Trailers [153]
- Figure 6.7 Tufts visualisation on a real car [64]
- Figure 6.8 Real model of Vauxhall Vivaro [153]
- Figure 6.9 Generic Schematic of Queen Mary University of London Wind Tunnel
- Figure 6.10 Generic model of Vauxhall Vivaro
- Figure 6.11 Vehicle with light-bars, (a) CAD model, (b) Physical wind tunnel model
- Figure 6.12 Vehicle with flat light-bars, (a) CAD model, (b) Physical wind tunnel model
- Figure 6.13 Queen Mary University of London Wind tunnel
- Figure 6.14 Model inside the wind tunnel
- Figure 6.15 Model 3mm above the wind tunnel floor
- Figure 6.16 Wind tunnel contraction section

- Figure 6.17 Dimensions of Vauxhall Vivaro [113]
- Figure 6.18 Drag force for 100 readings for 26.64 m/s
- Figure 6.19 Drag force for all velocities for four models
- Figure 6.20 Drag Coefficient for all velocities for four models
- Figure 6.21 Flow visualisation using tufts for baseline model
- Figure 6.22 Flow visualisation using tufts for model with light-bars (rear view)
- Figure 6.23 Flow visualisation using tufts for model with light-bars (top view)
- Figure 6.24 Computational geometry of the wind tunnel domain including boundary conditions
- Figure 6.25 Geometry of the vehicle inside the wind tunnel above the floor
- Figure 6.26 Illustration showing the grid on the symmetry plane and top wall
- Figure 6.27 Illustration showing the grid around the vehicle
- Figure 6.28 Solution domain dimensions with extended inlet and outlet
- Figure 6.29 Drag force vs number of cells
- Figure 6.30 Contour of y^+ value for S-A turbulence model for a) fine mesh, b) medium mesh
- Figure 6.31 Turbulence and mesh grid density comparison with the experiment for the Baseline model
- Figure 6.32 Drag force comparison for the medium mesh density for different turbulent models for all models with add-ons
- Figure 6.33 Drag coefficients comparison for the medium mesh density for different turbulent models for all models with add-ons
- Figure 6.34 Behaviour of the flow in front and rear of the baseline model
- Figure 6.35 Velocity contour and streamline of the baseline model
- Figure 6.36 Pressure contour and streamline of the baseline model
- Figure 6.37 Velocity contour and streamline of the model with light-bars
- Figure 6.38 Pressure contour and streamline of the model with light-bars
- Figure 6.39 Closed view of the velocity contour around the light-bar and rear of the vehicle
- Figure 6.40 Velocity contour and streamline of the model with light-bars flat
- Figure 6.41 Pressure contour and streamline of the model with light-bars flat
- Figure 6.42 Close view of the velocity contour around the light-bar flat and rear of the vehicle
- Figure 7.1 Side view of a Fiat ambulance (courtesy of P. Occardi)
- Figure 7.2 Side view of a Vauxhall Police van [89]
- Figure 7.3 BMW Police car [13]
- Figure 7.4 Generic model of van-type vehicle

- Figure 7.5 Wind tunnel domain and its dimensions
- Figure 7.6 Mesh structure surrounding the vehicle
- Figure 7.7 Conversion schemes for a generic ambulance model: with detached rear (Conversion A, top picture) and front lights bars and with the integrated (under the roof) lights (Conversion B, bottom picture)
- Figure 7.8 The generic ambulance model with the airfoil and light bar concepts.
- Figure 7.9 The parameterisation scheme used for shape optimisation of the ambulance roof
- Figure 7.10 Ambulance roof shapes obtained with: (left) $\alpha_1 = -2$ degrees and (right) $\alpha_1 = 2$ degrees.
- Figure 7.11 The profiles of optimised designs of the generic model: Optimal 1 (above) and Optimal 2 (below)
- Figure 7.12 Examples of CAD model geometry
- Figure 7.13 Rear and front light-bars of the Fiat ambulance: actual (above) and CFD model (below).
- Figure 7.14 Ambulance roof profile based on airfoil design concept
- Figure 7.15 Pressure contours and velocity streamlines on the vehicle surface for the original (left) and optimised (right) design conversion.
- Figure 7.16 Velocity contours and streamlines for the original and airfoil based designs.
- Figure 7.17 Generic model based on Vauxhall Vivaro
- Figure 7.18 Van with light-bars Conversion A,(Original left), Conversion B(Right)
- Figure 7.19 Model with airfoil configuration
- Figure 7.20 Design parameters
- Figure 7.21 Distribution of normalised design points in the design variable space.
- Figure 7.22 Sample points minimum distance plot for model building, validation and total merged DoEs.
- Figure 7.23 Minimum Drag force in Response surface of the Response Surface Model
- Figure 7.24 Optimum configuration of the light-bars
- Figure 7.25 Contours of velocity for original and airfoil-based design
- Figure 7.26 Velocity streamlines for original and airfoil-based design
- Figure 7.27 Real model of BMW 5series
- Figure 7.28 Wind tunnel domain
- Figure 7.29 Illustration of the mesh type and size around the vehicle
- Figure 7.30 Velocity contour for base car and converted one with light bar

Figure 7.31 Light bar with and without rounded edge

Figure 7.32 Approximation surface for DV1 and DV2 versus drag force

Figure 7.33 Approximation surface for DV1 and DV2 versus drag force

Figure 7.34 Light bar with 0 and 48 mm height

Figure 7.35 Design parameter 2, length

Figure 7.36 Design parameter 1, sharpness

Figure 7.39 Response surface Model

Figure 7.40 Optimum configuration of the car with light bar

Figure 7.41 Contours of velocity for original and airfoil-based design

Figure 7.42 Velocity streamlines for original and airfoil-based design

Figure 7.43 Optimum configuration of the light-bars, (a) CAD model, (b)
Physical wind tunnel model

Figure 7.44 Flow visualisation using tufts for optimised model (rear view)

Figure 7.45 Flow visualisation using tufts for optimised model (side view)

Abbreviations

BL	Boundary Layer
CAD	Computer Aided Design
CFD	Computational Fluid Dynamics
DES	Detached Eddy Simulations
DNS	Direct Numerical Simulations
DoE	Design of Experiments
FEM	Finite Element Method
FFD	Free Form Deformation
FVM	Finite Volume Method
GA	Genetic Algorithm
Hex	Hexahedral cell
HGV	Heavy Good Vehicle
KO	Wilcox's $k - \omega$ Turbulence Model
KE	$K - \epsilon$ (Realisable) Turbulence Model
KRG	Kriging
LES	Large Eddy Simulations
LHS	Latin Hypercube Sampling
LSRL	Least-Squares Regression Line
MIRA	Motor Industry Research Association
MLS	Moving Least Square
MAM	Multipoint Approximation Method
NASA	The National Aeronautics and Space Administration
NRC	National Research Council Canada
OFI	Oil Film Interferometry
OLH	Optimal Latin Hypercube
PDE	Partial Differential Equations
PIV	Particle Image Velocimetry
PR	Polynomial Regression
QUICK	Quadratic Upstream Interpolation for Convective Kinematics Scheme
RANS	Reynolds Averaged Navier-Stokes
RSM	Response Surface Method

S-A	Spalart Allmaras Turbulence Model
SIMPLE	Semi-Implicit Method for Pressure Linked Equations
SGS	Sub-Grid Scale
SAE	Society of Automotive Engineers
SST $K - \omega$	Shear Stress Transport $K - \omega$
SPM	Sensitive Paint Measurements
SQP	Sequential Quadratic Programming
Tet	Tetrahedral cell
UFD	Undercarriage Flow Device
URANS	Unsteady Reynolds-Averaged Navier-Stokes
VG	Vortex Generator
VSD	Vortex Strike Device
YAST	Yorkshire Ambulance Service Trust

Nomenclature

A	Projected projected area of vehicles
b	Model building DoE
C	Cord length of the aerofoil
C_D	Drag coefficient
$C_D A$	Drag factor
C_L	Lift coefficient
D	Drag force
e	Solution error
E	Discretisation error
F	Objective function
i	Index i
j	Index j
k	Turbulence kinetic energy
l	Turbulence intensity
L	Characteristic length of body
l_e	Eddy length scale
L_{ij}	Distance between points i and j in Latin Hypercube
L_T	Turbulent length scale
m	Combined model DoE
m	Mass fraction of fluid
p'	Pressure correction term in the SIMPLE algorithm
p^*	Predictor pressure term in the SIMPLE algorithm
p_{New}	Corrected pressure term in the SIMPLE algorithm
r_i	Euclidean distance of the Response Surface prediction location from the DoE
Re	Reynolds number
t	Non-dimensional time
T	Temperature in degrees Celsius
U	Pseudo-potential energy of DoE points
u, v, w	Local velocity components in the x , y and z directions respectively
u', v', w'	Velocity correction terms in the SIMPLE algorithm
u^*, v^*, w^*	Updated velocity terms in the SIMPLE algorithm

$u_{new}, v_{new}, w_{new}$	Corrected velocity terms in the SIMPLE algorithm
\bar{u}	Mean local velocity component
u'	Fluctuating local velocity component
u^+	Dimensionless velocity parallel to the wall
u_∞	Free-stream velocity
U	Resultant velocity in the x direction
v	Model validation DoE
w_i	Gaussian weight decay function
y	Half thickness of the aerofoil
y^+	Dimensionless normal distance away from the walls
β	Yaw angle of the wind
δ	Percentage reduction in flow rate
ε	Dissipation of turbulence kinetic energy
ρ	Density of air
μ	Dynamic viscosity
η	Kolmogorov length scale of turbulence
τ	Shear stress within a fluid
τ_w	Wall shear stress within a fluid
ϕ	Scalar transport variable
θ	Closeness of fit parameter
Γ	Diffusion coefficient
Γ_M	Fluid viscosity
σ_i	Standard deviation of minimum distance of DoE
σ_F	Response

1. Introduction

The dynamic performance and fuel consumption of an automotive vehicle is directly influenced by its aerodynamic characteristics and increasing governmental concerns about vehicle emissions, has motivated significant improvements in aerodynamic design for most classes of road vehicle [1].

There is a wide interest in reducing HGVs fuel consumption via aerodynamic drag reduction and the current state of aerodynamic improvement technologies for HGV allows significant drag reduction to be made. Generally HGVs are aerodynamically inefficient compared to other ground vehicles due to their large projected areas and bluff-body shapes and their fuel economy can be improved by retrofitting it with aerodynamic drag reducing device. Contributions to HGV drag are mainly due to pressure drag associated with direct flow exposure on large tractor/ trailer fronts, cross-flow effects inside tractor/ trailer gaps, base wakes, and complex under-body flow structures [1]. It is estimated that the pressure drags on heavy vehicles account to more than 80% of the drag [2], the remaining being mainly due to frictional drag. Ever increasing fuel prices and environmental legislations are providing strong drivers to reduce fuel consumption and carbon emissions resulting from emergency response vehicles such as ambulances and Police cars. Within the UK for example, the Yorkshire Ambulance Service Trust (YAST) holds around 1400 vehicles that cover 25 million miles every year, resulting in the consumption of 4.2 million litres of fuel at a cost of more than £6 million [3]. The YAST, in common with all other Ambulance Services Trusts in the UK, has ambitious targets in reducing CO₂ emissions from its fleet operations (currently set at 30% [3]) and improved aerodynamic design has been identified as a significant potential contributor to achieving substantially reduced fuel consumption and CO₂ emissions.

This study focuses on the aerodynamic design optimisation of specific type of light truck, namely emergency response vehicles (ambulance, see Figure 1.1, and Police transport vehicles, see Figure 1.2 and 1.3) that have not been reported previously in the literature.



Figure 1.1 Side view of a Fiat ambulance (courtesy of P. Occardi)

In practice due to the range of existing regulations, the shape of ambulances cannot be changed radically due to constraints on features such as the maximum vehicle height and the minimum vehicle height at the rear in order to provide adequate access to the vehicle. An additional complicating feature for aerodynamic design optimisation of ambulance is the need for warning lights at the front and rear of the roof.



Figure 1.2 Side view of a Vauxhall Police van [4]

Overall the past several decades, a significant amount of effort has been put to reduce the aerodynamic drag of HGV. Thus the reduction in total aerodynamic drag will have a significant improvement on the fuel economy of a heavy vehicle. Traditional approach to aerodynamic design optimisation is using wind tunnel testing, however in recent years the number of studies which have applied computational fluid dynamics (CFD) and optimisation methods to improve the aerodynamic design of the vehicle has increased rapidly and it has been recognised

as providing a powerful and efficient means of generating improved aerodynamic performance, particularly when detailed experimentation in wind tunnels is not feasible, see e.g [5-11]. The focuses of the recent studies have been on the drag reduction of HGVs, see e.g [5-8, 12]. There have only been few studies on the aerodynamic improvements of light trucks and cars [8-9], in addition only small number of reported studies have reduced vehicle aerodynamic drag using automated design optimisation techniques [9]. Most previous studies on improving vehicle aerodynamics have focused on the drag reduction of HGVs vehicles. In addition only small numbers of the reported studies have reduced vehicle aerodynamic drag using automated design optimisation techniques.



Figure 1.3 BMW Police car [13]

In order to conduct a study of this kind, the completion of literature review with relevance to this particular field of engineering is the normal. In this case there is a true lack of evidence specially targeted at the drag reduction of an ambulance using CFD. On the other hand there have been huge amounts of studies carried out using CFD optimisation to reduce the drag of HGVs and vehicles of similar size to an ambulance. Literature reviews of the related area is given in the next chapter.

2. State of The Art

2.1. Background

Everything moving in the fluid (air, water...) is subject to a retarding force called Drag force. Drag force is a function of velocity, shape of the body and the viscosity of the fluid. In order to keep the body moving at a desired velocity, energy must be expended in order to overcome the drag force; therefore it is desired to minimize the drag force. Streamlining the body has been the main area of the effort for minimizing the drag [14]. Reynolds number is the critical parameter for purpose of the drag. It is directly proportional to velocity and length of the body and it is inversely proportional to the dynamic viscosity, see Equations 2.1.

$$\text{Re} = \frac{\rho U_{\infty} l}{\mu} \quad (2.1)$$

Where U_{∞} , in vehicle aerodynamics is the velocity of the vehicle, ρ is the fluid density and μ is the fluids dynamic viscosity and l is the characteristic length.

Reynolds number can be defined as the ratio inertial to viscous forces in a given fluid [15]. Therefore Reynolds number is very high in vehicle aerodynamic flows where inertial forces dominate and low for the flow of highly viscous oil. When Re exceeds a value of 400,000-500,000, the flow turns into turbulent from laminar over a flat plate. Unfortunately the value of Re at which turbulence occurs is exceeded in almost all cases of practical applications. As result so much effort has been put on smoothing the flow around the body in order to make it laminar [14]. The power generated by the engine is mainly spent on overcoming the Aerodynamic drag, Rolling resistance and Climing resistance. As drag is directly proportional to the square of velocity, while moving at high speed, the aerodynamic drag amounts for three-quarter of the engine power. Therefore reduction of the aerodynamic drag is very important for keeping the fuel consumption at the minimum [7].

Figure 2.1 shows that the force required to overcome the aerodynamic drag and rolling friction increases as the speed is increased. However the rate of increase in aerodynamic drag with increasing speed is greater than that for rolling resistance. As seen from the equation (2.2) the drag also depends on the projected area as well as

the velocity, V . C_D is non-dimensionalise form of drag force which shows how aerodynamic is an object and does not depend on the size of the object.

$$D = \frac{1}{2} \rho AV^2 C_D \quad (2.2)$$

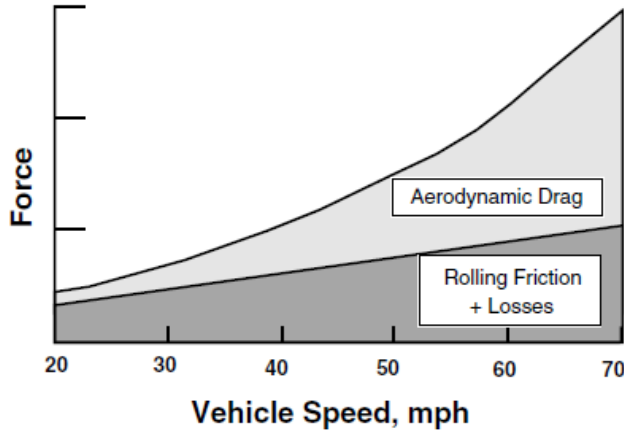


Figure 2.1 Resistance force requirement versus vehicle speed for HGV [16]

At 100 km/h, aerodynamic drag is accountable for 80% of the total drag. And vehicles travelling at higher speeds spend even more energy in order to overcome the aerodynamic drag, since the drag increases as the speed increases [17]. Reduction in the value of projected area will reduce the drag force experienced by the vehicle. Mathematically main components of the drag are the normal (pressure) and tangential (skin friction) forces. Experimental evaluation of the total drag of the elements of a vehicle, wheels, mirrors and other elements is very difficult as it needs detailed stress distributions over the entire surface. On the other hand, such a detailed stress distribution can be achieved using CFD. In addition, in contrast to wind tunnel experiments, there are no limitations in terms of size and geometry of the test section. Simulating the relative motion between the road and vehicle is also relatively easy [18]. The main reason for using the numerical methods in the study of vehicles is that they can produce information before any experimental work and tests. The data indicates that the tractor-trailer truck without aerodynamic shaping and fairing will have a drag coefficient between 0.7 and 0.9 whereas a tractor-trailer truck with aerodynamic shaping and fitted with roof and side fairing can have a drag between 0.6 and 0.7 [16]. At 100 km/h, aerodynamic drag is accountable for 80% of the total drag. Traditionally, all the data for analysis would only come from the experiment from scaled wind tunnel or full-scaled road tests. However recent advances in CFD modelling have made it easier to simulate the experiment

computationally and solve it numerically before any full experiment is carried out [17]. The CFD tools can be used with full-scale experiments, in order to guide the design refinement of devices for optimum performance, and therefore final product will be a specific design concept that can reduce the drag coefficient and thus improve the fuel efficiency [6].

CFD simulation has four main benefits:

- 1- It only requires a computer model and therefore reduces the cost in terms of time and money
- 2- It will produce a very detailed results
- 3- Since it is done in computational environment, it is very compatible with optimisation application [8].
- 4- Previous studies have confirmed a good agreement between the CFD simulations and the experimental results [17, 19-21].

The aerodynamics of the ground vehicle are generated from different sources, the external, which is body and its components such as mirrors and tyres et..., and internal components like the engine cooling system etc.... Simulation and optimising all these components is a big challenge [8]. The average drag coefficient of the HGVs was 0.7 in 1920s, and today this number is reduced to 0.5. This improvement mainly happened after the oil crisis in 1970s [8]. The typical simulation of ground vehicle starts by creating a computer model, it could be generated, for example, in a CAD package and be transferred first to solid modelling for further completion. The next step is the solution step that generates the flow fields parameters in the computational domain. Then, the velocity, pressure and other forces are analysed and if there is any optimisation process involved, the force variables will be transferred to the optimisation algorithm [8]. The most difficult and time consuming parts of the whole computation simulation procedure is the CFD model preparation and mesh generation step. The focus of the literature will be on Experimental work and it moves into the previous work on CFD drag reduction and finishes with Optimisation and methods for parameterisation.

2.2. Literature Review

Croll *et al.* [22] conducted an experimental study on HGV drag reduction. Few devices were tested in order to increase the base pressure [22]. Results of the study of add-on show 7.6% reduction in drag comparing to the baseline [22]. Comparing

to the work of Wood *et al.*[16] who achieved similar results by focusing on the rear low pressure area, see Figure 2.2.

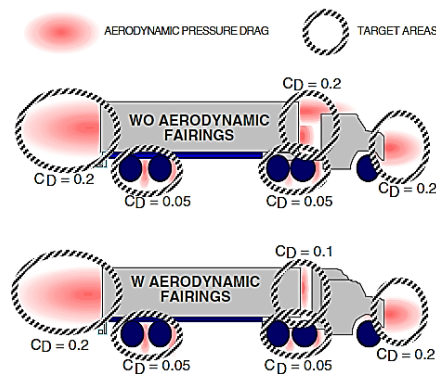


Figure 2.2 Graphic depicting the distribution of aerodynamic drag for a heavy vehicle tractor-trailer truck, with and without aerodynamic fairings, operating in a zero crosswind condition [16]

Figure 2.2 presents the target areas for drag reduction of HGV and their corresponding drag coefficient contribution. Modifications in these areas can result in reduction in drag coefficient and therefore save in fuel usage.

The main challenge was realised, in this study, to be the control of the massively separated and unsteady wake behind the bluff base area. VSGs were used which would generate some large vortices on the side and exterior surfaces to energize the flow on the rear part, therefore enabling the flow to expand to the base region and increase the back pressure which would result in decreasing the drag coefficient. The result would be a stable wake flow and high pressure base as results of it, see Figure 2.3. [16].

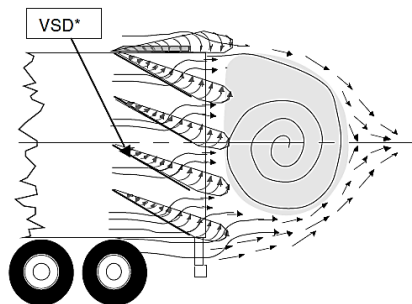


Figure 2.3 Sketch of a side view of the vortex strake trailer base wake flow characteristics for a typical tractor-trailer truck with the base treatment installed [16]

Similar results were reported by Schoon *et al.* who also investigated the impacts of several add-on devices on the reduction of the drag coefficient of HGV [23]. Drag reduction of 8% to 11% were achieved by Schoon which is relatively similar to the previous studies. Ron Schoon *et al.* conclude that the impact of the combining add-on devices is usually not equal to the sum of their individual impacts due to the interactions in the flow field. The overall drag reduction of 23% was achieved in this study by combination of lengthened side exterior and air fairing, trailer wake angled plates and straight skirt. Aider *et al.* [24] achieved 25.2% drag reduction by also combination of add-on devices at different parts of the vehicle. He concludes that the combination of the all the best individuals configurations, leads to the best drag reduction of. Similar to the above findings Jason Leuschen *et al.* [25] carried out full scale wind tunnel tests on aerodynamic drag reduction devices for tractor-trailer. Leuschen *et al.* [25] also confirmed the drag coefficient reduction of 0.11, compared to the baseline model by carrying out full scale wind tunnel tests on aerodynamic drag reduction devices for tractor-trailer.

Vortex generators can prevent the separation and as a result reduce the drag but they also create drag and since this drag depends on the shape and size of the vortex generators, therefore they need to be optimised to the best shape with minimum drag. There has been several studies on using the VGs to control the flow and subsequently reduce the drag force by Koike *et al.* [26], Aider *et al.* [27] and Duriez *et al.* [28]. Koike *et al.* [26] studied VGs on the Mitsubishi Lancer Evolution. It was found that the optimum height of the VGs is almost equivalent of the boundary layer thickness and the optimum method of the placement is to arrange them in a row in a lateral direction 100mm upstream of the roof end with the spacing of 100mm. The experiment also was analyzed using CFD [26]. On the similar study that Aider *et al.* [27] conducted on Ahmed body. The vortex generators being assessed for this study is, as shown in Figure 2.4, trapezoidal blades [27]. Study on the influence of the longitudinal position and angle of the vortex generators, reveals that for both cases (60° and 120°) drag and lift decreased about 12% and 54% respectively. The position of the optimum is upstream of the separation point at 0.26 m.

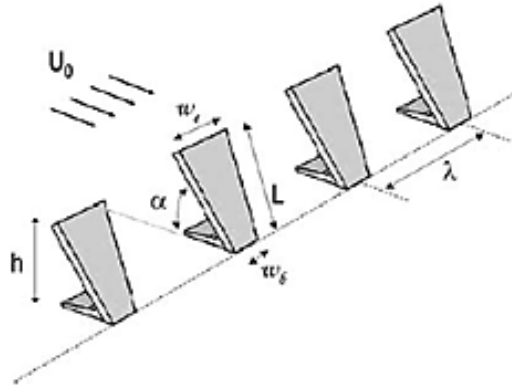


Figure 2.4 Description of the VGs geometry with the typical dimensions characterizing the device used in the experiments, angle α is 60° in the sketch which will be varied in the study [27]

Aider *et al.* [27] also studied the influence of the Reynolds number to find out if the Vortex generators remain efficient for higher Reynolds number. The results showed that the drag reduction decreases as the velocity increase (20 m/s, 30 m/s and 40 m/s, 12.2%, 7.1% and 3.7% drag reduction respectively). Similar study was done by Duriez *et al.* [28] on effectiveness of the Vertex Generator to control the separation over a curved ramp. It was concluded as it can be seen from Figure 2.5, VGs has effectively delayed the separation point further downstream [28].

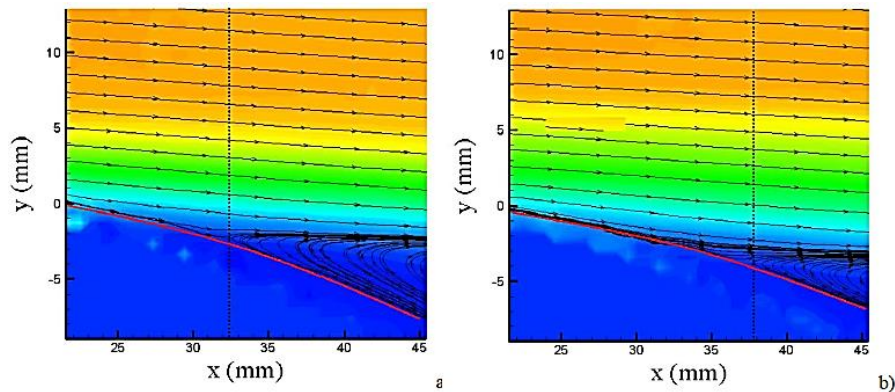


Figure 2.5 Streamline of time and space averaged flow over a curved ramp a) without VG's b) with VG's. Doted point is the position of the separation [28]

Experimental investigation is often expensive and time consuming; therefore numerical simulation by means of CFD is replaced as it is less expensive and faster. The experimental results are used to validate the numerical results. Several studies have been conducted using CFD in order to reduce the drag coefficient of different vehicles [6-8, 18, 29-34]. Study was conducted by Raveendran *et al.* [7], to reduce

the drag force of intercity bus. $K - \epsilon$ turbulence model was used with incompressible and steady flow. Raveendran refers to $K - \epsilon$ turbulence model as being able to converge to an accurate result in comparatively less time [7]. Results they achieved indicated the stagnation points in the front and the mirrors and low pressure on the rear of the bus comparing to the front due to the separation and circulation of the flow. This pressure difference is the main reason for the pressure drag of the vehicle. The new bus design drag coefficient was found to be 0.296 which is 44% improvement compared to the baseline model with the drag coefficient of 0.53 [7]. Figure 2.6 shows the overall drag comparison between the benchmark and new design at different design.

Figure 1.19 shows the results of this study for different velocity.

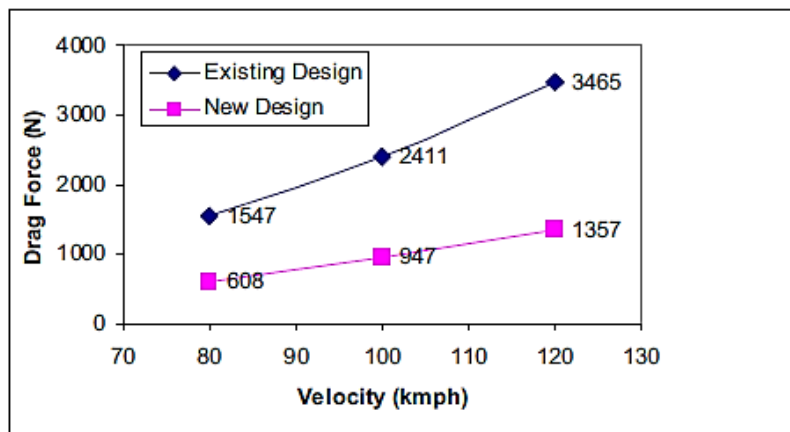


Figure 2.6 Overall drag comparison between the benchmark and new design at different speeds [7]

Roy and srinivasan [29] also used $K - \epsilon$ turbulence model and achieved 30% drag reduction on truck-like bluff body which correspond to estimated fuel saving of 15%. $K - \omega$ turbulence model has also proved to work well for HGVs since comparing the results of the computational and experimental data shows 1.12% difference on the study conducted by Huminic and Huminic [18]. $K - \epsilon$ turbulence model is used on most of the studies on CFD analysis of the HGVs such as study by Feng *et al.* on the CFD analysis of sedan and study by Illhan Bayraktar *et al.* [8] on computational simulation of the ground vehicle. In this study the common turbulence models ($K - \epsilon$, RNG $K - \epsilon$, SST, $K - \omega$) were examined. RNG $K - \epsilon$, SST and $K - \omega$ models showed more accurate behaviour comparing to the others. RAN- $K - \epsilon$ turbulence model was used as turbulence model in this study to assess the drag force of the HGVs [8]. $K - \epsilon$ turbulence model was also used on the computational and experimental investigation of the drag reduction device for HGVs

by Khalighi *et al.*[32]. Results of the study confirms the validity and usefulness of the unsteady RANS simulation for study of wake. A study conducted by A. Huminic *et al.* [30] also confirmed the capability of the CFD simulation to predict the drag force of the HGVs. $K - \epsilon$ turbulence model was used in this study and the importance on the using rotating wheels was highlighted.

CFD simulations need to be compared with the experimental results for the purpose of validations. Several studies have been conducted in the past to reduce the drag force of the HGVs using CFD together with experimental validations see [11, 17, 19, 21, 35-38]. Pointer *et al.* [17] investigated the effects of different parameters in CFD simulation of the commercial vehicle, and compared it with experimental results. $K - \epsilon$ turbulence model was used and The results for the predictions of the drag coefficient shows the error decreases from 12% to 1.7% as the mesh size become finer. Pointer *et al.* [17] describes that the difference in the accuracy of the drag coefficient is in fact, a result of small differences in the pressure distribution over the entire surface rather than large localized differences. The study in detail reveals that most discrepancy comes from the under-body and in the gap between the tractor and the trailer [17], it is also shown that prediction of low drag states is closer to the experimental data comparing to the experimental data. Study by Gilkeson *et al.* [11] also shows that the CFD results are in agreement with the experimental data but for the area of separations and wake regions, it over predicts pressure distributions. But despite this, overall agreement is good [11]. Gilkeson *et al.* [11] concentrated on experimental and computational aerodynamic analysis of passive ventilation characteristics of small livestock trailers. Similar study was conducted by Verzicco on the simulation of the flow around HGV [35]. The results were compared with the available experimental data. Comparing the numerical results of the baseline with the experimental data, they show a good agreement and the effect of the separation bubble is captured accurately. The length of the separation bubble predicted by simulation is 1.73 which is very closer to the experimental value of 1.6. Comparison between the simulation and the experimental data shows that the time-average quantities and also flow dynamics were predicted accurately. It also shows that the drag reduction simulation results very good agree with the experiments [35].

Figure 2.7 and 2.8 are the comparison between the CFD and experimental result by Ortega *et al.* [36]. The study is to compare the numerical results from the LES simulation with the experiments and the wake behind the vehicle was analysed. Figure 2.7 presents time average velocity fields in the vertical mid-plane for the

coarse and fine grid. It is clear from Figure 2.7 that the circulations have been more captured with the fine grids.

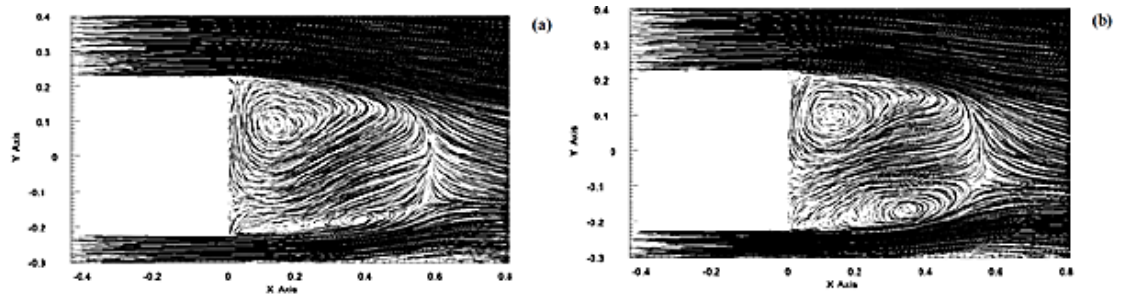


Figure 2.7 Time-averaged velocity fields in the vertical mid-plane for a) coarse and b) fine grids [36]

Figure 2.8 also presents corresponding PIV (Particle Image Velocimetry) velocity measurements in the vertical plane.

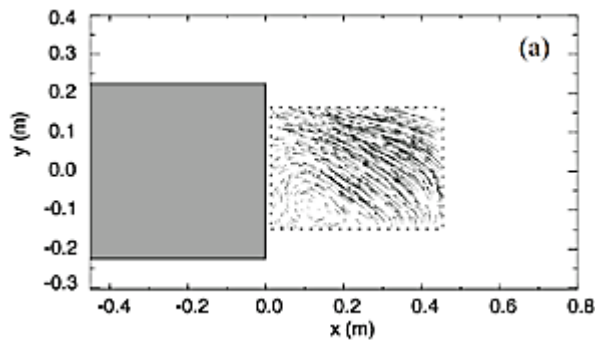


Figure 2.8 PIV velocity field measurements in the vertical mid-plane [36]

The difference in the wake structure, when comparing the results of the vertical mid-plane, is obvious. In the computational simulation, there are two circulation regions in the separated flow, whereas there is only one in experimental data. This may be as a result of the PIV camera not covering all the areas, or it may be as a result of truncating the model or neglecting the under-body on the experimental model. LES approach again showed potential to achieve an accurate results when compared with experimental data by McCallen *et al.* [19]. He did investigated the validity of the CFD on heavy duty trucks. Drag coefficient was reduced by 25% from 0.6 to 0.3. The experimental testing was performed on 1/8 scale of Sandia model in NASA Ames wind tunnel and the results proved the ability of the CFD to capture the unsteady wake flow. Despite these agreement Pankajakshan *et al.* [38] concluded on

his study on the simulation of class 8 trucks with rotating wheels that the simulation without spinning wheel can over predict the drag by 7%. Similar to the previous study [30], the affect of wheel on the CFD results was highlighted by Pankajakshan *et al.* [38] as well as study by Duncan *et al.* [21]. He describes the CFD simulation as a reliable means to evaluate wheels designs early in the vehicle development process. It compares the numerical results with the experimental and suggests that the simulation results are well-correlated to the experimental results [21]. The limitation of the CFD simulation approaches for rotating wheels are as follows [21]:

- Need for the accurate geometry of the vehicle including its parts
- Mathematical approximation of the transient and airflow

The effects of the rotating wheel using typical angular velocity approach and rotating geometry approach is compared with the wind tunnel experiments. The drag changes, overall, match closely with the wind tunnel data. It is concluded from this study that simulation can be used to predict the drag effect of the wheel and provides an understanding of the aerodynamic effects which can lead to optimum design solutions in respect to drag [21].

The effectiveness of the CFD simulation was discussed in details with the details of the past studies. CFD has been very popular in the past for the means of analysing the aerodynamic behaviour of the HGVs in order to reduce the their drag force. CFD simulation has recently been combined with optimisation in order to modify the shaped of HGVs to the optimum design [10, 39-42]. Doyle *et al.* [39] has combined CFD with Optimisation (Genetic Algorithm) in order to find the minimum drag coefficient for tractor-trailer. Genetic Algorithm was used to determine the optimal position, size, position and curvature of the flap for the base drag reduction. Half of the model was used for reducing the computation cost, and five variables were used for the modelling of the base region slats. Figure 2.9 shows five variable which was used for the optimisation [39].

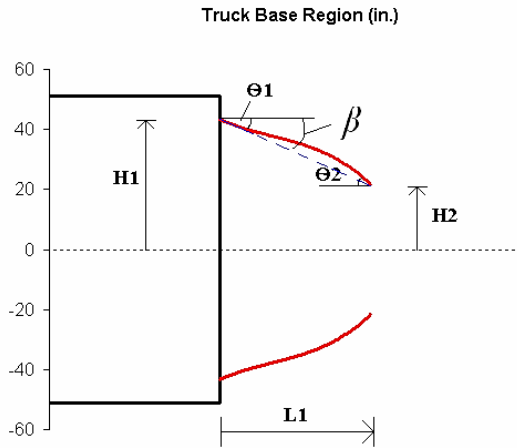


Figure 2.9 Depiction of slat optimisation parameters [39]

The drag coefficient was reduced proximately 29% from 0.6 to 0.426 by means of CFD optimisation. Attached flow and also reduction of the circulation region can be seen in Figure 2.10.

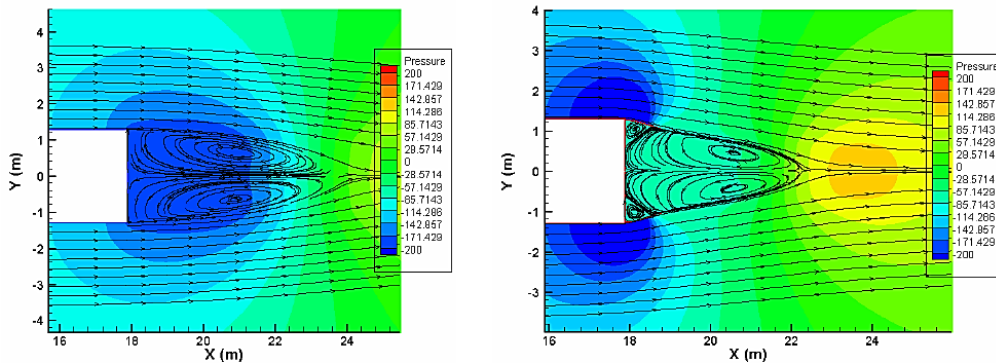


Figure 2.10 Wake region without (Left) and with GA optimised slat (Right) [39]

Another study by Williams *et al.* focused on the methods for drag reduction of light trucks, using CFD and numerical optimisation techniques [10]. For CFD simulation, $k - \epsilon$ model was selected as it has excellent performance for relevant flow and also is well established. After development of the geometry, the physics of the flow should be specified in CFD solver. The last stage is to set up an optimiser. The optimiser should be able to effectively manipulate the design variables as well as calculating objective function. The new variables have to be accepted by the geometry and meshing technique. Then the new mesh will be created and the process starts again. The new geometry will be solved and the new objective function value will be compared to the old one. Data obtained from the experiment shows that reasonable improvement can be achieved through CFD optimisation and

it proves that optimisation methods are very useful and predictive of possible improvements. Gilkeson *et al.* [40], Lietz [41] and Chen *et al.* [42] also investigated the capability of the CFD optimisation of the reduction vehicles drag force. Gilkeson *et al.* [40] was based on the shape of the livestock trailer with the three design variables as it can be seen in Figure 2.11.

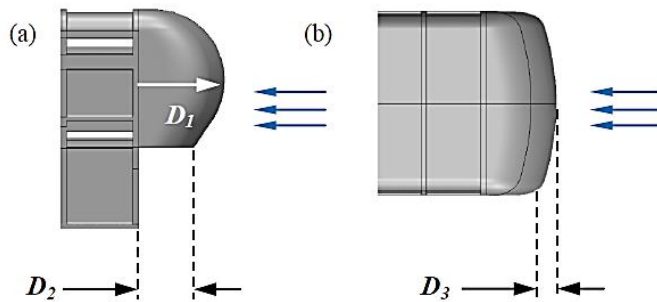


Figure 2.11 Illustration of the three design variables shaping the headboard fairing. A) Side view b) and aerial view [40]

The method showed to be very effective and 6.6% drag reduction was achieved by installing an optimised fairing in front of the trailer. Figure 2.12 shows the pressure distribution around the model with and without fairing.

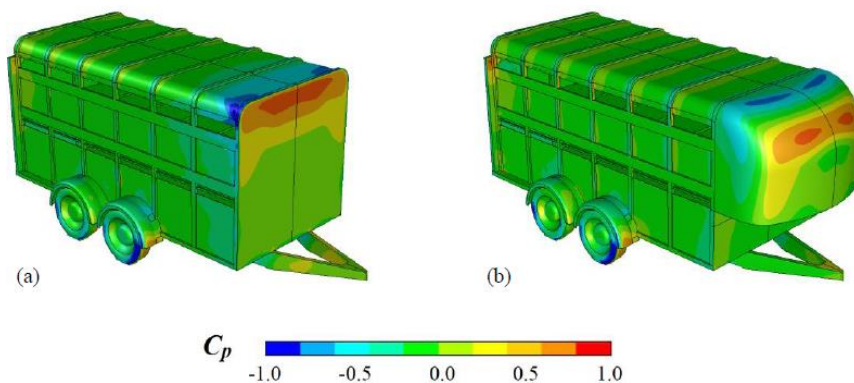


Figure 2.12 Surface contour plots of the pressure coefficient for the baseline trailer and the optimum fairing predicted by met model [40]

Lietz [41] also confirms that the process of CFD optimisation is useful in support of vehicle aerodynamic development in a production environment. The use of digital simulation especially in the early stage of the vehicle development and avoidance of extensive clay model testing in the wind tunnel is an essential component in this development process. But even in later stages, digital simulation can still contribute valuable information and help keeping the amount of wind tunnel testing at a

minimum [42]. Lietz [41] integrated the morphing, simulation and optimisation technologies into a single process for optimisation of vehicle shape. His goal was to deliver an aerodynamic shape optimisation methodology capable of investigating the total design space around a particular theme. The process defines the minimum drag attainable from the shape, the optimum factor for each parameter and provides the aerodynamicist with an interactive tool. Chen et al. [42] optimised the Shanghai Volkswagen (New Lavidia) development process by extensively using CFD simulation to reduce aerodynamic drag in a very early phase of the project. The approach with significant involvement of CFD for the aerodynamic optimisation of the New Lavidia has managed to meet the target of 4% reduction in aerodynamic drag over the Lavidia (last generation) with minimal use of physical testing in the wind tunnel [42]. Wind tunnel testing was then done at the end of this phase in order to validate the CFD results. Figure 2.13 shows the comparison between the predicted and measured aerodynamic drag.

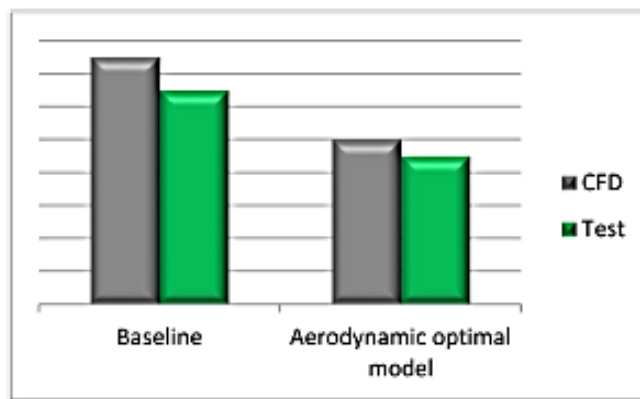


Figure 2.13 Comparison between predicted and Measured aerodynamic drag [42].

The optimisation work was also done on other parts of the car and improvements were achieved. Figure 2.14 shows the comparison of the drag force for the CFD and experimental values in the detailed engineering phase of the work. Q. Chen et al. [42] concludes that the two objectives of drag reduction and also a good accuracy from the validation, have been achieved.

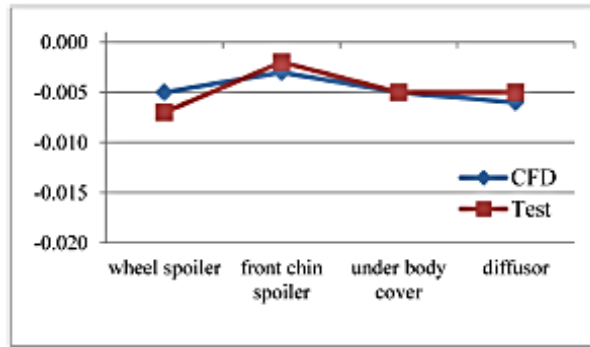


Figure 2.14 Comparison of the drag between CFD and test for new Lavidia [42].

Parameterisation of the geometry, as one of the most important part of the optimisation process, will be used in this work. Following is the summary of the past literature on different parameterisation methods used on similar studies. One of the most important ingredients in numerical optimisation is the choice of design variables and the parameterisation of our system in using these variables [43]. Past methods often involve complex parameterisation schemes which use arcs, circles and polynomials for geometry creations [44]. Many of these methods require large data sets to describe the profiles. In addition, they do not provide simple, intuitive parameters for the designers to control. Bezier curves were developed by Dr. Pierre Bezier who was an engineer with the Renault car company in the 1960's [45]. Bezier curves have since become a popular method for creating parametric curves and they have wide applications including postscript font definition, see Figure 2.15, turbine blade design [46], wind turbine airfoil design [43, 47]. Figure 2.15 shows different examples of Bezier curves with different degree of freedom.

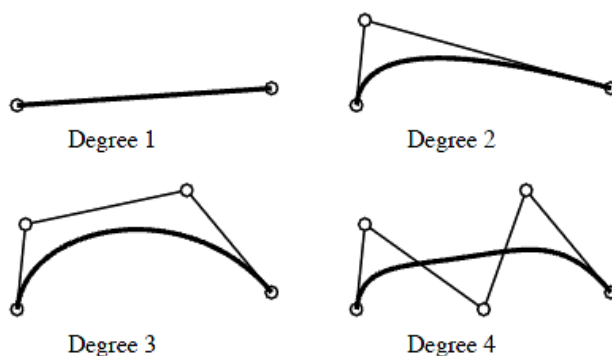


Figure 2.15 Bezier curves of various degree [44]

Often a single Bezier curve is insufficient for describing a complex profile and several of them are joined together. Karpowitz [44] proposed Bezier curve fitting

approach as a tool to improving the existing design of the turbine blade. He used an optimisation technique to determine the control points for the approximated curves while maintaining tangency and curvature at the connections [44]. The study confirms that the Bezier curve approximation closely matches the existing data set while maintaining tangency and curvature at the connection points. He concludes that a Bezier curve approximation is a useful method for creating a robust, parametric geometry definition. This approach provided a simple method for optimising the curve fit based on the continuity at the junctions [44]. Bizzarrini et al. [43] also suggests that one of the an important ingredients in numerical optimisation is the choice of design variables and the parameterisation of our system in using these variables. In order to reduce the number of necessary parameters to take into account to describe the air-foil shape, but without loss of information about the geometrical characteristic of the air-foil, it is necessary to choose a proper design variable [43]. In his study, for optimisation of the wind turbine blade, Bizzarrini [43] used a composite third order Bezier curve to describe the geometry. The advantage of this choice is the possibility to conjugate the properties of the Bezier function in terms of regularity of the curve and easy usage, with piecewise structure that allows also local modification to the geometry. On a similar study, Sarbajit Pal et al. [48] proposed an efficient face recognition scheme by using Bezier curve fitting. The two control points of a Bezier curve are interpolated by this method [48]. The faces with expressions are compared against the model face database consisting of normal faces. He concludes that the efficiency of the parameterisation method and the algorithm used is 100% [48].

An important part of this work is the optimisation. After the process of parameterisation, the model will be optimised for the solution with the minimum drag force. Following is the past literature on the optimisation techniques. Design optimisation is becoming increasingly important in engineering practice [49-51]. In practice shape optimisation is becoming an important part of the design process for internal and external vehicle aerodynamics [52, 53]. Gradient-free method such as Genetic Algorithm [54-56] and gradient-based methods such as adjoint method [57-59] are usual methodologies to solve optimisation problems. The computational cost of each method is different. In general, if the problem contains n design variables, a Genetic Algorithm must perform n^2 objective function evaluations to improve the original design. On the other hand gradient-based methods require $O(n)$ objective function evaluations per design cycle [60]. For problem involving many design variables and few cost functions a better alternative is to employ an adjoint formulations [57, 61, 62].

The gradient-free optimisation in the form of Genetic Algorithms is becoming popular due to their ability to find the global optimum and straight forward implementation [63]. However in many engineering applications, such as aerodynamics, finding a local minimum is also necessary. As gradient based optimisation algorithms are efficient at finding local optima, they are finding widespread use in external aerodynamics [49, 64]. In the case of gradient based optimisation, adjoint method has been identified as the method of choice for the computation of sensitivities [65]. Adjoint methods have been recognized by the automotive industry as an efficient optimisation tool only recently, while already established in the aerospace sector [66]. The adjoint approach to optimal design consists of followings [67, 68]:

- Computing the sensitivities of the cost function via an adjoint state
- Feeding these sensitivities into a gradient-based optimisation algorithm

It is the ‘‘cost independence of the number of design variables’’ characteristics of the adjoint method, that opens up unparallel possibilities for design optimisation and one DoEs not have to concern oneself anymore with a complicated CAD parameterisation [69]. Discrete adjoint method is a technique allowing efficient evaluation of the sensitivities (Derivatives) of a function depending on the solution of a discretised partial differential equations (PDE) [70, 71]. It is numerical method for effectively computing the gradient of a function in a numerical optimisation problem. Discrete adjoint techniques allows the use of integration by parts, resulting in a form which explicitly contains the physically interesting quantity [72]. It gives an efficient way to evaluate the gradient of a function [73]. Adjoint method is very effective on find the global optimum on application where there are high number of design variables since it is based on the gradient of the function. It has recently become popular on automotive applications, see [4, 63, 65, 69, 72]. Muller *et al.* [72] refers to gradient based method such as discrete adjoint method as an efficient method specially when there are many design variables and if the design is already close to optimal. He also mentions that the main challenge in gradient-based method is to evaluate the gradient in a computationally efficient manner [72]. The The EU-funded 'Fluid optimisation workflows for highly effective automotive development processes' (FLOWHEAD) Project is an example of successful optimisation work by using adjoint method [74, 75]. The aim of FlowHead is to develop fast gradient-based optimisation methods using adjoint sensitivities for automotive flow design. It focused on developing adjoint solvers for CFD problems in the automotive industry,

and integrating them into the design workflow. The ultimate goal was to speed up the design process thereby improving its labour and cost effectiveness. Applications in various test cases such as external vehicle aerodynamics, side mirror acoustics, climatisation ducts and electric vehicle battery cooling were identified. Application to these cases demonstrated significant reductions in lead time, thereby offering a viable solution for the car development process. Overall, the FLOWHEAD project illustrated the full potential of CFD and adjoint optimisation method in the automotive industry [75, 76].

As mentioned previously the gradient-based method are mainly used to find the local optimum and where there are high number of parameters in the application and gradient free method such as Genetic Algorithm is a global method and is efficient enough when the number of parameters are low. Therefore the focus of the literature will be more on Genetic Algorithm which is more suitable for this study and will be useful in this work. Genetic Algorithm has been used on several recent studies on the drag reductions of different vehicles and also aerodynamic analysis of objects such as wind turbines and it is well established method, see [43, 46, 77-80]. Lorriaux *et al.* [77] and Krajnovic [78] conducted two separate optimisation study to reduce the drag force of the railway motor coaches. An aerodynamic optimisation procedure using a Genetic Algorithm was used together with CFD software for the flow simulations to bring out train shapes with lowest possible aerodynamic drag.

The train geometry used in Lorriaux's study [77], as well as the computational domain and the boundary conditions are shown in Figure 2.16.

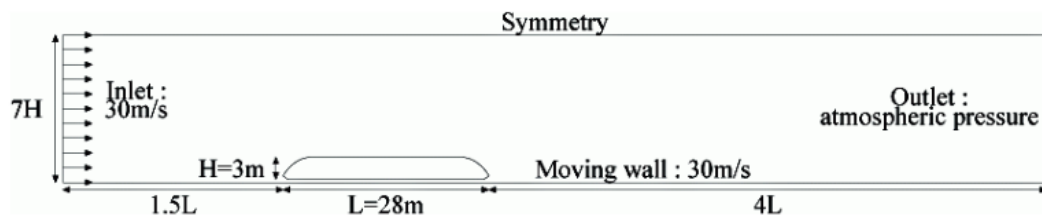


Figure 2.16 Computational domain and boundary condition for railway analysis [77]

Parameterisation and the optimisation were implemented on the nose of the coach in order to reduce the high pressure experienced on that area and consequently reduce the drag force. Figure 2.17 shows the geometry of the nose and its parameters.

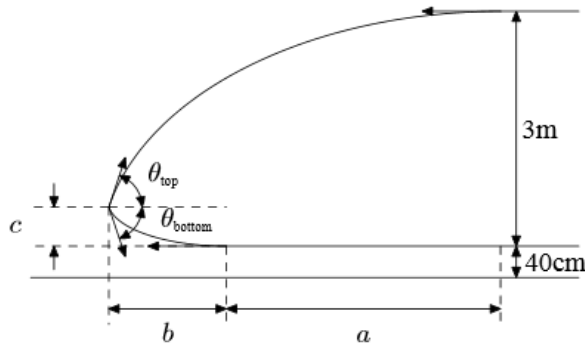


Figure 2.17 Geometry of the nose [77]

Figure 2.18 and 2.19 show the influence of the parameters θ_{top} and the nose length $(a + b)$ on the drag force production respectively. The data pattern in Figure 2.18 shows that best solutions are obtained for the whole range of the parameter θ_{top} . As a consequence, it can be concluded that this parameter is not most significant. However, the fact that the data are distributed in a triangular area with better results towards the smaller values of θ_{top} reveals that this parameter is nevertheless playing a role and that the optimum is likely to be found in this area.

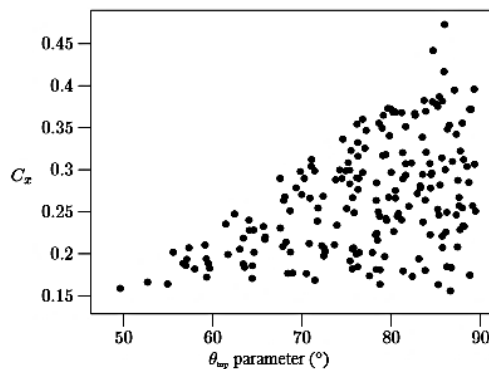


Figure 2.18 Influence of the parameter θ_{top} [77]

As far as the nose length $(a + b)$ is concerned, Figure 2.19 clearly shows a direct influence on the drag coefficient: best solutions are only obtained for larger values of $(a + b)$. This trend denotes a significant parameter.

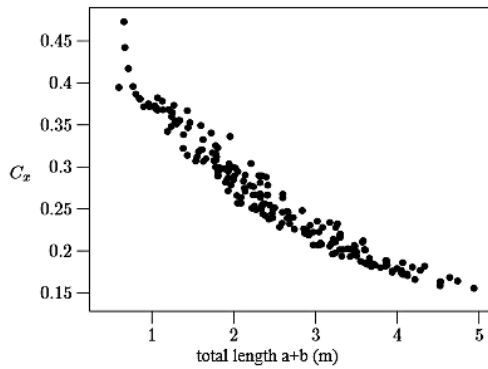


Figure 2.19 Influence of the total nose length ($a + b$) [77]

E. Lorriaux et al. [77] concludes that comparison of the results obtained by Genetic Algorithm with the random method demonstrates that, Genetic Algorithm is able to detect a low drag solution. He also confirms that Genetic Algorithm is feasible and efficient for finding the global optimum. However he indicated that the solution obtained from the Genetic Algorithm strongly depends on the initial population [77].

Krajnovic [78] also manipulated the nose of the train and also worked on the improving the drag force by means of passive methods of Vortex generator. Figure 2.20 shows the parameters, for improving the nose of the coach and also the vortex generator used.

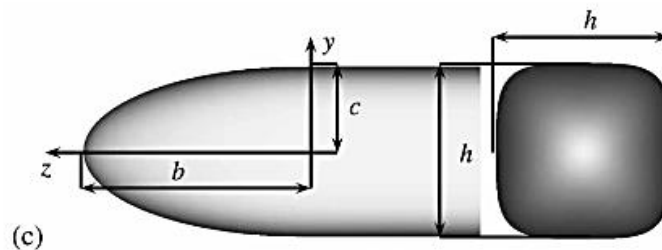


Figure 2.20 Shape of the front of the train including the parameters [78].

The optimisation problem was solved using Genetic Algorithm. Krajnovic [78] firms the method used is an efficient shape optimisation technique for the aerodynamics of high speed trains. Genetic Algorithm method has also been used on CFD optimisation of the wind turbine as mentioned earlier by Bizzarrini et al. [43] and Giannakoglou [46]. Bizzarrini et al. [43] suggests that the choice of optimisation algorithm is very important because the final results are usually dependent on the specific algorithm in terms of accuracy and local minimum sensitivity. He used Genetic Algorithm for his optimisation process [43]. He refers to the reasons to use the Genetic Algorithm as being capable of exploring wide range, non-linear and

discontinuous domains and being less sensitive to the initial configurations especially when compared to gradient based algorithm [43]. Bizzarrini et al. [43] Aerodynamic efficiency optimisation of an air-foil for the outer part of the blade compared with the existing wind turbine air-foils has been studied and a family of air-foils that improves the aerodynamic efficiency by using Genetic Algorithm. The comparison shows that the usage of Genetic Algorithms helps to achieve better air-foil performance at the affordable computational cost [43]. Giannakoglou [46] also used Genetic Algorithm random search algorithm based on the model of biological evolution, to find the optimum solution. Close to the optimum solution, the Genetic Algorithm switches to an iterative hill-climbing method which undertake the final refinement. Giannakoglou [46] concludes that the proposed geometrical model proved to be very effective for modelling of the turbine blades and also Genetic Algorithm proved to be efficient optimisers [46]. Genetic Algorithm has also been used as an affective optimisation method on several other aerodynamic applications such as study by Fan et al. [79] to improve the efficiency of the jet pump and study by Khan et al. [80] to optimise the ventilation system design to control airborne contaminant dispersion and occupant comfort. Fan et al. [79] used Genetic Algorithm (GA) to find a global minimum with fitness evaluations carried out using the surrogate models [79]. By using CFD optimisation, J. Fan et al. [79] managed to achieve a substantial improvements in jet-pump design and pump efficiency has increased from 29% to 33% and the energy requirements of the pump have been reduced by over 20% [79]. Khan et al. [80] used similar methods as J. Fan et al. [79] for its optimisation. He used the optimisation scheme based on the combination of response surface methodology and Genetic Algorithm. He refers to GA as one of the most popular in this category and widely accepted global optimisation technique which has been inspired from Darwin's theory of natural selection. This method has demonstrated its capability to handle discontinuous variables and also noisy objective functions [80]. In addition it can find near optimal solution using less computing time compared to other methods. Since it is stochastic method, it has a better chance to explore the entire design space and reach global optimum [80].

2.3. Main Focus

The main focus of the present study is to exploit the advantages of computer simulation and optimisation techniques to modify and optimise the geometry of Emergency Response Vehicles in order to reduce the drag force and consequently lower the fuel consumptions. These are investigated here using detailed CFD simulations and Optimisation techniques, validated by experimental data. The remainder of this thesis is organised as follows: Chapter 2 briefly covers the

aerodynamic characteristics of bluff bodies including drag reduction strategies. Chapter 3 describes CFD methodology and the techniques which are required for the examination of vehicle aerodynamics. Verification and validation is also covered in this chapter. Chapter 4 focuses of the optimisation techniques and it includes the optimisation related materials. Experimental techniques, Experiment and CFD validation is discussed in details in chapter 5 and chapter 6 will include the design optimisation of Emergency Response Vehicles. It contains three different CFD optimisation study on different types of Emergency Response Vehicles. Finally, conclusions and future work are discussed in chapter 7.

3. Vehicle Aerodynamics

Modern vehicle design is influenced by aerodynamics which influences a number of parameters such as energy efficiency. Aerodynamics can strongly effect the fuel consumption of the vehicle, as more streamline shape will result in a lower drag coefficient. As discussed in the previous chapter, drag force is the key to fuel consumption reduction which in turn is a function of the aerodynamic characteristics. This chapter focuses on some of the key aspects of vehicle aerodynamics which are most relevant to the present study.

3.1. Fundamentals

Flow field generated by the motion of the vehicle through the air is three-dimensional and highly turbulent. However such complexities occur due to a number of elementary principles which lie at the heart of aerodynamics.

3.1.1. Governing Equations

Although the flow field is very complex, the flow physics is based on the three conservation laws [81]:

- Conservation of mass
- Conservation of momentum
- Conservation of energy

They imply that mass, momentum and energy neither can be created nor destroyed and Newton's law is valid. They are described by a set of equations which were separately derived by Claude Navier and George Stokes; the Navier-Stokes equations 3.1 [82]. The motion of a non-turbulent, Newtonian fluid is governed by the Navier-Stokes equation. The general form of the transport equations [83] which are conservative and utilised by CFD. Following is N-S equation in x, y and z direction [56, 84]:

$$\rho \left(\frac{\partial u}{\partial t} + u \frac{\partial u}{\partial x} + v \frac{\partial u}{\partial y} + w \frac{\partial u}{\partial z} \right) = -\frac{\partial P}{\partial x} + \eta \left(\frac{\partial^2 u}{\partial x^2} + \frac{\partial^2 u}{\partial y^2} + \frac{\partial^2 u}{\partial z^2} \right) + F_x \quad (3.1)$$

$$\rho \left(\frac{\partial v}{\partial t} + u \frac{\partial v}{\partial x} + v \frac{\partial v}{\partial y} + w \frac{\partial v}{\partial z} \right) = -\frac{\partial P}{\partial y} + \eta \left(\frac{\partial^2 v}{\partial x^2} + \frac{\partial^2 v}{\partial y^2} + \frac{\partial^2 v}{\partial z^2} \right) + F_y$$

$$\rho \left(\frac{\partial w}{\partial t} + u \frac{\partial w}{\partial x} + v \frac{\partial w}{\partial y} + w \frac{\partial w}{\partial z} \right) = -\frac{\partial P}{\partial z} + \eta \left(\frac{\partial^2 w}{\partial x^2} + \frac{\partial^2 w}{\partial y^2} + \frac{\partial^2 w}{\partial z^2} \right) + F_z$$

Where ρ is density, u is velocity in x direction, t is time, η is dynamic viscosity, and F is body force. The Navier–Stokes equations describe the motion of fluid and they are formed by applying Newton's second law to fluid motion, together with the diffusing viscous term and a pressure term. In addition to the Navier-Stokes equations, equations of state such as the ideal gas law are also implemented for compressible and non-isothermal-flows [83].

3.1.2. Reynolds Number

Behaviour of the fluid flow is strongly influenced by how the pressure, speed, density and viscosity vary as well as the shape and size of the object. The dependence of the flow patterns on speed, viscosity, density and length can be expressed in terms of single quantity known as the Reynolds number [85]. Reynolds number is a non-dimensional constant which provides information about the characteristics of the aerodynamic flow and it defines the ratio of inertial to viscous forces within the flow [86]. Reynolds' investigation not only identified the various region in the pipe flow, but made some critical observations: “...*the general character of the motion of the fluids in contact with solid surfaces depends on the relation between a physical constant of the fluid and the product of the linear dimensions of the space occupied by the fluid and the velocity*” [15]. This statement led to the dimensionless Reynolds number:

$$\text{Re} = \frac{\rho U_{\infty} l}{\mu} \quad (3.2)$$

Where U_{∞} , in vehicle aerodynamics, is the velocity of the vehicle, ρ is the fluid density and μ is the fluids dynamic viscosity and l is the characteristic length. Reynolds number can be defined as the ratio inertial to viscous forces in a given

fluid [15]. Therefore Reynolds number is very high in vehicle aerodynamic flows where inertial forces dominate and low for the flow of highly viscous oil. The value of Reynolds number defines whether the flow is laminar or turbulent, the critical region where the flow takes a transition from one to the other is approximately 5×10^4 and can be said to be fully turbulent at 10^5 in air [86]. The vehicle velocity for our work is 26 m/s with corresponding Reynolds number of around 9.02×10^6 , length of 5 m (typical van), air density of 1.225 kg/m^3 and air dynamic viscosity of 1.85×10^{-5} . Therefore the flow is fully turbulent.

3.1.3. Energy Cascade

Energy cascade is also another important concept in understanding the turbulence. It describes the relation between turbulent eddy sizes in a fluid with an energy spectrum. Turbulent energy flows from large eddies to smaller ones until the energy is dissipated due to the viscosity. To illustrate this concept Richardson [87] adapted a sonnet by Swift: “*Big whirls have little whirls, which feed on their velocity, and little whirls have lesser whirls and so on to viscosity*” [88] This process (Cascade) of larger eddies breaking up into smaller and smaller ones is the key to understanding turbulence. Broadly speaking, the mean flow determines the largest eddy sizes, and the viscosity of the fluid governs the smallest eddy sizes and the intermediate scales ensure cascading transfer of energy across the range [89]. The distribution of eddy sizes in turbulent fluid is continuous in reality but for the convenience it is categorised into discrete ranges. Supposing a large eddy Reynolds number, Re_l is defined based on the eddy length scale (l_e) and its velocity (U_e) it can be shown that it is of the same order as Re for the mean flow [90]. The reason for this to happen is that the characteristic velocity and length scale of the eddy is proportional to the corresponding mean flow values. This shows that inertial effects dominate the large eddies and they are largely independent of viscosity. In summary, the three categories of eddy sizes within turbulence are all affected by different mechanisms each of which is present in vehicle aerodynamics.

3.1.4. Laminar and Turbulent flow

Fluid flows can, broadly speaking, be classed as laminar, transitional and turbulent. In the laminar flow, molecules move in a structured and orderly fashion, and moves parallel to the wall. Air flows smoothly with no turbulent perturbations and appear to behave rather like a stack of flat sheets over each other. Transitional (Transitional flow is a mixture of laminar and turbulent flow with irregular fluctuations) flow contains some instability and turbulence can be described as “a chaotic and random

state of motion in which the velocity and pressure changes continually with time in substantial regions of the flow'' [91]. The state between the laminar and the turbulent is called transition and it is largely governed by the value of the Reynolds number. For example for a flat plate transition occurs at the Reynolds number of around $5 \cdot 10^5$ [79]. Many practical applications experience turbulent flows such as swirling of the blood through our hearts.

Leonardo Da Vinci reported some of the earliest observation of the turbulence in the late fifteenth and early sixteenth centuries. In his experiments, he placed various objects in shallow river stream to obstruct the free-stream in order to induce tumbling and swirling flows. Fig. 3.1 shows an example of turbulence.

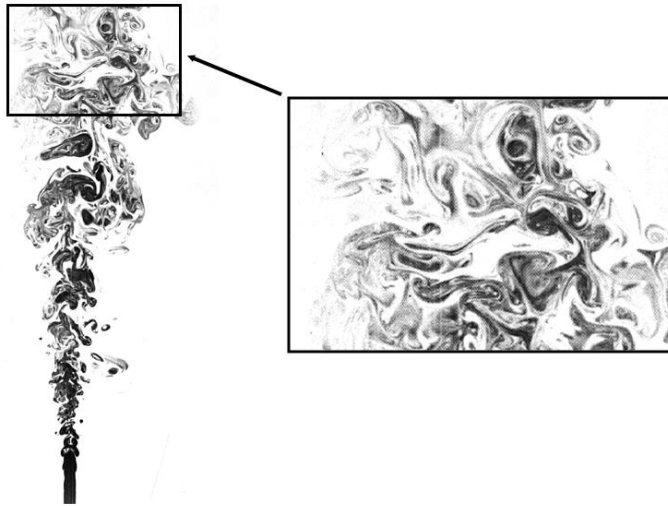


Figure 3.1 Example of turbulence (Visualisation of jet flow) [91]

Turbulence property of the upcoming air, is an important factor controlling boundary layer behaviour. Level of turbulence can significantly modify the behaviour of boundary layer and also flow around the vehicle. Increasing the flow stream turbulence tends to move the boundary layer transition position forward, but the increased turbulence can also help to keep the flow attached [85].

The most important factor which characterises the turbulence is the turbulence intensity of the stream-wise velocity fluctuations (I_v). It is measured by the ratio of the standard deviation of the velocity fluctuations to the mean velocity [85].

$$I_u = \frac{\sqrt{\overline{u^2}}}{\overline{U}} \quad (3.3)$$

Where u is the increase or decrease in velocity above the mean value \overline{U} .

There are also associated I_v and I_w for the flow components of v and w for different directions [85].

3.1.5. Boundary layers

Since air is a Newtonian and hence viscous fluid, its aerodynamics is also characterised by the no slip condition which states that at a solid surface, the velocity of the fluid relative to the surface is zero [92]. This results in a region known as the boundary layer close to the surface where the velocity rapidly increases from zero and approaches the free stream velocity [93]. Viscosity of the air is small compared to water, but this property plays a significant role in how airflows interact with solid bodies. The average velocity of the air molecule at the solid wall is zero, no matter how fast the air flows over them, and it is called no-slip condition [92]. The velocity rapidly increases from zero in the surface to the free-stream value at the nominal distance above the wall. This region is called boundary layer. The boundary layer thickness, δ , is defined as the distance from the wall to where the velocity reaches $0.99 U_\infty$ [94]. If the Reynolds number is high enough, the boundary layer has four distinct flow regions described in Fig. 3.2.

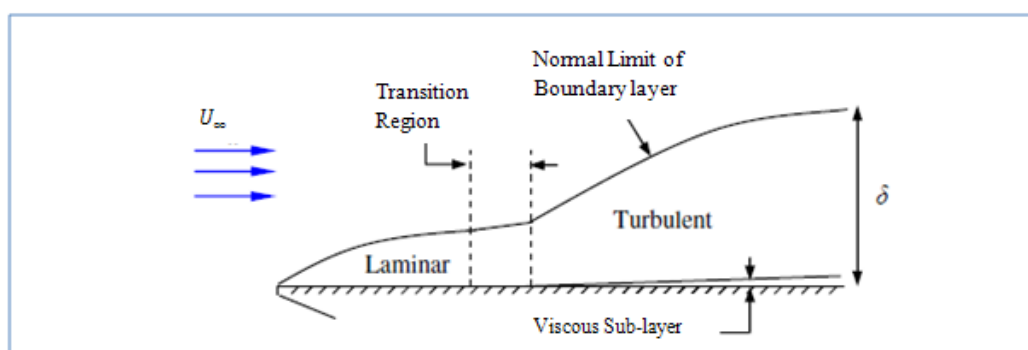


Figure 3.2 Illustration showing the structure of the boundary layer [92]

Flow is laminar at the leading edge and as the instability begins as the thickness of boundary layer increases and transition occurs. Transition region is small as the turbulent eddies within the boundary layer develop rapidly and dominate the layer. Underneath of the turbulent region is the viscous sub-layer which is laminar as the

turbulent eddies must die close to the surface [92]. The velocity gradient of the turbulent flow is larger than of the laminar part close to the wall.

The presence of the boundary layer and the energy it extracts from the free-stream leads to viscosity drag force which acts tangentially to the surface. This is expressed as the shear stress given by:

$$\tau = \mu \left(\frac{du}{dy} \right)_{y=0} \quad (3.4)$$

Where $y = 0$ is the wall surface. Clearly when the velocity gradient is larger in turbulent boundary layers, the shear stress will be greater on adjacent walls compared with that in the laminar boundary layer. In turbulent boundary layer, turbulent eddies mix the flow and faster moving air molecules are drawn in from the free-stream, therefore they contain more kinetic energy. This principle has been exploited in the design of golf balls, where instead of smooth surface, irregularity has been placed in order to keep the flow turbulent and causing the flow to stick to the ball for a longer distance compared with the smooth ball. The drag coefficient of the golf ball is 5-7% less than a smooth one at low spin velocities [95].

3.1.6. Pressure Gradient and Flow Separation

The pressure gradient is an important parameter which directly affects the behaviour of boundary layer. If the pressure gradient is such that over a range of x it decreases with distance x downstream, the pressure gradient with respect to x is therefore negative (favourable), the velocity in the boundary layer, U increases with x [96]. Likewise in the presence of an external rising pressure with x , or positive pressure gradient (adverse), the opposite effects occur [81]. In the case of adverse pressure gradient the flow within the boundary layer has to overcome not only the wall shear but also pressure forces opposing its motion. The relative decrease in velocity in the strata close to the surface (boundary layer) will be more affected as a result of presence of shear wall as well as adverse pressure gradient. Flow separation is a phenomenon that occurs with aerodynamic flows around bluff bodies [86]. Longitudinal pressure gradient (dp/dx) is the primary factor to determine whether the flow past a body is attached or separated. Flow remains attached if the pressure increases in x direction and it is termed as favourable pressure gradient, ($dp/dx > 0$). It can be seen as air accelerates past the leading edge of an airfoil from high to low pressure. Liquid generally flows from the region of high pressure to region of low pressure. Flow separation occurs when the pressure decreases along the x

direction (adverse pressure gradient, ($\frac{dp}{dx} < 0$)) and where the boundary layer cannot maintain enough energy to continue following body contours and it breaks down. The position of separation is given by the condition that the velocity gradient perpendicular to the wall vanishes at the wall, i.e. the wall shear stress (τ_w) vanishes [97].

$$\tau_w = \mu \left(\frac{du}{dy} \right) = 0 \quad \text{Separation [97]} \quad (3.5)$$

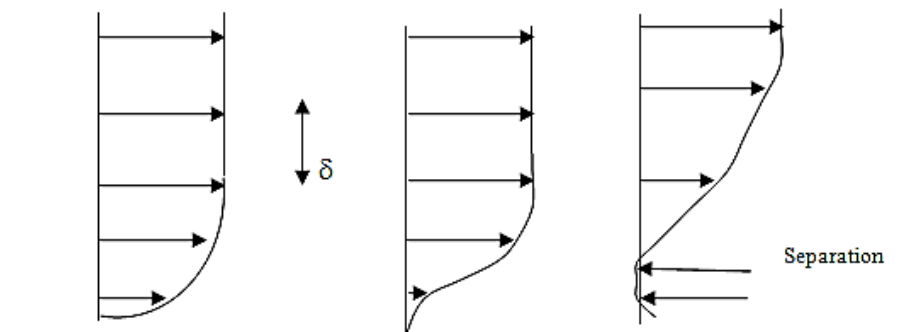


Figure 3.3 Profile of boundary layer separation

Downstream of the separation point the shear layer either passes over the region of the circulating fluid and reattaches to the body (separation bubble) or forms a wake and never reattaches to the body [97]. It normally occurs on the rear part of the airfoil which experiences pressure recovery from mid cord low pressure to the ambient pressure at the trailing edge.

3.1.7. Drag or shape factor

The total force resisting the motion of a road vehicle comes from the following factors [85] :

- Rolling resistance of the wheel (friction)
- Aerodynamic drag

The aerodynamic drag dominates at the speed above 60-70 km/h and there are considerable economic and performance advantage to be gained from drag reduction. Drag is an aerodynamic force that opposes the objects motion through the fluid. It is a mechanical force and is generated by interaction of the solid body with a fluid. Drag is generated by the difference in the velocity between the object and the

fluid as shown in Figure 3.4 [98]. Viscous effects (boundary layer) and pressure effects are two major sources of drag, these are termed viscous and pressure drag respectively. Pressure drag is usually larger than the viscous drag which is due to pressure difference and is associated with the large energy-containing eddies which are abundant in the wake, comparing to the viscous drag which is present in the boundary layer.

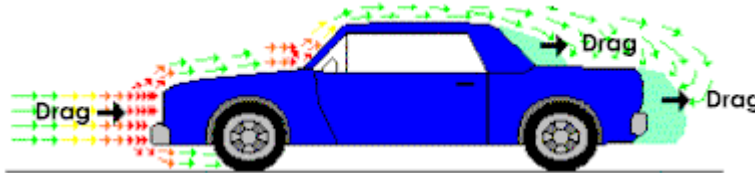


Figure 3.4 Drag force [98]

Apart from the large-scale eddies in the wake, there are series of vortices which are initiated further downstream behind the vehicle. They are created on the side of the windscreen because of the pressure difference between the side and roof of the vehicle. They also increase the drag of the vehicle.

$$D = 0.5 \rho A C_d V^2 \quad (3.6)$$

Where ρ is the density of the fluid, A is the area, V is the velocity and C_d is Drag coefficient.

The drag coefficient, in fluid dynamic is a dimensionless quantity that is used to quantify the drag or resistance of an object in a fluid [99].

$$C_d = \frac{D}{0.5 \rho A V^2} \quad (3.7)$$

It is often more useful to characterise the aerodynamic shape of a vehicle using drag coefficient as it takes out the effect of the speed as well as the projected area. Figure 3.5 shows components of the drag force. By adding two forces together it would give the drag on the surface element [85].

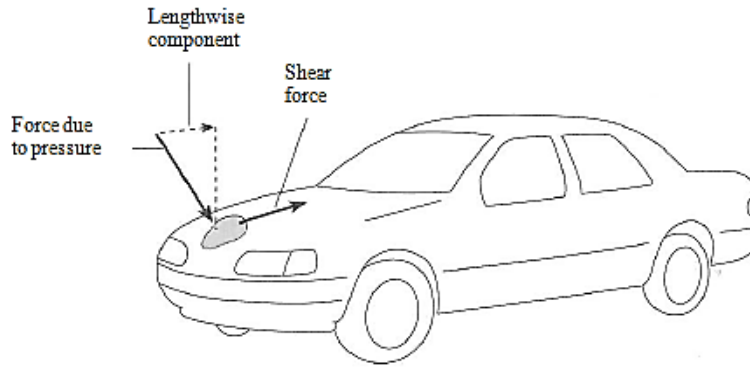


Figure 3.5 Shear and pressure force on a vehicle [85]

Viscous drag which is due to frictional shear (Interaction and resistance of flow over a surface) is relatively small for the conventional road vehicles, but it can be in the order of 30% for the typical modern car [85]. The greater part of aerodynamic drag force comes from the fact that the pressure in front of the vehicle is higher than the one in the rear of the vehicle. Number of elements effects the pressure distribution around a vehicle. The most important factor is the boundary layer. When air flows past a vehicle, it appears to stick to the surface and at the surface there is no measurable relative motion. The individual molecules move randomly at the surface and their average speed parallel to the surface is zero. The dimensionless laminar and turbulent boundary layer thickness, referred to the length of the plate, l , according to Blasius equation is [81]:

$$\frac{\delta_{Laminar}}{l} = \frac{4.91}{\sqrt{Re_x}} \quad (3.8)$$

$$\frac{\delta_{Turbulent}}{l} = \frac{0.382}{Re_x^{(1/5)}} \quad (3.9)$$

Where Re_x is $Re_x = \rho u x / \mu$

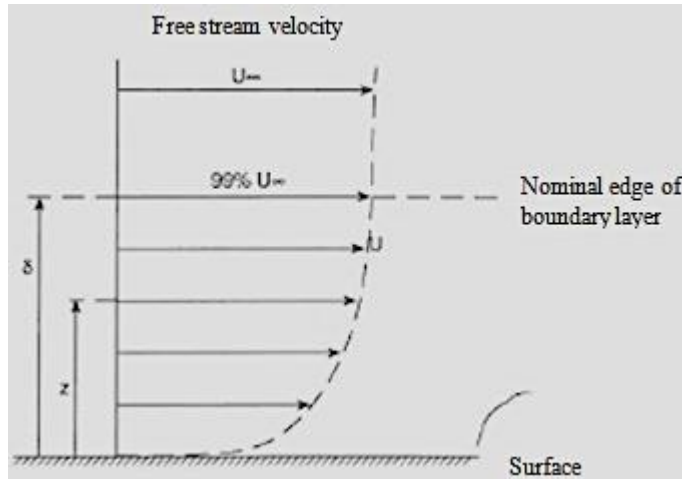


Figure 3.6 The variation of the velocity in a boundary layer [85]

Thickness of the boundary layer grows with distance but does not exceed more than few centimetres on a car travelling at a normal speed as it is calculated below. Despite this layer is very thin, but it holds the key to understanding how air flows around a vehicle and how the drag force is generated [85].

$$\frac{\delta_{Turbulent}}{l} = \frac{0.382}{Re_x^{1/5}} \quad (3.10)$$

$$\frac{\delta_{Turbulent}}{0.852} = \frac{0.382}{1.22 \times 60 \times 0.85 / 1.85 \times 10^{-5}^{1/5}}$$

$$\delta_{Turbulent} = 0.00089765$$

Where $\rho = 1.22$ (kg/m^3) is the density of the air at 20°C , $u = 60$ m/s is the maximum velocity of the flow in the wind tunnel for our experiments, $x = 0.85$ is the distance to the front of the model and $\mu = 1.85 \times 10^{-5}$ is the dynamic viscosity of the air at 20° .

In the turbulent boundary layer, the flow is still streamlined and it still follows the contours of the body. The turbulence motion is of very small scale. There are important differences in the properties of two types of boundary layer. The laminar layer produces less drag due to friction with the surface. Turbulent boundary layer produces less pressure drag since the flow is more likely to follow the contours of the body and the turbulence delays the separation [85]. Figure 3.7 illustrates how the

boundary layer influences the pressure distribution on a simple case of two-dimensional flow around a smooth symmetrical shape.

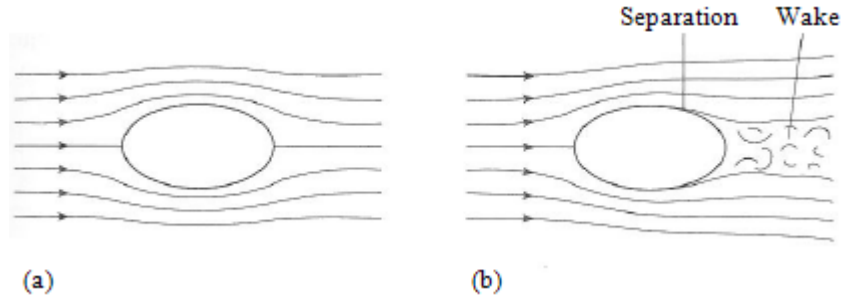


Figure 3.7 The effects of viscosity [85] (a) Theoretical flow pattern obtained when the effect of viscosity are ignored; (b) typical actual pattern for a real air flow.

The relative air speed is brought to zero at the nose, the flow accelerates and reaches a high relative speed at the widest part and then it slows down as it approaches the tail. There will be a high pressure near the tip of the nose where the speed is low and low pressure on the wide area where the speed is high according to the Bernoulli equation [79]:

$$P_1 + \frac{\rho}{2}V_{m1}^2 + \rho gh_1 = P_2 + \frac{\rho}{2}V_{m2}^2 + \rho gh_2 \quad (3.11)$$

Height is insignificant in road automotive air flow, therefore it will be ignored and it is assumed that the flow is incompressible and air density does not change with velocity for low speed ($Mach \leq 0.3$) (Mach number is the air velocity divided by speed of sound):

$$P_1 + \frac{\rho}{2}V_{m1}^2 = P_2 + \frac{\rho}{2}V_{m2}^2 \quad (3.12)$$

Where P is the static pressure, ρgh is dynamic pressure, V is the mean velocity and ρ is the density [79].

Mach number of the highest velocity in this work (60 m/s) is 0.18 which is below the value at which flow becomes compressible and its density changes. Without the influence of viscosity the streamline would close up behind the shape and produce a symmetrical pattern shown in Figure 2.12 (a), in reality because of effect of the viscosity, the streamlines around the shape would look more as in Figure 2.12 (b),

this is because the viscosity causes the energy in the air flow close to the surface to degrade and therefore the energy is lost. As a result of this the air cannot return to its initial values of speed and pressure, instead a wake of slower moving air is formed and the boundary layer may even separate. In this flow condition the pressure distribution is no longer symmetric and the pressure on the rear portion of the object is on average lower than the front and therefore there will be a rearward drag force. The drag force arising this way is known as form or pressure drag. In modern design it accounts for one third of the total drag [85]. In reality flow around a vehicle is highly three-dimensional and many of the approximations to two-dimensional flow that are commonly used in aircraft aerodynamic analysis cannot be used for road vehicles. Figure 3.8 shows some aspects of the three-dimensionality of the flow around a car [85].

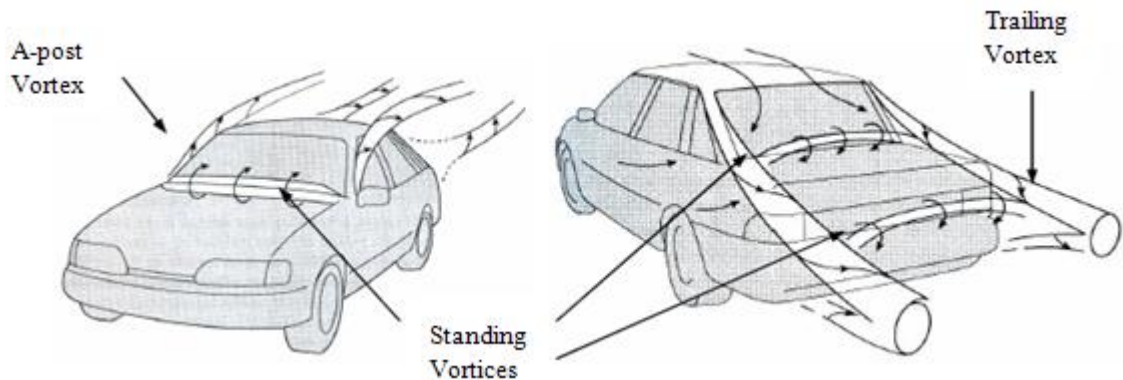


Figure 3.8 Illustrations showing the vortex structure around a vehicle [85]

Most vehicles produce lower pressure on the top surface than underside and as a result lift will be generated. Another consequence of this is that the air tends to flow from the high pressure underside to the low pressure on top, resulting in the production of vortices in the wake as shown in Figure 2.13 [85]. They are called trailing vortices and large amount of energy goes into the formation of these large swirling masses of air and therefore they represent source of drag. The vortices draw air away from the rear of the vehicle, creating a low pressure there, and thereby pulling the air down. Because the air is swirling with high speed, the pressure in the vortices is low, therefore any surface exposed to the influence of a vortex will be subject to a reduced pressure. A reduced pressure over the rear of the vehicle will obviously increase the drag. this contribution to drag is commonly called trailing vortex or induced drag [85]. ‘Drag factor’ is the more universal measure of drag defined as $C_d A$ which allows comparisons to be made between large and small objects with the same C_d [100].

3.2. Flow Separation Control

The boundary layer control includes any mechanism or process through which the boundary layer flow is caused to behave differently than it normally would where the flow developing naturally along a surface [101]. The science of the flow control originated with Prandtl (1904), who introduced the boundary layer theory, explained the physics of separation phenomena and described several experiments in which the boundary layer was controlled [101]. In order to build a foundation and to provide background to the research, a literature review survey is carried out which included a discussion of all the major methods of boundary layer low speed flow control:

3.2.1. Flow Control Methods

Purpose of all these methods is to affect the whole flow in a desired direction by influencing the structure of the boundary layer. The methods that have been used to control the separation have been as below:

- Removal of low momentum near wall flow
- Re energising near wall flow and changing the wall static pressure through the manipulation of surface geometry

The past research has shown that the above methods tend to assist to either delay the separation or even prevent the boundary layer to separate. By introducing a system to reenergize the flow near the wall, and therefore higher momentum flow near the surface, the separation may be delayed or even eliminated. The various techniques that have been developed over the years to control the flow are classified into two main categories:

- Passive control (requiring no auxiliary power)
- Active control (requiring energy expenditure)
- Or the combination of both which has recently been developed (active/passive).

The passive control simply means, no power source, and that would usually prove to be better than the active control with the power source which require the manipulation of the structure for the power source and usually outweighs the

advantage of the active control over the passive. For example for the active flow such as suction the structural modification will be required but for passive control simply without the power source it won't be as complex and the result will be more appreciated. Active control is further divided into predetermined or reactive. The predetermined active control DoEs not have a feed back in order to adjust the input but the proactive is simply an active control with feedback in order to adjust the input. The summaries of the principals involved in both passive and active flows are as following [81]:

- **Passive**

- Vortex generators

- Geometry manipulation

- Passive cavity

- **Active**

- Suction

- Blowing

- Air jet vortex generator

- Heating, cooling

- Mems

- Motion of the solid wall

In vehicle aerodynamics, mainly passive flow control methods have been practiced such as vortex generators and geometry manipulation. To be able to do the aerodynamic optimisation the method of geometry manipulation has to be applied. In this particular method the geometry will be manipulated and the best shape will be chosen with the means of aerodynamic optimisation. In design of the road vehicle, most important factor is drag force and considerable performance and economic advantages is gained by drag reduction and producing a vehicle with a smoothly controlled continuous surface as the gaps and discontinuity produces drag. Gaps and discontinuity increase the drag by increasing the boundary layer thickness and turbulence. By extending the laminar boundary layer, less surface friction drag will be produced. By suitable shaping and maintain the favourable pressure gradient and moving the maximum thickness further down, laminar boundary layer can be

maintained and as a result surface drag is decreased. Keeping the flow as far attached as possible is the most effective way in reducing pressure drag. If the pressure rise is gradual, the energy from the free stream will be fed into the boundary layer fast enough to prevent the separation. Therefore the cross section should decrease gradually for that to happen. Streamlining is important factor in drag reduction. Therefore for the cars, ideal shapes are thinner and longer. As it is more appropriate to minimize the drag for a given volume rather than given projected area. Lift-induced drag can also be simply decreased by minimizing the lift. Reducing the aerodynamic drag can produce a major improvement in fuel consumption. Also gain in performance in terms of both speed and acceleration. Figure 3.9 shows how the teardrop shape modifies and reduces the turbulence and the separation on the rear of the vehicle. Consequently it reduces drag force by 15% [102].

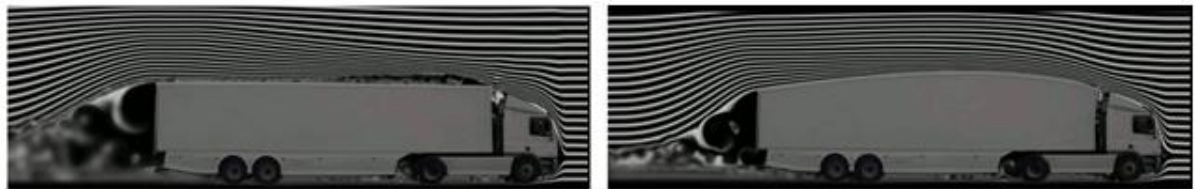


Figure 3.9 Image demonstrating the pressure recovery in the wake of the Don-Bur 'teardrop' design (Right) relative to a standard trailer (Left) [102]

3.2.2. Advantage of Flow Control

Modern passive and active flow-field control is a rapidly emerging field of significant technological importance to the design and capability of a new generation of forthcoming air-vehicle systems. Generally it is desired to postpone separation so that form drag is reduced, lift is enhanced and pressure recovery is improved. Therefore less drag, reduced engine power and noise, therefore more payload and less fuel are the consequences [101].

3.2.3. Passive drag reduction

Increasing the fuel economy is the primary objective of drag reduction on vehicle, since it is beneficial to the environment. This aspect of the aerodynamic is very challenging for bluff shapes such as trucks and large bluff vehicle like ambulance. Drag reduction principles are relatively straight forward in the opinion of Cooper [103]. Drag reduction, by using the method of streamlining in the automotive

industry, was widely adopted throughout the automotive industry between 1920's and 1940's, however the resulting teardrop shaped vehicle were impractical and uncomfortable due to the space restrictions [100]. Oil crisis on 1973 changed the public perception and drag reduction became accepted as an essential part of design process [100, 103]. One of the most comprehensive drag reduction investigation was carried out in a wind tunnel at the university of Maryland in the 1950's [103]. Several devices such as roof fairing, side skirts and seals to bridge the gap, were added to the baseline. With minor changes, drag reduction as much as 50% were gained and it was shown the drag can be halved if these modification are applied to the boxy vehicles of that time. The study also showed the significant effects of rounding the leading edges to bluff shapes to lower drag through minimising pressure gradient and therefore controlling the separation. Other techniques such as adding low-drag fairing and raking back the front face of trucks are also useful. Figure 3.10 clearly demonstrate how modifying the shape and also adding add-ons decreases the drag coefficient. Grey area indicates the drag coefficient for vehicles without modifications and add-ons (between 0.7-1.1). Whereas the drag coefficient has been lowered to less than 0.5 for vehicles with modifications and add-ons.

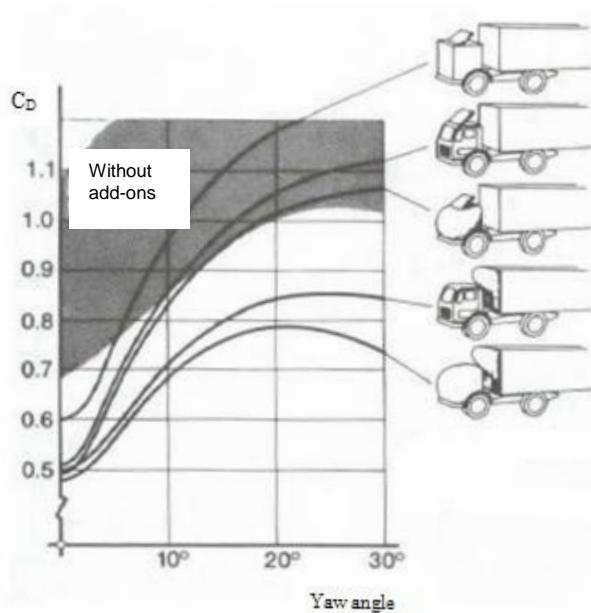


Figure 3.10 Effect of shape of the truck on the drag coefficient [29]

Gary [104] and Charwat [105] investigated the effectiveness of fairings for commercial vehicle and utility box trailer. Drag reduction of 30% was achieved for the box trailer in zero yaw angle and 60% for yaw angle of 30° . Modification to the

rear part of trucks in the form of boat-trailing is also very effective in reduction in drag [106].

3.3. Fuel Consumptions

As noted earlier, interest in the aerodynamic performance of Emergency Response Vehicles, is stimulated by the need to improve fuel economy and reduce emissions from their fleet operations. Since there are not any previous study on the fuel consumption of the Emergency Response Vehicles, the improvements in fuel consumption resulting from the reduced aerodynamic drag of the optimised design are quantified based on the trends identified for Heavy Goods Vehicles. Comprehensive data on the fuel consumption of the HGVs are available in studies [16, 19, 37]. The study [16], for example, found that at 90 km/h, a 20% aerodynamic drag reduction results in a 10% improvement in fuel economy, whereas at 60 km/h, in order to achieve the same improvements fuel economy of 10%, aerodynamic drag has to be reduced by 30%. At lower speeds, significantly larger improvements in aerodynamic drag are required to achieve the same reduction in fuel economy and for low speeds (≤ 15 km/h) the influence of aerodynamics on fuel consumption may be neglected. The relationship between drag reduction and fuel economy improvement for speeds of 30, 60 and 90 km/h presented in [16] are shown in Table 3.1, with similar findings presented in [37].

Vehicle Speed (mph)	Aerodynamic Drag Reduction to Increase Fuel Economy 1%
60	2%
40	3%
20	6%

Table 3.1 Relationship between drag reductions and fuel economy improvement for tractor trailer trucks [16]

3.4. Three-Dimensional Flow (Airflow Pattern)

Three dimensionality of the flow involved makes the vehicle aerodynamic such a challenging subject. In the beginning of the 20th century, the research on the external aerodynamic was mainly focused on aviation industry (driven by war effort) where flow is mostly attached. This occurs because the general lay out of the airplane is fuselage and the wing and they have very small geometrical gradient which induce small pressure gradient. In contrast, road vehicles are blunt bodies and very compact and are not amenable to gentle curvaceous contours. Therefore the flow field around

the ground vehicle is more complex than for an airplane and a number of factors needs to be considered.

3.4.1. Pressure Distribution

One of the simplest forms of interpreting the local flow structure is observing the pressure distribution. C_p (defined in equation (3.13)) is a dimensionless pressure coefficient and a very useful parameter for the following reasons:

- Characterizing common flow features
- Making comparison between different vehicles

$$C_p = \frac{P - P_\infty}{\frac{1}{2}\rho V_\infty^2} \quad (3.13)$$

Where P and P_∞ are static and free stream pressure respectively, ρ is the density and V_∞ is the velocity. When vehicle moves through the air, flow stagnates locally and its velocity decreases to zero ($C_p = 1$). The size of these high pressure regions (stagnation) depends on how streamlined the front of the vehicle is. Also the separation occurs due to the sharp changes in the geometry as the air flows over the bonnet of the vehicle and produces a separation bubble downstream. Smooth radius, in these region, can cause the flow to accelerate and move faster and generate suction giving negative value of C_p , see Figure 3.11. Figure 3.11 also indicates the area of high and low pressure and where the modifications need to take place in order to lower the drag coefficient.

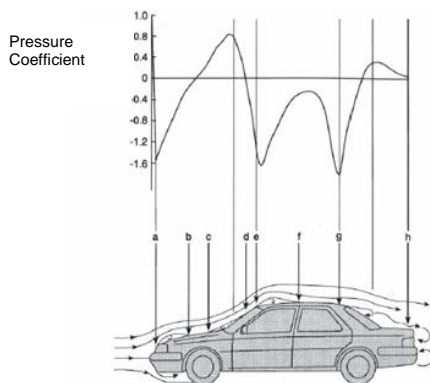


Figure 3.11 Illustration showing the surface pressure distribution along the centreline of a vehicle [85]

Before flow reaches the centre of the roof, flow phase changes from separation to reattachment around the base of the windscreen leading to a trapped vortex and also over the leading edge of the roof. Sudden reduction in the cross-section of the vehicle and slanting windows leads to strong adverse pressure gradients which include an extensive region of separated flow (the wake).

3.5. Summary

- The Navier–Stokes equations describe the motion of fluid and they are formed by applying Newton's second law to fluid motion. Reynolds number is also a dimensionless number describing whether flow is laminar or turbulent.
- Broadly speaking, flow and its boundary layer to the surface can be classed as laminar and turbulent.
- Turbulence and low pressure region causes the flow to leave the surface which is known as flow separation. Flow separation increases the drag force.
- There are several methods to control the flow separation such as geometry manipulation which is mainly used in vehicle aerodynamic drag reduction.
- Geometry manipulation has been used in this work in for the aerodynamic optimisation of Emergency Response Vehicles.

4. Computational Fluid Dynamics

Three-dimensional flow can be described in terms of partial differential equations and they cannot be solved analytically. There can only be an approximate numerical solution to these equations. Discretization method, which approximates the differential equations by a system of algebraic equation, has to be used. The approximations are applied to small domains in space or time, so the numerical solution provides results at discrete locations in space and time. The accuracy of the numerical solution depends on the quality of discretization used. This process is known as Computational Fluid Dynamics. Computational Fluid Dynamic (CFD) numerically solves the governing equation of fluid flows by the ability of microprocessors that can handle millions of calculations [107]. CFD has been developed in terms of maturity in recent years. This chapter includes a comprehensive description of CFD methodology which will be used in the next chapters.

4.1. CFD

Computational Fluid Dynamic (CFD) is a way to analyse of fluid flows by means of computer based simulation as mentioned before. This technique is very powerful and it covers wide range of industrial and non-industrial applications [91]. This work focuses on the analysis of the flow field around the vehicle by means of CFD as well as experiment which will be explained in details in upcoming chapters. The flow field around the vehicle is very complex. Therefore the efficiency of a CFD simulation depends on many factors. Model geometry and its integration into the physical domain, choice of suitable turbulent model and grid generation are significant factors that will determine the level of success of CFD simulation. Efficiency of an aerodynamic simulation depends on many factors as the flow field around the vehicle is very complex. Model geometry creation and its integration in the physical domain, grid generation and also suitable numerical scheme are very important factors that can decide the level of success of the simulation process [18].

When power of computer is used to simulate the behaviour of fluids, it involves a number of key elements. First, a mathematical description of the physics of fluid flow is required for the problem of interest. In order to represent the problem and achieve the solution, many different algorithms need to be used. Following section illustrates some of the key features of CFD application.

4.1.1. Discretisation

Flows such as slow flow that are geometrically simple and allow the simplification of the governing equations can often be described by analytical solutions which consists of functions that can be evaluated at any point in a given fluid domain. However, for the general governing partial differential equations (PDEs), or for geometrically complex domains, analytical solutions do not exist. Instead system of algebraic equations which represent these PDEs must be derived, this process is called discretisation. This can be done either by approximating the solution of the PDEs by piecewise polynomial function or by approximating the partial derivatives by finite differences. In either case, the domain is represented by a grid of points (or nodes) at which value of the dependent variables are to be found. Discretisation method will define the form of the system of algebraic equations. there are number of methods in which the governing PDE's can be discretised and are described below [64]:

4.1.2. The Finite Difference Method

The finite difference method involves Taylor series expansions which produce approximations to the partial derivatives of the governing PDE's at the grid points [44]. This method is normally applied to, structured networks of grid points, although the regularity of grids allow for high order differencing approximations, thereby ensuring high accuracy. The main disadvantage is that the conservation properties such as mass and momentum, are rarely enforce unless great care is taken [44]. Also, the particular requirement for structured grids is not always flexible enough to deal with the complex geometries often encountered in science and engineering. Also the application of the Taylor series expansion results in an error which is inherent in the calculation. This error tends to zero with the grid spacing so it can be suppressed to a large extent and this is minimized by using higher order discretisation methods.

4.1.3. The Finite Element Method

Intensive period of finite element method (FEM) research occurred between 1940 and 1960 and it was developed then and its origin were in structural analysis [108]. In order to provide insight into stress distribution of the component, the principle is to discretise a given structure into small elements for stress analysis and repeat the stress field using analytical functions of nodal values and re-assemble these results. Unstructured elements, which are more flexible in terms of shape to fit the complex

geometries, were used originally in the method to make it appropriate for fluid mechanics [108]. In 1960, FEM implementation into CFD community begun when its formulation was generalised so that it would be suitable for CFD. One of the greatest strength of FEM is its ability to discretise a fluid domain with irregular elements to fill the spaces with practically any shape [64]. In the derivation of the discretised equations, a (typically low-order polynomial) interpolation function describes the way in which the dependent variable, ϕ (Such as pressure and velocity for fluid flow), varies across each individual element, as a function of the values of ϕ at the element nodes. Therefore the FEM is based on the approximating the solution rather than the approximating the equations as with finite differences. Thus the result is still set of algebraic equations to determine the nodal values of ϕ .

4.1.4. The Finite Volume Method

Direct physical interpolation is the philosophy behind the control volume method and finite volume method (FVM) [64]. In this method the solution domain is divided into non-overlapping control volumes so that a computational node positions at the centre of a control volume., see Figure 4.1.

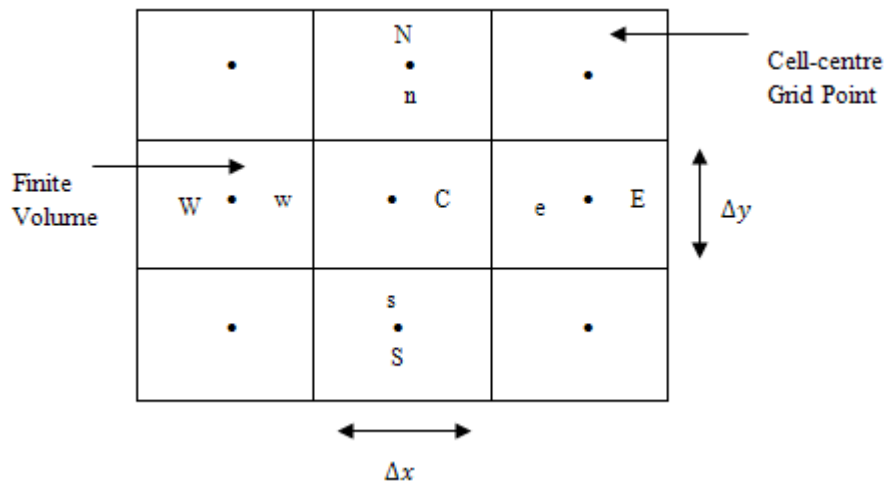


Figure 4.1 Illustration of the finite volume method for a two-dimensional grid [64].

Once the fluid domain is discretised, the goal is to calculate the solution variables are at the cell centres. The differential equations describing the flow are then discretised for each control volume [64]. Next, these equations are numerically integrated over each individual control volume to evaluate the fluxes through each of the cell faces. For example, the integration process would find solution variable fluxes through faces n, e, s and w for the c control volume on the middle. This

method, by integration of the conservation quantities, ensures that mass, momentum and energy are conserved locally to each control volume, this is what makes FVM so attractive. Therefore the global conservation is ensured, whether the grid is fine or coarse, it will produce solution which exhibit exact integral balances [64]. The FVM discretisation method is utilised in the commercial code Fluent, which will be primary tool used in this study.

4.1.5. Pressure-Velocity Coupling

There are generally two approaches for solving the governing flow equations: segregated and coupled solver. They are Segregated and coupled. Segregated solver, which are explicit in nature, are used for incompressible flows and employ an iterative technique to reach a solution. Pressure and velocity coupling method is used to obtain the solutions for compressible flow problems which simultaneously solves the algebraic equation for pressure and velocity [109]. The flow around the bluff bodies, is comparatively slow, therefore segregated method for incompressible flow will be discussed. To ensure that pressure obtained from the momentum equations correspond to that of the continuity equations, the pressure-velocity coupling technique is applied. Semi-Implicit Method for Pressure Linked Equations (SIMPLE), designed by Patankar and Spalding in 1972, is the most popular method for achieving this. This is a robust guess-and-correct scheme for solving the pressure field such that continuity is maintained.

The pressure field is denoted by p^* and the iterative process starts by guessing the pressure field, this is the predictor step [91]. Velocities in the momentum equations are denoted by u^* , v^* and w^* and the values of p^* are used to solve for these velocities [81]. Since the obtained values of u^* , v^* and w^* are based on the guessed pressure field, continuity may not be satisfied, once these values are substituted into the continuity equation. For this reason, the continuity equation itself is used to give the pressure correction equation, namely:

$$p_{new} = p^* + p' \quad (4.1)$$

Where p' is the pressure correction. Therefore the new value of pressure, p_{new} will ensure that the velocity field agrees with the continuity equation more closely [81]. This is used to give the velocity corrections, which are given by:

$$u_{new} = u^* + u' \quad (4.2)$$

$$v_{new} = v^* + v' \quad (4.3)$$

$$w_{new} = w^* + w' \quad (4.4)$$

The updated values of p_{new} , u_{new} , v_{new} and w_{new} are then substituted into the momentum equation in the final step in the SIMPLE procedure, replacing the initial guessed p^* , u^* , v^* and w^* quantities. This process is repeated iteratively until the computed velocity field satisfies the continuity equation [81]. Since the equation (4.5) can also move towards divergence, the notion of under-relaxation needs to be applied. This technique involves applying a fraction, α , of the pressure correction:

$$p_{new} = p^* + \alpha p' \quad (4.5)$$

As sometimes the guessed pressure is too far away from the final solution, it is necessary to reduce the α , it then ensures that solution progresses without jumping too far from the final solution, therefore the probability of convergence is improved [91]. The default values of under-relaxation factors, for the commercial CFD code, are 0.3 and 0.7 respectively Fluent [46] for the current work, these value have proven to be suitable and they were not changed during the course of simulations.

4.1.6. Differencing Schemes and Accuracy

Order of discretisation scheme used, influences the accuracy of numerical scheme, which in turn depends on how calculations throughout the fluid domain are made. FVM requires the value of solution to be computed on cell faces, once the integral form of the differential equation has been established. Central differencing, which is second order accurate [109] calculates the face value using the average of adjacent cell centres. Central differencing is unable to determine the flow direction and that is one of its weaknesses. This means that if there is a strong convection current in the domain, the average would be inappropriate since the flow should be bias towards one side [91].

4.2. Grid Generation

Process of discretisation which is achieved through grid generation, is one of the most time consuming and difficult stages in applied CFD. This is, in fact, a process

of deciding where to make the calculations in a fluid domain. Quality of CFD results depends on the size and type of the grid as they determine the discretization error. Therefore by spending more time and generating a fine grid, the solution of the CFD calculations are improved. A good quality grid without sudden changes in structure will always provide better results to a coarse one. For three-dimensional geometry, this criteria will be extremely challenging. For the simple geometry, grids using Cartesian co-ordinate system can be used to discretise the geometries, but for the more complex geometries making more flexible gridding approaches are necessary. Following types of grid strategies are common [91]:

- Body-fitted grids
- Block-structured grids
- Unstructured grids

4.2.1. Body-fitted Grids

Methods based on body-fitted grid system have been developed to deal with curved boundary flows such as flow over an airofoil [91]. Body-fitted grids involve mapping the flow domain onto a computational domain with a simple shape [91]. Figure 4.2 shows an example of body-fitted grid for a simple geometry together with the equivalent Cartesian grid seen by the computer. This allows simple matrices to be employed without the need for time consuming and complicated conversion processes.

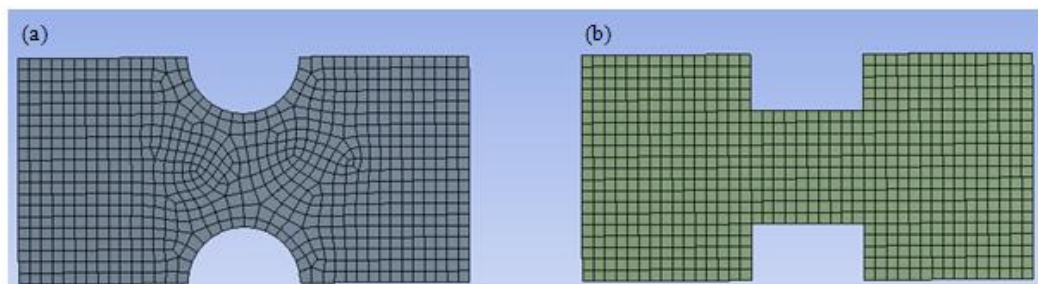


Figure 4.2 Schematic of (a) a simple body-fitted grid for flow past cylinders and (b) the computational grid onto which it is mapped (Own Figure)

4.2.2. Structured Grids

For more complex solution domains, decomposing the domain into sub-blocks is more appropriate, the sub-blocks can then be meshed more easily. Refined cells can

then be positioned where large gradient is expected in the flow field as it can be seen in Figure 4.3. Benefits of structured grids are that they are more accurate.

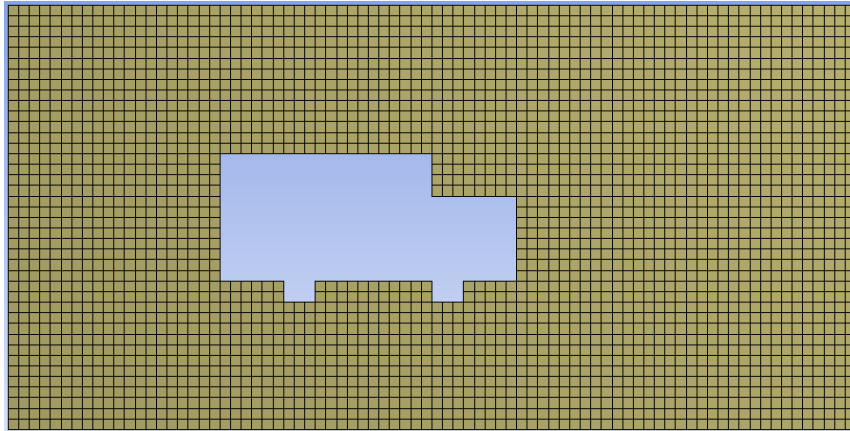


Figure 4.3 Illustration of a typical block structured grid (Own Figure)

4.2.3. Unstructured Grids

Using unstructured grid generation is another alternative, in unstructured grid each cell can be considered as an individual block in its own right [91]. Unstructured grid generation has two important advantages:

- 1) They can deal with complex geometry.
- 2) They don't require domain decomposition.

An example of unstructured grids using triangle cells is presented in Figure 4.4.

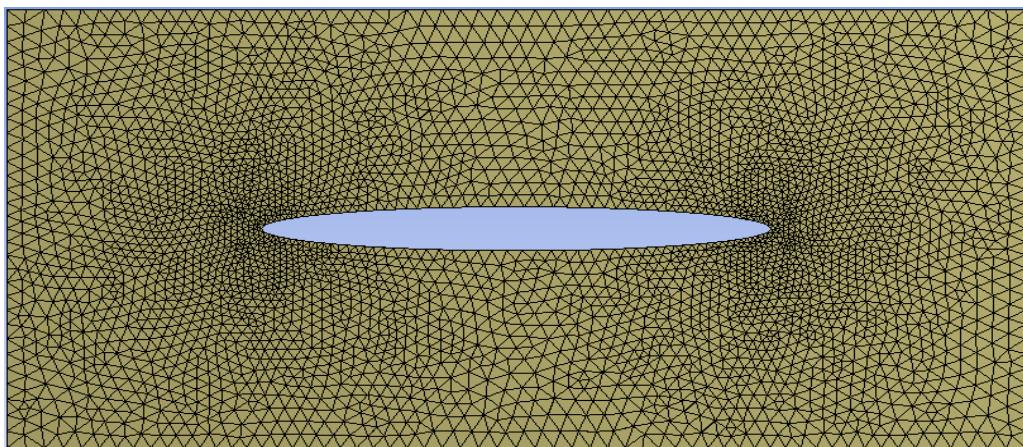


Figure 4.4 Illustration of triangular unstructured elements for a fluid domain surrounding an ellipse (Own Figure)

4.2.4. Good Practice

For obtaining reliable and accurate results, producing a high quality grid is very important. Despite this importance, there is not any standard procedure for gridding, which is probably due to the fact that there is wide range of CFD applications. Instead best practice guidelines describe very simple methods for maintaining good quality throughout [108]. For example, if the flow variable gradient is expected to reduce along a certain geometry, then high density cells can change into less dense cells. See Figure 4.5. In contrast, sudden jump from fine cells into coarse ones can lead to unstable solution behaviour. Also when two boundaries meet, care needs to be taken in order to maintain the uniform cell size.

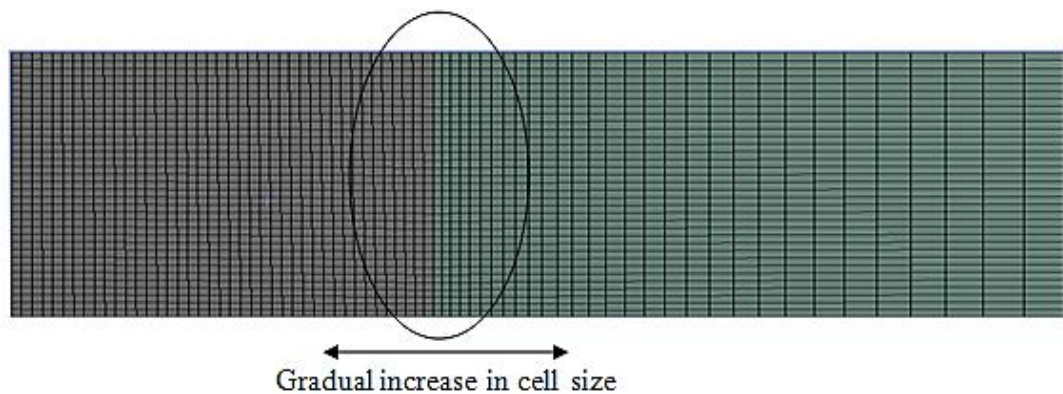


Figure 4.5 Illustration of good practice meshing (Own Figure)

4.3. CAD Models

Generic models can be created with similar dimensions using software such as design modeller but it would not contain the very details of the model. This technique can be used when the obtaining the real geometry is not possible or cleaning of the geometry would not be feasible.

CAD models of industrial parts are often not suitable for CFD meshing as they are created by designers for manufacture purposes and which may either be incomplete and/or too detailed, have imperfections like gaps, edge/face discontinuities, cracks, free vertices/edges/volumes, etc. This makes the CFD mesh generation particularly challenging and time consuming and may require several weeks to complete. Figure 4.6 shows a part of a CAD model geometry before and after repair. These can take the form of disconnected panels with fillets with a large number triangle faces that

represent the vehicle's external panels. These can be overcome by: (i) removing the fillets (where applicable), (ii) connecting panels by creating in-between faces, and (iii) merging triangles.

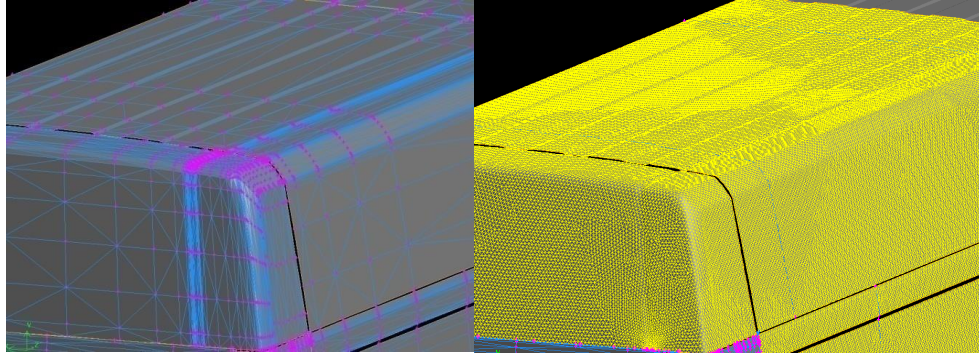


Figure 4.6 Examples of CAD model geometry before and after repair

4.4. Boundary Conditions

Appropriate boundary conditions are required prior to solution procedure once the governing equations are discretised with a suitable grid. In order to define a problem properly, a suitable combination of boundary condition types, to the fluid domain, need to be chosen. Some of the boundary conditions available in Fluent 13 [46] are as given below:

- Inlets (Velocity)
- Outlets (Pressure)
- Walls
- Symmetry
- Turbulence intensity and length scale

4.4.1. Inlet, Outlet and Symmetry Planes

A wide range of boundary condition types permit the flow to enter and exit the solution domain, and boundary data required depends on physical model selected. For example for incompressible flow, velocity inlet and pressure outlet are normally selected, and for compressible flows, mass flow inlet and pressure far field are selected. Inlet velocity defines the velocity vector and scalar properties of the flow at the inlet and it is intended for incompressible flow and is useful when the velocity is known at the inlet. For the pressure outlet, static pressure at the outlet boundary is

defined which is the static pressure of the environment at which the flow exhausts and it is usually assumed to be constant over the outlet. Pressure outlet must always be used when model is set up with pressure inlet.

Symmetry boundary condition is used to reduce the computational effort in problems such as vehicle inside the wind tunnel. It can be used when the flow field and the geometry is symmetric with zero normal velocity at the symmetric wall and zero normal gradient of all variables at symmetry plane and it is not valid for asymmetrical flow which can occur in the wake of a symmetrical body [92]. Symmetry boundary conditions assume that the flow is tangential to the surface with no transverse velocity components [91]. For analysing the flow field around a vehicle, it is essentially placed inside a large duct with a column of air passing through it. In the CFD simulations, there are no limits on the positions of the external boundaries. Not only side walls and the ceilings can be placed far away from the model but they can also be assigned a full-slip condition so that unrealistic boundary layers do not form. If the boundaries such as inlet and outlet are too close to the model, they can have a significant impact on the flow.

4.4.2. Walls

Wall boundary is used to bound the fluid and solid regions are the most common boundary type. The grid cells nearest to the wall are assigned a velocity of zero from the no-slip condition when the wall DoEs not move. For viscous flow, the no-slip condition is enforced at the wall which ensures that the tangential fluid velocity equals to wall velocity and normal velocity components are equal to zero. The grid cell nearest to the wall is assigned a velocity of zero from the no-slip condition. However difficulty with walls is that the development and the growth of the boundary layer yields many features including intermediate and small scale turbulence.

Broadly speaking there are two approaches to simulating near-wall turbulence, the first is to solve all the way from the free-stream to the wall. However, this requires a boundary layer grid containing a very high cell density adjacent to the wall [110]. The second method is to use wall functions [110] which essentially model the mean velocity profile near to the wall, see Figure 4.7. Consequently, a coarse grid can be used with the wall function bridging the gap between the computational nodes on the wall surface and those in the turbulent core.

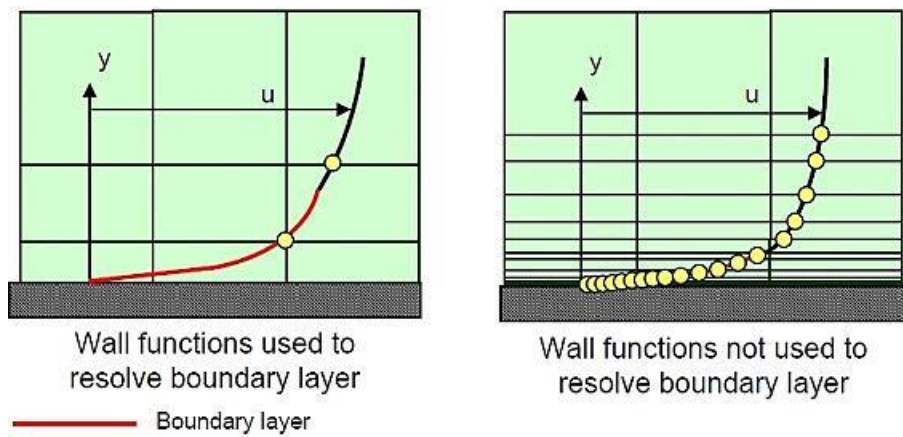


Figure 4.7 Representation of Wall Function approach vs fully resolving the boundary layer [111]

Wall functions are universal because they are characterised in terms of two variables, namely the time-averaged dimensionless velocity parallel to the wall, u^+ and the dimensionless normal distance away from the wall, y^+ [112]. y^+ is a non-dimensional measurement of distance from the wall, see Figure 4.8. It is used to describe the height of the first grid element next to a wall. Experimental observation has confirmed that flows of all scales tend to demonstrate very similar patterns as it approaches the wall. So y^+ is used to identify where in the boundary layer profile the first calculation point resides. For the y^+ in the range of $y^+ \sim 1$, there is no need for any wall functions, as the flow is solved all the way to the wall. For the coarser mesh with the y^+ in the range of 30-500, the wall function has to be utilised in order to capture the near wall velocity profile [113].

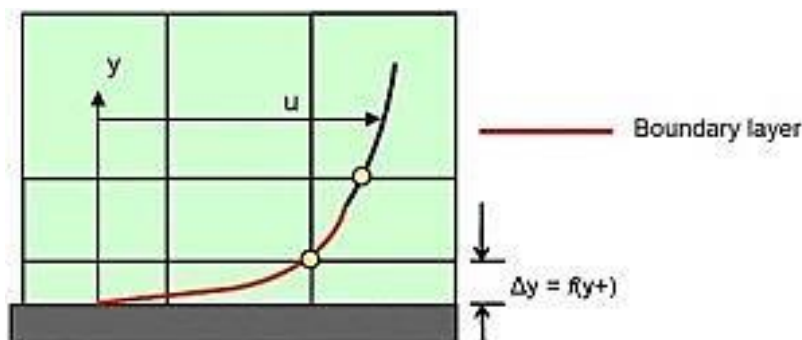


Figure 4.8 y^+ definition [113]

Looking at the Figure above, the y^+ value should not fall outside the boundary layer region, as the wall function used by the turbulence model may incorrectly calculate the flow properties at this first calculation point, which will introduce errors into the pressure drop and velocity results. In addition to the concern about having a mesh with y^+ values that are too large, if the y^+ value is too low then the first calculation point will be placed in the viscous sub-layer, see Figure 4.9. Flow region and the Wall Functions will also be outside their range validity [113].

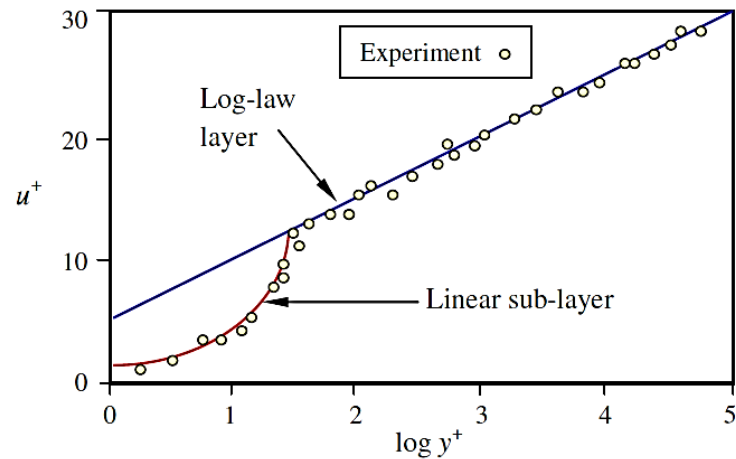


Figure 4.9 Dimensionless velocity distribution for the inner region of a boundary layer [114]

In this region $y^+ < 5$ [114] and the following relation holds:

$$U^+ = y^+ \quad (4.6)$$

Further away from the wall the log-law layer exists for which, $30 < y^+ < 500$ [114]. The main benefit of this wall function approach lies in the significant reduction in mesh resolution and thus reduction in simulation time. However, there will also be disadvantages if reduction of the y^+ value continues to below 30. This can result in unbounded errors in wall shear stress and wall heat transfer [115]. Despite the drawbacks of wall functions, they are very widely used for three-dimensional turbulent flows because of the benefit of minimising the cell count in the grid. Even so, the grid structure should still be sensibly constructed to make this approach valid. This ensures that near-wall turbulence is adequately treated without the prohibitively large mesh that would be necessary to solve the turbulent structures all the way to the wall [115].

4.4.3. Turbulence Intensity

The turbulence intensity is defined as the root-mean-square of the turbulent velocity fluctuations (u') divided by the Reynolds averaged mean velocity (U) and it is often referred as turbulence level [66].

$$I = \frac{u'}{U} \quad (4.8)$$

u' can be computed as when the turbulent energy (k) is known:

$$u' = \sqrt{\frac{1}{3} (u_x'^2 + u_y'^2 + u_z'^2)} = \sqrt{\frac{2}{3} k} \quad (4.9)$$

U can also be computed as:

$$U = \sqrt{U_x^2 + U_y^2 + U_z^2} \quad (4.10)$$

Where, U_x^2 , U_y^2 and U_z^2 are the mean velocity components.

It is often necessary to estimate the turbulence intensity on the inlet when setting the boundary conditions for the CFD simulation. The estimation is normally based on some form of measurements or previous experience. Some examples for common estimation of the incoming turbulence intensity are mentioned below [66]:

- **High-turbulence case:** Typically the turbulence intensity is between 5% to 20% for high speed flow inside complex geometries like flow inside rotating machinery.
- **Medium-turbulence case:** The turbulence intensity is typically between 1% to 5% for the flow in not-so-complex devices like large pipes and ventilation flows.
- **Low-turbulence case:** Flow originating from a fluid that stand still, like external flow across cars and aircraft. Quality wind tunnels can reach really low turbulence level. Typically the turbulence intensity is low and below 1%.

4.4.4. Turbulence Length Scale

The turbulence length scale (l) is a physical quantity describing the size of the large energy-containing eddies in a turbulent flow. It is often used to estimate the turbulence properties on the inlets of a CFD simulation. It is easy to guess a reasonable value of the turbulence length scale since it is a quantity which is related to the physical size of the problem. The turbulent length scale, in the $k - \epsilon$ model can be computed as below [67]:

$$l = C_{\mu}^{\frac{3}{2}} \frac{k^{\frac{3}{2}}}{\epsilon} \quad (4.12)$$

Some CFD codes such as Fluent, use a different length scale definition based on the mixing-length as follow:

$$l = C_{\mu}^{\frac{3}{4}} \frac{k^{\frac{3}{2}}}{\epsilon} \quad (4.13)$$

Where C_{μ} is the model constant which is 0.09 for the standard version of the $k - \epsilon$ model. The turbulence length scale used in these codes is about two times larger than the length scale variable used in other codes. Turbulence length scale is normally set to a certain percentage of a typical dimension of the problem. For example at the inlet of a turbine stage a typical turbulence length scale is about 5% of the channel height [91]. For some CFD codes, such as Fluent, 0.038 should be replaced by 0.07. For external flows such as this work (Wind Tunnel simulation) it is customary to set the turbulence intensity to something low such as 1% [107]. This is because the fluid is assumed to be standing still before the car pushes a hole into it, meaning this parameter is a measure in some way of the initial turbulence energy in the system. The turbulence length scale for our case in fluent is set to 7% of the hydraulic (characteristic) diameter. This diameter is the scale from which the resulting turbulence is generated (in our case the length of the car in the direction of motion) [67].

4.5. Turbulence Modelling

Turbulent flows are characterised by a wide range of spatial and temporal scales. Only simple geometries at relatively low Reynolds numbers can be solved without

turbulence flow modelling. The motion of a non-turbulent, Newtonian fluid is governed by the Navier-Stokes equation. The Navier–Stokes equations as mentioned earlier, describe the motion of fluid and they are formed by applying Newton's second law to fluid motion, together with the diffusing viscous term and a pressure term. Turbulence is characterised by a range of turbulence length scales. Clearly the number of length scales involved in the vehicle aerodynamics presents a significant challenges for CFD simulations. The necessity to solve such a problems has resulted in developments of turbulence modelling, which seeks to capture features of fluid flows in an accurate and efficient manner. Therefore, for engineering purpose, and/or in case of complex flows, one has to separate the scales so only specific ones are solved for certain applications. With this idea, some scales are going to be resolved (usually the larger scales) and some others will be modelled. This idea of modelling is called turbulence modelling. To do this, several approaches are available as below. One approach is chosen depending on the cost, reliability and accuracy. The different types of CFD modelling of turbulence are [116]:

4.5.1. Direct Numerical Simulation (DNS)

In this approach the N-S equations are solved without any turbulent modelling. It combines mean flow and turbulent velocity fluctuations and solve the time-dependent Navier-Stokes equations. The principle of Direct Numerical Simulation (DNS) is to directly solve all the turbulent length and time scales. In order to make this possible, the grids must be fine enough to resolve the smallest eddies which places huge demands on the computing resources [43]. In addition, temporal discretization should be sufficient to capture the fastest events which can occur with a frequency of on the order of 10 kHz, and should require time steps of 100 μs [44]. Since DNS is expensive, it is limited to flows with low Reynolds number; the flow around a vehicle will be out of reach for many decades [46]. In fact directly resolving all of the turbulent scales is of little use when it is limited to simulations within tiny domains for a very small timeframes [46]. Therefore obtaining such a wealth of detailed information is unnecessary and unfeasible in simulating vehicle aerodynamic flows. It is sufficiently difficult to resolve Kolmogorov micro-scale (smallest dissipative scales in turbulent flow) at which the energy dissipation takes place and it is a time consuming approach [108]. Equation (4.15) defines the Kolmogorov length scale.

$$\eta = \left(\frac{\nu^3}{\epsilon}\right)^{1/4} \quad (4.15)$$

Where ϵ is the average rate of energy dissipation per unit mass and ν is the kinetic viscosity. Typical values of the Kolmogorov micro-scale range from 0.1 to 10 millimetres [117]. This method has proved to be very costly and therefore is not widely used. [118]

4.5.2. Large Eddy Simulation (LES)

LES tracks the larger eddies with most energy and fluxes (important eddies) of the flow. This method contains spatial filtering that passes larger eddies and rejects the smaller eddies with little energy and fluxes and models the effects of unsolved flow (small eddies) by a sub-grid scale model. Demands of this model on computer resources are large as unsteady flow equation needs solving. It is more suitable for complex geometry [118]. LES is a compromise between the accuracy of the DNS and the efficiency demanded by industry. LES only computes the large scale turbulence fluctuations in space and time and turbulence eddies below a certain size, are filtered out and modelled using semi-empirical laws in the form of a sub-grid scale (SGS) model [91, 108]. For this model the grid only needs to be fine enough to model the large eddies, and the sub-grid scale accounts for anything smaller, but still time dependent nature of the LES makes it expensive for high Reynolds number flows and it would be far from affordable for the aerodynamic flows for many decades [77, 79, 80].

4.5.3. Detached Eddy Simulations (DES)

Spalart *et al.*, (1997) proposed a hybrid method that combines the respective strength of LES and RANS which is known as Detached Eddy Simulations (DES). DES is designed for external flows and the concept is to entrust the entire boundary layer to a steady RANS model, which it with attached eddies, whilst allowing LES to resolve separated regions containing detached eddies [79]. It offers advantages in terms of simplicity because it only requires small alteration to the Spalart Allmaras (S-A) one-equation model [119].

4.5.4. Reynolds-Averaged Navier-Stokes (RANS) Equation

The focus will be more on RANS equations, since they will be used in this work and they have been very popular and widely used in similar works. RANS equations focuses on mean flow and the effect of the turbulence on the mean flow properties and its objective is to compute the Reynolds Stresses. The Reynolds Stress is the

stress tensor in a fluid due to the turbulent fluctuations in the fluid momentum. The stress is obtained from an average over these fluctuations. The Navier-Stokes equations are averaged, they are based on mean velocity, pressure and stress etc. They have an extra term (time average) due to interaction between various turbulent fluctuations. RANS is based on the assumption that there is an analogy between the action of the viscous stress and Reynolds stress on the mean flow. A characteristic feature of a turbulent flow is a small - scale, high - frequency random fluctuation superimposed on a main flow which has an identifiable direction. Normally, the magnitude of the fluctuation is in the range of 5 -10% of the magnitude of the main flow [91]. In order to be able to take a time-average, the momentary value is decomposed into the parts mean value and fluctuating value. The momentary velocity component is u , the time-averaged value is named \bar{u} and the fluctuating velocity has the letter u' . With help of this definition the decomposition can mathematically be written as [107]:

$$u = \bar{u} + u', \quad v = \bar{V} + V', \quad w = \bar{w} + w', \quad p = \bar{p} + p' \quad (4.16)$$

In Figure 4.10 the horizontal line in brown colour indicates the time independence of a laminar flow. Also, in the same Figure, the fluctuating flow is earmarked with a blue horizontal line which represents the time-average of the fluctuating velocities. The averaging process is defined by [107]:

$$\bar{u} = \frac{1}{t} \int_0^t u(\tau) d\tau \quad (4.17)$$

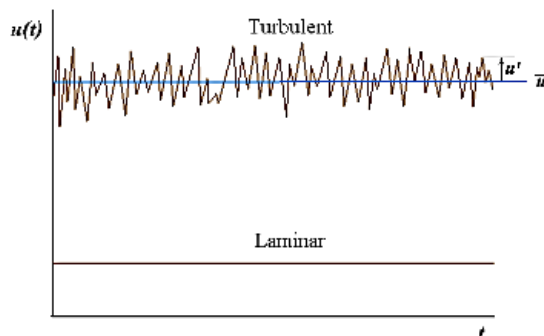


Figure 4.10 Instantaneous velocity measurements in laminar and turbulent flow [107]

By going back to the x-component of the momentum equation in conservative form [91]:

$$\rho \left(\frac{\partial u}{\partial t} + \frac{\partial(u^2)}{\partial x} + \frac{\partial(uv)}{\partial y} + \frac{\partial(uw)}{\partial z} \right) = -\frac{\partial P}{\partial x} + \mu \left(\frac{\partial^2 u}{\partial x^2} + \frac{\partial^2 u}{\partial y^2} + \frac{\partial^2 u}{\partial z^2} \right) \quad (4.18)$$

Note that a time-dependent term $\frac{\partial u}{\partial t}$ has been appended to this equation to take account of the fact that a turbulent flow is inherently unsteady. Substituting in variables defined in term of mean and fluctuating components:

$$\rho \left(\frac{\partial(u+u')}{\partial t} + \frac{\partial(u+u')^2}{\partial x} + \frac{\partial(u+u')(v+v')}{\partial y} + \frac{\partial(u+u')(w+w')}{\partial z} \right) = -\frac{\partial(P+p')}{\partial x} + \mu \left(\frac{\partial^2(u+u')}{\partial x^2} + \frac{\partial^2(u+u')}{\partial y^2} + \frac{\partial^2(u+u')}{\partial z^2} \right) \quad (4.19)$$

Expanding the equations:

$$\rho \left(\frac{\partial \bar{u}}{\partial t} + \frac{\partial(\bar{u}^2)}{\partial x} + \frac{\partial(\bar{u}\bar{v})}{\partial y} + \frac{\partial(\bar{u}\bar{w})}{\partial z} + \frac{\partial(u')}{\partial t} + \frac{\partial(2\bar{u}u')}{\partial x} + \frac{\partial(u')^2}{\partial x} + \frac{\partial(\bar{u}v')}{\partial y} + \frac{\partial(\bar{v}u')}{\partial y} + \frac{\partial(u'v')^2}{\partial y} + \frac{\partial(\bar{u}w')}{\partial z} + \frac{\partial(\bar{w}u')}{\partial z} + \frac{\partial(u'w')^2}{\partial z} \right) = -\frac{\partial \bar{P}}{\partial x} - \frac{\partial p'}{\partial x} + \mu \left(\frac{\partial^2 \bar{u}}{\partial x^2} + \frac{\partial^2 \bar{u}}{\partial y^2} + \frac{\partial^2 \bar{u}}{\partial z^2} + \frac{\partial^2 u'}{\partial x^2} + \frac{\partial^2 u'}{\partial y^2} + \frac{\partial^2 u'}{\partial z^2} \right) \quad (4.20)$$

Figure 4.11 shows the graphical representation of the terms that appear on the right hand side of the equation (3.21).

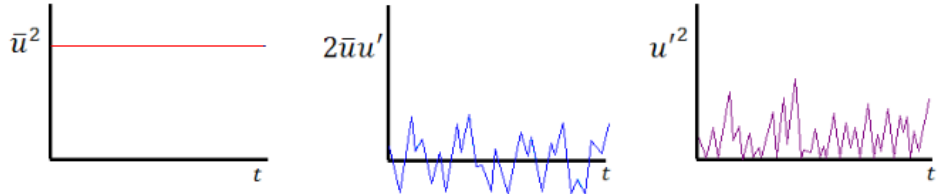


Figure 4.11 Graphical representation of the terms that appear on the right hand side of the equation [91]

Following rules are applied when above equation is time-averaged:

$$\begin{aligned}
\overline{\bar{u}} &= \bar{u} & \overline{\bar{u} + u'} &= \bar{u} + \bar{u}' = \bar{u} & \overline{\bar{u} \cdot u'} &= \bar{u} \cdot \bar{u}' = 0 \\
\frac{\partial \bar{u}}{\partial x} &= \frac{\partial \bar{u}}{\partial x} & \overline{u'^2} &= \overline{\bar{u} \cdot \bar{u}} = \bar{u} \cdot \bar{u} = \bar{u}^2 & \overline{u'v'} &< 0
\end{aligned} \tag{4.21}$$

Many of the terms cancel out to give [91]:

$$\rho \left(\frac{\partial \bar{u}}{\partial t} + \bar{u} \frac{\partial \bar{u}}{\partial x} + \bar{v} \frac{\partial \bar{u}}{\partial y} + \bar{w} \frac{\partial \bar{u}}{\partial z} \right) = -\frac{\partial \bar{P}}{\partial x} + \mu \left(\frac{\partial^2 \bar{u}}{\partial x^2} + \frac{\partial^2 \bar{u}}{\partial y^2} + \frac{\partial^2 \bar{u}}{\partial z^2} \right) - \rho \left[\frac{\partial}{\partial x} (\overline{u'^2}) + \frac{\partial}{\partial y} (\overline{u'v'}) + \frac{\partial}{\partial z} (\overline{u'w'}) \right] \tag{4.22}$$

This is RANS equation in x-direction. The additional terms that arise in this equation due to turbulent mixing are called the apparent or Reynolds stresses [91].

$$\begin{aligned}
\tau'_{xy} = \tau'_{yx} &= -\rho \overline{u'v'} & \sigma'_{xx} &= -\rho \overline{u'^2} \\
\tau'_{yz} = \tau'_{zy} &= -\rho \overline{v'w'} & \sigma'_{yy} &= -\rho \overline{v'^2} \\
\tau'_{zx} = \tau'_{xz} &= -\rho \overline{u'w'} & \sigma'_{zz} &= -\rho \overline{w'^2}
\end{aligned} \tag{4.23}$$

The RANS approach is the most used method for simulating turbulence, which is inherently steady state and only the largest turbulent scales are computed [108]. They usually employ wall functions to represent near-wall turbulence and can be split into the following types of extra term [91]:

- k-ε model [113] (two transport equations)
- k – ω model [120] (two transport equations)
- Mixing length model (zero transport equations)
- Reynolds stress Model (seven transport equations)
- Algebraic stress model
- Spalart-Allmaras [41] Model (one transport equation)

K-ε model and Spalart-Allmaras models are widely used and will be used in this work and discussed in details later. Although the RANS modelling takes away vital information in a given flow field, the averaging process considerably simplifies the problem and time-averaging is not required. If time dependent solutions are required, an unsteady formulation of RANS, URANS, can be adopted which allows

phenomena such as vortex shedding to be simulated. URANS solutions are much smoother than the true turbulent field and suitable for external aerodynamics [46]. Below is an example of the respective performance of different approaches to turbulence which are presented by Spalart (2000): Figure 4.12.

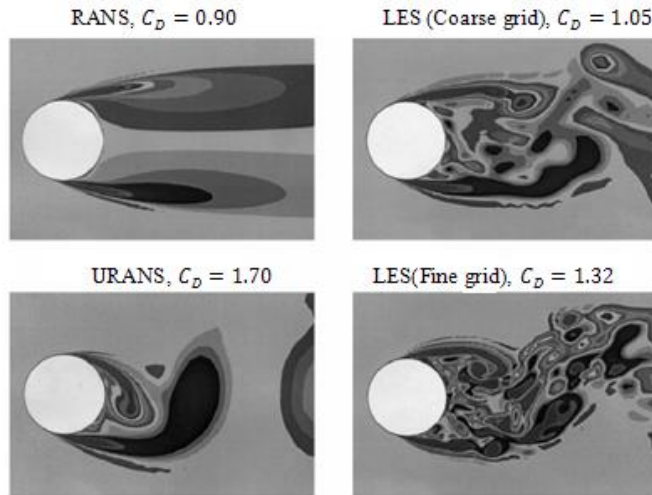


Figure 4.12 Comparison of computed flow fields around a cylinder for $Re = 50,000$ using various turbulence treatments. Experimental $C_D = 1.2$ [43]. Courtesy of Philippe Spalart, Boeing Commercial Airplanes.

4.5.5. Efficiency vs. Accuracy

Since there is a variety of methods to model the flow turbulence, it is difficult to choose one amongst them. DNS and LES clearly present the most accurate for solving bluff-body flows but since they require immense computational power, they are impractical, see table 4.1.

Category	Unsteady	Empiricism	Grid Nodes	Ready
RANS	No	Strong	10^7	1990
URANS	Yes	Strong	10^7	1995
DES	Yes	Strong	10^8	2000
LES	Yes	Weak	$10^{11.5}$	2045
DNS	Yes	None	10^{16}	2080

Table 4.1 Summary of turbulence strategies for the 3D flow past an aeroplane or vehicle [43]

DES is also impractical for the present study, since it requires many grid elements. In terms of grid required to simulate the airflow around a van or a car, both RANS

and URANS are suitable. Since the focus of this investigation is to measure the drag force, RANS turbulence modelling is the only viable method.

4.5.6. The $k - \omega$ Model

One of the most commonly used turbulence models is the $k - \omega$ model. It is two equation model which means it has two extra transport equation ((4.26) and (4.27)) to represent turbulence properties of the flow the same as $k - \omega$ model. The first transported variable is k which is turbulent kinetic energy and determines the energy in turbulence. The second variable is ω which is the turbulence frequency. Original form of $k - \omega$ (KO) was proposed by Kolmogorov [120] and later developed by Wilcox (1994). Eddy viscosity and ω are given as below:

$$\omega = \frac{\varepsilon}{K} \quad (4.24)$$

$$\mu_t = \rho \frac{k}{\omega} \quad (4.25)$$

The transport equations for k and ω in $k - \omega$ model, are as below [91]:

$$\frac{\partial(\rho k)}{\partial t} + \text{div}(\rho k U) = \text{div} \left[\left(\mu + \frac{\mu_t}{\sigma_k} \right) \text{grad}(k) \right] + \gamma_1 \left(2\rho S_{ij} \cdot S_{ij} - \frac{2}{3} \rho k \frac{\partial U_i}{\partial x_i} \delta_{ij} \right) - \beta^* \rho \omega \quad (4.26)$$

$$\frac{\partial(\rho \omega)}{\partial t} + \text{div}(\rho \omega U) = \text{div} \left[\left(\mu + \frac{\mu_t}{\sigma_\omega} \right) \text{grad}(\omega) \right] + \gamma_1 \left(2\rho S_{ij} \cdot S_{ij} - \frac{2}{3} \rho \omega \frac{\partial U_i}{\partial x_i} \delta_{ij} \right) - \beta_1 \rho \omega^2 \quad (4.27)$$

Or in words:

Rate of change of k or ω + Transport of k or ω by convection = Transport of k or ω by turbulent diffusion + Rate of production of k or ω - Rate of dissipation of k or ω

Following are the constant values in the equation [91]:

$$\sigma_k = 2.00; \sigma_\omega = 2.00; \gamma_1 = 0.553; \beta_1 = 0.075; \beta^* = 0.09$$

Advantages and disadvantages of $k - \omega$ models :

$k - \omega$ model is more accurate for near wall treatment. It performs very well for wall-bounded and low Reynolds number flows. It accounts for transitional, free shear, and compressible flows and performs well under adverse pressure gradient [114]. Its disadvantages are that it normally predicts separation excessively and requires mesh resolution near the wall [84].

4.5.7. The Spalart-Allmaras Model

The Spalart-Allmaras model [41] only contains one transport equation for a kinematic eddy viscosity parameter ($\tilde{\nu}$). It is very economical in terms of computations of boundary layer for external aerodynamics; the transport equation for $\tilde{\nu}$ is as follows [91]:

$$\frac{\partial(\rho\tilde{\nu})}{\partial t} + \text{div}(\rho\tilde{\nu}U) = \frac{1}{\sigma_v} \text{div} \left[(\mu\rho\tilde{\nu}) \text{grad}(\tilde{\nu}) + C_{b2}\rho \frac{\partial\tilde{\nu}}{\partial\partial_k} \frac{\partial\tilde{\nu}}{\partial\partial_k} \right] + C_{b1}\rho\tilde{\nu}\tilde{\Omega} - C_{w1}\rho \left(\frac{\tilde{\nu}}{ky} \right)^2 f_w \quad (4.28)$$

And in words:

Rate of change of viscosity parameter $\tilde{\nu}$ + Transport of $\tilde{\nu}$ by convection = Transport of $\tilde{\nu}$ by turbulent diffusion + Rate of production of $\tilde{\nu}$ - Rate of dissipation of $\tilde{\nu}$

Where $\tilde{\Omega}$ is the local mean vorticity as follows:

$$\tilde{\Omega} = \Omega + \frac{\tilde{\nu}}{(ky)^2} f_{v^2} \quad (4.29)$$

$$\Omega = \sqrt{2\Omega_{ij}\Omega_{ij}} \quad (4.30)$$

$$\Omega_{ij} = \frac{1}{2} \left(\frac{\partial U_i}{\partial x_j} - \frac{\partial U_j}{\partial x_i} \right) \quad (4.31)$$

The functions $f_{v^2} = f_{v^2}(\tilde{\nu}/\nu)$ and $f_w = f_w \left(\tilde{\nu}/\tilde{\Omega}K^2y^2 \right)$ are wall damping functions,

Model constants have been driven by experiments and are given by [91]:

$$\begin{aligned} \sigma_v &= \frac{2}{3}; k = 0.4187; C_{b1} = 0.1355; C_{b2} = 0.0.622; \text{and } C_{w1} \\ &= C_{b1} + K^2 \frac{1 + C_{b2}}{\sigma_v} \end{aligned}$$

The Spalart-Allmaras model has proven to give good performance in boundary layers with adverse pressure gradient which are important for predicting stalled flows. As it is suitable for airfoil applications, therefore it is very attractive for turbo-machinery community. The model is unsuitable for complex geometry since it is difficult to predict the length scale in complex geometries and also it is not suitable for rapidly changing flows as it lacks sensitivity to transport processes [41, 91].

4.5.8. The Standard $k - \varepsilon$ Model

One of the most common turbulence models is $k - \varepsilon$ two transport equation which means, it includes two extra transport equations to present the turbulent properties of the flow. The first variable which is transported is k (kinetic energy), and the second one is ε (turbulent dissipation). k determines the energy in the turbulence and ε determines the scale of the turbulence [80, 113]. $k - \varepsilon$ model is the most widely used and validated turbulence model. It has been successful in calculating a wide variety of thin shear layer and recirculating flows. It has following advantages and disadvantages:

Advantages [44, 91]:

- Simplest turbulence model
- Excellent performance for many industrially relevant flows
- The most widely validated turbulence model

Disadvantages:

- Poor performance in some cases (some unconfined flows, large extra strains such as curved boundary layers, rotating flows)

$k - \varepsilon$ model is a semi-empirical model. The model transport equation for k is derived from the exact equation but the transport equation for ε was obtained using physical reasoning. In this model it is assumed that the effects of molecular viscosity are negligible and the flow is fully turbulent [81]. $k - \varepsilon$ model focuses on the mechanism that effects the turbulence kinetic energy k . It is a sum of the mean kinetic energy and the turbulent kinetic energy [91]:

Mean kinetic energy:

$$K = \frac{1}{2}(U^2 + V^2 + W^2) \quad (4.30)$$

Turbulent kinetic energy:

$$k = \frac{1}{2}(\overline{u'^2} + \overline{v'^2} + \overline{w'^2}) \quad (4.31)$$

Therefore:

$$k(t) = K + k \quad (4.32)$$

The $k - \varepsilon$ model uses the following transport equations for k and ε [91]:

$$\frac{\partial(\rho k)}{\partial t} + \text{div}(\rho k U) = \text{div} \left[\frac{\mu_t}{\sigma_k} \text{grad } k \right] + 2\mu_t S_{ij} \cdot S_{ij} - \rho \varepsilon \quad (4.33)$$

$$\frac{\partial(\rho \varepsilon)}{\partial t} + \text{div}(\rho \varepsilon U) = \text{div} \left[\frac{\mu_t}{\sigma_\varepsilon} \text{grad } \varepsilon \right] + C_{1\varepsilon} \frac{\varepsilon}{k} 2\mu_t S_{ij} \cdot S_{ij} - C_{2\varepsilon} \rho \frac{\varepsilon^2}{k} \quad (4.34)$$

In words the equations are:

Rate of change of k or ε + Transport of k or ε by convection = Transport of k or ε by diffusion + Rate of production of k or ε – Rate of destruction of k or ε

k and ε are used to define the velocity scale (ϑ) and length scale (l) [91]:

$$\vartheta = k^{3/2} \quad (4.35)$$

$$l = \frac{k^{3/2}}{\varepsilon} \quad (4.36)$$

The turbulent viscosity, (μ_t), is computed by combining k and ε as below:

$$\mu_t = C_\rho \vartheta l = \rho C_\mu \frac{k^2}{\varepsilon} \quad (4.37)$$

The equation contains following constants [91]. They have been determined from experiments and they have been found to work well for a wide range of wall-bounded and free shear flow.

$$C_\mu = 0.09 \quad \sigma_k = 1.00 \quad \sigma_\varepsilon = 1.30 \quad C_{1\varepsilon} = 1.44 \quad C_{2\varepsilon} = 1.92$$

4.5.9. Realisable $k - \varepsilon$ Model

The Realisable $k - \varepsilon$ model is a recent development and is different from standard $k - \varepsilon$ in two ways [114]:

- It contains a new formulation for the turbulent viscosity
- A new transport equation for the dissipation rate (ε) has been derived from an exact equation for the transport of the mean-square vortices fluctuation.

$k - \varepsilon$ model modified by Shih *et al.*, (1995) to account for higher Reynolds number flows, and was named realisable $k - \varepsilon$. The term realisable implies that turbulence quantities such as k and ε must satisfy the condition that they are always greater than zero [91]. The model (realisable $k - \varepsilon$) satisfies certain mathematical constraints on the Reynolds stresses, consistent with the physics of turbulent flows. The viscosity, the same as other $k - \varepsilon$ models, is computed as below, but the difference is that C_μ is no longer constant and computed using the formula below:

$$\mu_t = \rho C_\mu \frac{k^2}{\varepsilon} \quad (4.38)$$

$$C_\mu = C_\mu \left(\frac{SK}{\varepsilon} \right) \quad (4.39)$$

Where:

$$S = \sqrt{2S_{ij}S_{ij}} \quad (4.40)$$

There is also a modification to the ε equation [91]. This model has been validated for a wide range of flows (rotating shear flows, free flow including jets and mixing

layer and separated flows) [82]. This makes the Realisable $k - \varepsilon$ model more suitable than the standard $k - \varepsilon$ model for bluff body vehicle aerodynamics [9].

4.5.10. The RNG $k - \varepsilon$ Model

In standard $k - \varepsilon$ model the eddy viscosity is determined from a single turbulence length scale, therefore the turbulent diffusion occurs only at the specific scale but in reality all scales of motion will contribute to the turbulent diffusion. RNG $k - \varepsilon$ model was developed to account for the effects of smaller scales of motion. It is a modified form of the $k - \varepsilon$ equation which attempts to account for the different scales of motion through changes to the production term [80].

Transport equations for RNG $k - \varepsilon$ model are as below:

$$\frac{\partial(\rho k)}{\partial t} + \text{div}(\rho k U) = \text{div} \left[\frac{\mu_t}{\sigma_k} \text{grad } k \right] + 2\mu_t S_{ij} \cdot S_{ij} - \rho \varepsilon \quad (4.41)$$

$$\frac{\partial(\rho \varepsilon)}{\partial t} + \text{div}(\rho \varepsilon U) = \text{div} \left[\alpha_k \mu_{eff} \text{grad } \varepsilon \right] + C_{1\varepsilon}^* \frac{\varepsilon}{k} \tau_{ij} \cdot S_{ij} - C_{2\varepsilon} \rho \frac{\varepsilon^2}{k} \quad (4.42)$$

Where

$$\tau_{ij} = \overline{\rho u_i' u_j'} = 2\mu_t S_{ij} - \frac{2}{3} \rho k \delta_{ij} \quad (4.43)$$

$$\mu_{eff} = \mu + \mu_t \quad , \quad \mu_t = \rho C_\mu \frac{k^2}{\varepsilon} \quad (4.44)$$

$$C_\mu = 0.0845 \quad , \quad \alpha_k = \alpha_k = 1.39 \quad , \quad C_{1\varepsilon} = 1.42 \quad , \quad C_{2\varepsilon} = 1.68$$

And

$$C_{1\varepsilon}^* = C_{1\varepsilon} - \frac{\eta(1 - \eta/\eta_0)}{1 + \beta\eta^3} \quad , \quad \eta = \frac{k}{\varepsilon} \sqrt{2S_{ij} \cdot S_{ij}} \quad , \quad \eta_0 = 4.377 \quad , \quad \beta = 0.012$$

4.6. Numerical Noise and Convergence Tolerance

Numerical noise is an inevitable by-product of Computational Fluid Dynamics (CFD) simulations which can lead to challenges in finding optimum designs [102].

It is, in fact, the distance from the simulation results to the actual experimental value. The noisy simulation results are not in favor of optimisation and it is intended to reduce the noise as much as possible. The noisy responses create a unrealistic response surfaces and the corresponding optimisation results would not be very accurate.

Convergence is arriving at a solution that is close to the exact solution within some pre-specified error tolerance or other convergence criterion. Convergence tolerance is the specified error between the convergence and the exact result which is acceptable and is set initially [121]. At convergence, the following should be satisfied:

- All discrete conservation equations (momentum, energy, etc.) are obeyed in all cells to a specified tolerance or the solution no longer changes with subsequent iterations.
- Overall mass, momentum, energy, and scalar balances are achieved.
- Generally, a decrease in residuals by three orders of magnitude indicates at least qualitative convergence. At this point, the major flow features should be established.
- Ensure that overall mass/heat/species conservation is satisfied.

If solution monitors indicate that the solution is converged, but the solution is still changing or has a large mass/heat imbalance, this clearly indicates the solution is not yet converged. In this case, the iterations need to be continued until the solution converges. The convergence can be accelerated and the numerical errors can be contained by implementing the following [121]:

- Use higher-order discretization schemes (second-order upwind)
- Refine the mesh

For a Steady State simulation we need to ensure that the solution satisfies the following three conditions [122]:

- Residual RMS Error values have reduced to an acceptable value (typically 10^{-4} or 10^{-5})

- Monitor points for our values of interest have reached a steady solution
- The domain has imbalances of less than 1%.

The values of interests such as pressure and velocity needs to converge to a steady value and running the simulation for an additional 50 iterations should not produce a different result. Ensuring that these values have reached a steady solution means that the solution is a single repeatable value [122].

4.7. Error and Uncertainty in CFD

Numerical errors are unavoidable within the solution of CFD calculations since they involve discretizing a set of continuous governing equations. Their iterative nature and other factors including the effects of numerical diffusion also add to the error of the solution. The following definitions are widely accepted in the CFD modelling for the error and uncertainty [1, 12, 91]:

- **Error:** recognisable deficiency in a simulation which is not caused by lack of knowledge. (Boundary condition, fluid property)
- **Uncertainty:** potential deficiency which is caused by lack of knowledge

Errors can be grouped into three main categories [91]:

- 1) Coding errors
- 2) User errors
- 3) Numerical errors

Most of the problems are caused due to the coding and user errors. Coding error can catch out even the most sophisticated organisations. Since the modern CFD is complex, it is unlikely that these coding and user errors can be totally eliminated but they can be minimized by training and experience. Round-off errors and iterative convergence error are two examples of numerical errors. Round-off error is caused as a result of the computational representation of real numbers. Convergence can be defined as a point during the CFD simulation when successive iterations yield no tangible differences/improvement in the solution. Convergence error occurs when

the solution is analysed before through convergence is observed, which can be very misleading. In commercial CFD packages such as Fluent, convergence is established when residuals reduce by a pre-determined levels, typically, three order of magnitude [46]. However, greater precision may be needed in other flows.

4.8. Verification and Validation

Once the error and uncertainty have been considered in the CFD simulation, it becomes necessary to develop a method to quantify the level of confidence in its results. The most fundamental methods are verification and validation which relate to the error and uncertainty resulting from the numerical simulations [1, 91]:

- Verification: this is the process at which it ensures that the mathematical representation of a physical system is solved accurately. (or as Roache (1998) [2] calls it: solving the equations right).
- Validations: this is concerned with whether the correct problem is being solved and the model is the accurate representation of the real world from the perspective of the intended uses of the model (or as Roache (1998) [2] calls it: solving the right equations.

Since each problem is unique, verification is a difficult process, and discretization of the governing equations will inevitably be in error. The process of verification involves quantification of the error. Computer coding errors and user errors have already been discussed, therefore estimation of the following verification errors will be discussed [91]:

- Round off error
- Iterative convergence error
- Discretisation error

By comparing the CFD results obtained using different level of machine accuracy, round off error can be assessed. Iterative convergence error can also be assessed by investigating the effects of systematic variation of the truncation criteria for all the residuals on the target quantity of interest. Discretisation error is quantified by systematic refinement of the space and time meshes. Two or three successive levels

of mesh refinement of the whole flow field can demonstrate the reduction of the discretisation error [91]. Two main source of validation uncertainties are as below [91]:

- Input uncertainty
- Physical modelling uncertainty

Sensitivity or uncertainty analysis can be used to estimate the input uncertainty. This involves the multiple test runs of the CFD model with different values of input data. By observing the variation of target quantity of interest, the lower and upper bounds for the expected range can be produced, they are then useful for input uncertainty measurement. Physical modelling uncertainty requires comparison of CFD results with high quality experimental results [12]. Therefore the comparison between the CFD model output and experimental data is the ultimate test of validation. However the way in which such a comparison should be made is not clear and still subject of discussion. The most common way of reporting the outcome of the validation exercise is to draw a graph of a target quantity such as distance or force on the y-axis and flow parameter such as velocity or temperature on the x-axis. If the difference between the CFD result and the experimental data is small, CFD model is considered to be validated. If suitable experimental results for a validation analysis are not available, a data set for a similar problem can be used. If the problem chosen for the validation is sufficiently close to the actual problem to be studied, the same CFD approach can be applied [91].

5. Design Optimisation

This chapter is concerned with optimising vehicles using CFD-based optimisation methods and it presents an overview of the relevant technical methods. This chapter explains the process of optimisation which is mainly used for CFD optimisation. It will also explain the most popular methods used in different parts of the process of optimisation. The main focus will be on the techniques that will be used in this study which is the CFD optimisation of the Emergency Response Vehicles.

5.1. Optimisation process

Optimisation is defined as the design and operation of a system or process to make it as good as possible in some defined sense [80]. The philosophy is to find an improved design which may not be intuitive, based on the principle of the application under investigation. The maturity of CFD is now such that coupling it with formal optimisation techniques offers potentially huge benefits. Although this idea is not novel and there is a great interest in coupling CFD with optimisation [80]. Following is a review of optimisation and the focus is on the methods which are employed later in the study. Optimisation can be done directly by modification of the design variables by using the information from the old design until it reaches the optimum (MAM) and it can also be done virtually by optimising the response surface method which is called virtual optimisation. The method chosen here consists mainly of three parts:

- Creation of design variables (DoEs)
- Creation of response surface (meta-models)
- Optimisation on the response surfaces

5.2. Design of Experiments (DoEs)

Response surface modelling is a method for approximating a system's response using function values at certain points in the design variable space and it is often used to minimize the number of response evaluations and reduce the effects of numerical noise (refer to chapter 4.6). In order to build the response surface the response of the system is evaluated by running the simulation model at a series of parameter values defined by a DoEs in the range of variation of these parameters [123].

5.2.1. Design vector

Any engineering system is defined by set of variables and constants. All the quantities that are treated as variables in an engineering system are called design variables and the space that they are placed in is called design space. Each of these points in the design space is called design point which represents either a possible or impossible solution to the design problem.

$$\text{Design variables} \quad x_i, i = 1, 2, \dots, n \quad (5.1)$$

$$\text{Design vector} \quad X = \{x_1, x_2, \dots, x_n\}^T \quad (5.2)$$

A key component of developing an accurate Response Surface of a system's response to its input design variables is the use of an effective DoEs strategy for obtaining information from across the design space as efficiently as possible [123]. Clearly the quality and accuracy of the optimisation will depend on the number of points used and the way they are spread out in the design space. DoEs are sampling plans which determine the number and distribution of the points required, so it can extract the maximum amount of information from the fewest simulations possible [77]. It is a branch of applied statistics that deals with planning, conducting, analyzing and interpreting controlled tests to evaluate the factors that control the value of parameter or group of parameters [73]. Generally DOE or experimental design is the design of any information-gathering exercise where variation is present. These terms, in statistics, are normally used for controlled experiments. In DOE, the experimenter is usually interested in the effect of some process or treatment on some objects, which may be group of people, materials, etc. DOE economically maximizes the information in an experiment; one or more process variables are deliberately changed in order to observe the effect the changes have on one or more response variables. It is an efficient procedure for planning experiments so that valid objective conclusion can be yielded from the data obtained. DOE starts with determining the objectives of an experiment and selecting the design variables for the study. It is the laying out of a detailed experimental plan in advance of doing the experiment. DOE generally starts with the concept of choosing several discrete or continuous factors called design variables that can be controlled [74]. DOE studies are defined as a test or a series of tests in which input variables of a process or a system are intentionally changed so that the reasons for changes in the output response can be identified and observed. The factors such as thickness, shape design variables, and material properties can be changed to study the output responses of

the model. DOE studies can also provide information about interactions between these input factors and their effect on the output. The objective of a DOE study is to understand how changes to the design parameters of a model influence its performance. In such a study, a model is repeatedly run through a simulation for various combinations of design parameter settings. Effects and interactions of the design variables of the model can be studied.



Figure 5.1 Optimisation process [124]

The goal of a DOE study is not to find an optimal, single solution

but it is to develop an understanding of the behaviour of a system. The most important information obtained from a DOE study is the ability to predict trends, even with interacting design variables. The response surface is the next step on from the DoEs [75].

5.2.2. Sampling

There is a high number of sampling methods and one of the most popular methods is, Latin Hypercube Sampling (LHS), which is also used in this thesis; in the following three methods are explained briefly:

- Random Sampling
- Full Factorial Sampling
- Latin Hypercube Sampling

Random sampling and Full Factorial Sampling are discussed briefly below and the main focus will be on Latin Hypercube sampling which is the most popular method and will be used in this study.

5.2.3. Random Sampling

In random sampling, new sample points are generated without taking into account the previously generated sample points. There is no need to know beforehand how many sample points are needed.

5.2.4. Full Factorial Sampling

In Full Factorial Sampling, which is probably the most common and intuitive strategy and in its most simple form, there are k factors (i.e. design variables) and $L=2$ levels per factor. The samples are given by every possible combination of the factors values leading to a sample size of $N=2^k$. The idea of the 2^k full factorial design can easily be extended to the general case where there are more than two factors and each of them have more than two levels. If there are k factors x_1, \dots, x_k having L_1, L_2, \dots, L_k levels, then the sample size of the adjustable full factorial design is

$$N = \prod_{i=1}^k L_i \quad (5.3)$$

Full factorial designs make very efficient use of the data and enable the main and the interaction effects between factors to be identified clearly. The family of L_k designs, namely full factorial designs where the number of levels is the same for each factor, is particularly suitable for interpolation by polynomial response surfaces, since a 2^k design can be interpolated with a complete bilinear form, a 3^k design by a complete biquadratic form, a 4^k with a complete cubic and so on. The following Figure shows graphical representations of the 2^2 , 2^3 and 3^3 full factorial designs.

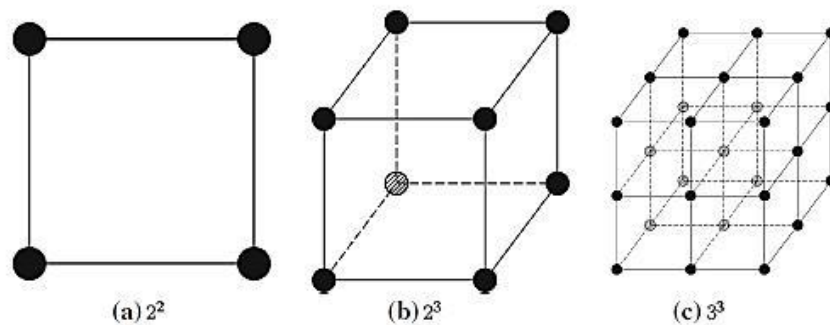


Figure 5.2 Simple Full Factorial Designs [123]

5.2.5. Latin Hypercube Sampling

In Latin Hypercube Sampling, which is a space filling method, the base is on the concept of levels and do not require discretization and the sample size is chosen by the experimenter independently from the number of parameters of the problems. It is needed to decide how many sample points to use and for each sample point remember in which row and column the sample point was taken. Latin Hypercube Sampling is a statistical method for generating a distribution of plausible collections of parameter values from a multidimensional distribution. The technique was first described by McKay in 1979 [120]. It was further elaborated by Ronald L. Iman, and others in 1981 [113]. Latin Hypercube Sampling is a form of stratified sampling that can be applied to multiple variables. This method is commonly used to reduce the number of runs for a Monte Carlo simulation (Monte Carlo methods are stochastic techniques [123]), meaning they are based on the use of random numbers and probability statistics to investigate problems to achieve an accurate random distribution [79]. The concept behind the Latin Hypercube Sampling is not very complex. Variables are sampled using an even sampling method, and then randomly combined sets of these variables are used for one calculation of the specified function. It ensures the Monte Carlo simulation is run over the entire length of the variable distributions, it would also take unlikely extremities into account [80]. In Latin Hypercube, the design space is subdivided into an orthogonal grid with N elements of the same length per parameter if the variables have uniform distributions. Within the multi-dimensional grid N sub-volumes are specified so that along each row and column of the grid only one sub-volume is chosen. In the following Figure the chosen sub-volumes are black and give a typical crosswords-like graphical representation of Latin Hypercube designs. Inside each sub-volume a sample is chosen randomly.

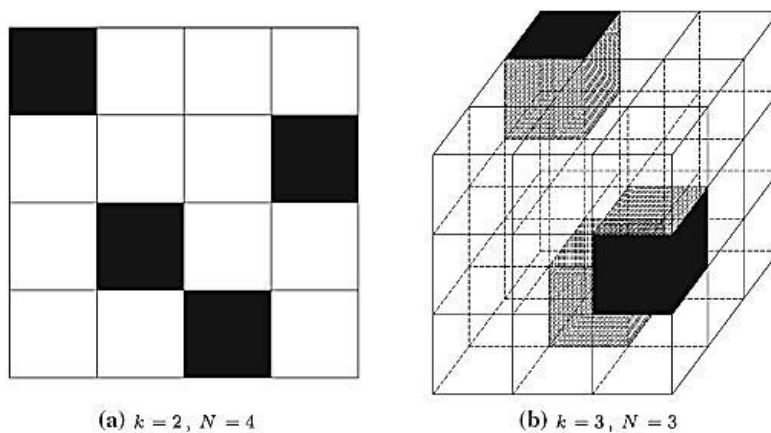


Figure 5.3 Latin Hypercube Sampling [123]

It is important to choose the sub-volumes in order to have no spurious correlations between the dimensions or to spread the samples all over the design space. For example, a set of samples along a design space diagonal would satisfy the requirements of a Latin Hypercube DoE but would leave most of the design space unexplored. There are several techniques used to reduce the correlations in Latin Hypercube designs. The following Figure shows an example of a correlation reduction between variable values in a Latin Hypercube DoE with $k=2$ factors and $N=10$:

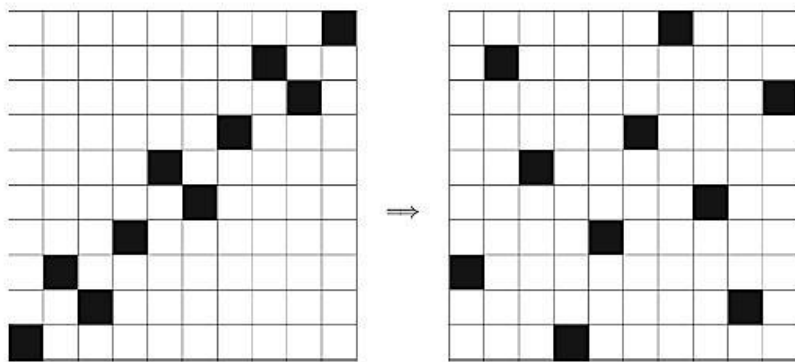


Figure 5.4 Correlation reduction in Latin Hypercube Sampling [123]

There are two different types of Latin Hypercube Sampling [96]:

- 1) Random Latin Hypercube (RLH)
- 2) Optimised Latin Hypercube (OLH)

The effect of two different methods for improving the uniformity of the space-filling properties of Latin Hypercube design is now compared briefly. The results below compare results from two space-filling Latin Hypercube DoE techniques for a sample size N and two design variables/factors, i.e. $k=2$. The first one, shown later on the left creates an optimised Latin Hypercube from a series of random Latin Hypercube using the Morris-Mitchell [96] criterion that maximises the minimum distance between the points, r , p and q i.e.

$$\max \left\{ \min_{1 \leq p \neq q \leq N} r_{pq} \right\} \quad (5.4)$$

The second one, on the right for comparison, distributes the points as uniformly as possible by minimising the following function of the distance between points:

$$\sum_{p=1}^N \sum_{q=p+1}^N \frac{1}{r_{pq}^2} \quad (5.5)$$

This is achieved by using a permutation Genetic Algorithm, Bates *et al.* [97]. These results suggest that the Optimal Latin Hypercube sampling method [97] is more effective at providing uniform sampling throughout the design space. Swidzinski [125] states LHS could be nearly five times more effective in yield estimation than traditional sampling methods.

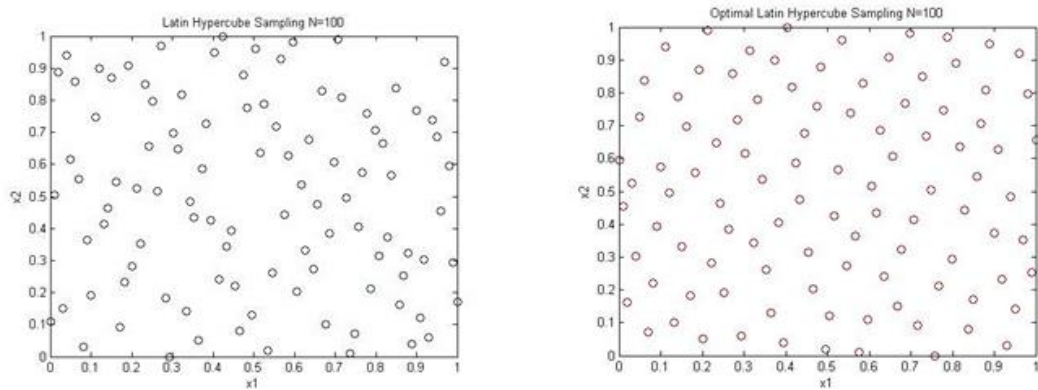


Figure 5.5 Comparison between LHS and OLHS for 100 design variables [97]

There is not so many recommendations or estimates for the sample size of LHS in the literature and determining the sample size is not a simple task [81]. The problem with LHS is that the resulting spread of points can vary significantly from one DoE to another which may lead to regions of design space which are under or over sampled [77]. Bates *et al.* [6] confirms that Optimised Genetic Algorithm require on average 46-times fewer function evaluations to reach comparing to Random Genetic Algorithm [6]. There is generally no best choice, although several DoE techniques are available. Key issues to be considered include [123]:

- Number of affordable experiments (N)
- Number of design variables (K)
- The number of levels for each parameters
- The purpose of the DoE

5.3. Response Surface Methods (RSM)

The computational cost of complex scientific and engineering simulations makes it impractical to rely on them exclusively for design studies. Using approximations in such cases lead to substantial savings of computational resources. The most extensive applications of RSM are in the situations where several input variables potentially influence some performance measure or quality characteristic of the process. Thus performance measure or quality characteristic is called the response. Once an appropriate DoE has been selected, the designated design parameters are used as input variables for generating high fidelity CFD responses. These responses values are then used to assemble the Response Surface. Response Surface Methods are used when an outcome of interest cannot be easily directly measured in an engineering system and also when measuring it is time consuming. Therefore a model of the outcome will be used instead. Using Response Surface models can reduce design cycle times and cost by enabling rapid analysis of alternative designs. In competitive, technically challenging environments, Response Surface models can reduce program cost and increase the efficiency of the design process. These approximation models can be applied in different phases and aspects of the engineering design process. It can also be used in design optimisation when the computational expense of simulations is large [126]. Response surface modelling is a statistical method for approximating design space using function values at certain points in the design space [6]. As the form of the response function f , is unknown, we need to approximate it. In fact, successful use of RSM depends on the experimenter's ability to develop a suitable approximation for f . usually, a low-order polynomial in some small region is appropriate. In many cases, first-order and second order models are used. The first-order model is appropriate when the experimenter is interested in approximating the response surface over a small region of the independent variable space in a location where there is little curvature in f . For the case of two independent variables (x_1, x_2) , the first-order model in terms of the coded variables is

$$\eta = \beta_0 + \beta_1 x_1 + \beta_2 x_2 \quad (5.6)$$

The curvature in the response surface is often sharp and strong that the first-order model is not sufficient. Therefore there is a need to use a second-order model. For the case of two variables, the second-order model is [9]:

$$\eta = \beta_0 + \beta_1 x_1 + \beta_2 x_2 + \beta_{11} x_1^2 + \beta_{22} x_2^2 + \beta_{12} x_1 x_2 \quad (5.7)$$

The second-order model is widely used in response surface methodology for the above reasons [9]:

- 1) The second-order model is very flexible and it can take on a wide variety of functional forms, so it will often work well as an approximation to the response surface.
- 2) It is easy to estimate the parameters (the β 's) in the second-order model. The method of least squares can be used for this purpose.
- 3) There is considerable practical experience indicating that second-order models work well in solving real response surface problems.

In some rare situations, order of greater than two is used. Figure 5.6 illustrates a simple example of second order Response Surface consisting of 5 points.

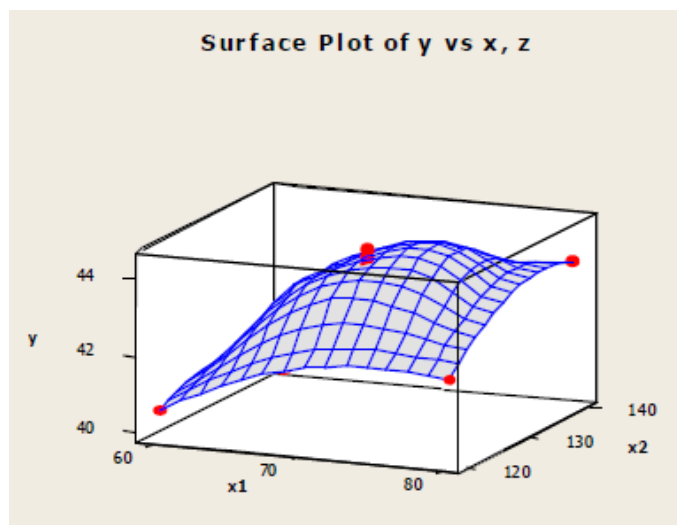


Figure 5.6 Second order Response Surface Plot [9]

Broadly speaking there are two types of Response Surface models:

- Interpolation
- Regression

Interpolation-based Response Surface is constructed by forcing the Response Surface to pass through solution points upon which they are built. Examples includes Polynomial Regression (PR) and Kriging (KRG) [3, 77]. Whilst these

methods have merits, they do not account for errors in solutions. In contrast, a feature of Moving Least Squares (MLS) Response Surfaces is that they are built using approximations [12], which make allowances for numerical noise (refer to chapter 4.6) by selecting an appropriate closeness of fit parameter, θ , for a given data set. Supposing the noise levels are high then the Response Surface can be loosely fitted to the points. Alternatively, a close fit can be used if the noise levels are small. When using approximations, there is a tradeoff between accuracy and efficiency then the question is how to generate an accurate representation of the response with a low cost or better an affordable cost. There are several methods that can be used to evaluate these polynomial approximations, two different algorithms that are mostly implemented, are Kriging, Least Square (LS) and Moving Least Squares (MLS). The main focus will be on Moving Least Square Methods as it is the most suitable method for this study which is noisy and has been used often in the recent years and will be used in this study.

5.3.1. Kriging

Kriging is a group of special statistical techniques to interpolate the value of a random field at an unobserved location from statistical observations of its value at nearby locations. The theory behind it, was developed by the French mathematician Georges Matheron based on the Master's thesis of Daniel Gerhardus Krige [90]. Kriging is known to be the best linear unbiased estimator of the Response Surface approximation. In the kriging process the sum of weights assigned to the input data is adjusted to one, and the error of estimation is kept to a minimum. Kriging uses a method, which DoEs not depend on the actual value of the variable, but depends on its spatial distribution and internal spatial structure. Simplified kriging equation, is as following:

$$Z_x^* = \sum w_i Z(x_i) \quad (5.8)$$

where, w_i is the weight assigned to the sample Z at location x_i and $\sum w_i = 1$.

The kriging weights are derived based on a data-driven weighting function which would make the sum of the weights equal to one, therefore it reduces the effect of bias towards input sample values. Kriging technique is popular in mining industry which is due to the realistic resource model that is created when kriging parameters are defined [110]. Kriging is an optimal prediction method designed initially for geophysical variables with a continuous distribution. Kriging belongs to the family of linear least squares estimation algorithms. The variable values are random but their variation is not described by any geometric function. Kriging interpolates an

elevation value for each output cell by calculating a weighted average of the elevations at nearby vector or database points. Closer points/nodes are weighted more heavily than more distant ones in the calculation. The Kriging method analyzes the statistical variation in values over different distances and in different directions to determine the shape and size of the point selection area as well as the set of weighting factors that will produce the minimum error in the elevation estimate. If the approximation type is Kriging, the polynomial order of the approximation is automatically chosen [93].

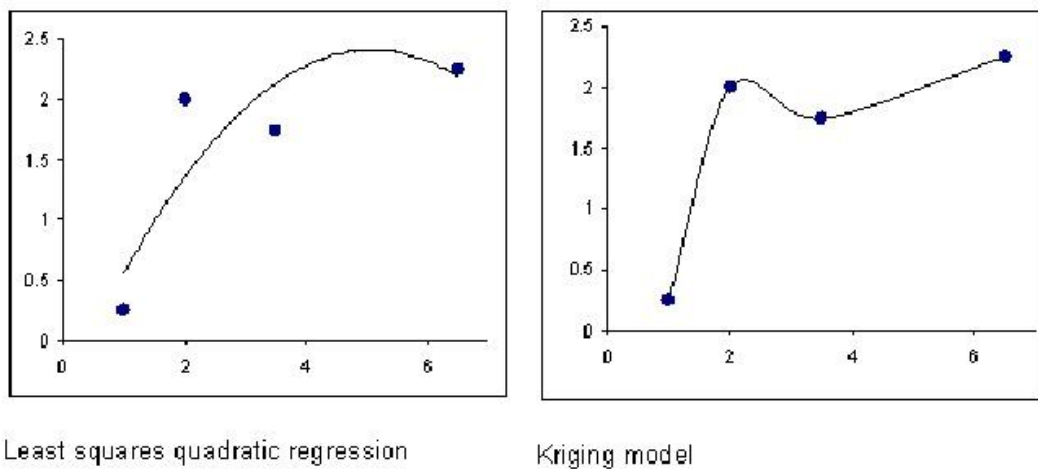


Figure 5.7 Examples of Kriging and least square quadratic regression model [93]

5.3.2. Least Square Method

The fundamentals for least-squares analysis was developed by Carl Friedrich in 1795. However Legendre was the first to publish the method. If a scatter plot shows a linear relationship between two variables, least-squares regression is a method for finding a line that summarizes the relationship between the two variables, at least within the domain of the explanatory variable, x . The least-squares regression line (LSRL) is a mathematical model for the data. A straight line that describes how a response variable y changes as an explanatory variable x changes is the regression line. It can sometimes be used to predict the value of y for a given value of x and residual is a difference between an observed y and a predicted y [87]. In least squares methods, if there are n points giving a response f as a function of number of design variables x_1, x_2, \dots, x_{ndv} , the purpose is to look for polynomial fit of the data. For example for a linear fit for two design variables, the data will be fitted to a hyper-plane of the form: $f = c_1 + c_2x_1 + c_3x_2$. The goal is then to find the 3 regression coefficients c_1, c_2, c_3 . Standard regression analysis minimises the sum of

the squares of the differences (Square Errors, SE) between the data points and the fitted curve. For this example [88]:

$$SE = \sum_{i=1}^n (f_i - c_1 - c_2 x_{1,i} - c_3 x_{2,i})^2 \quad (5.9)$$

Where, f_i is the response at the i th sampling point $x_{1,i}, x_{2,i}$. To find the regression coefficients c_i which minimise the SE following equations need to be satisfied [88]:

$$\frac{\partial SE}{\partial c_1} = -2 \sum_{i=1}^n (f_i - c_1 - c_2 x_{1,i} - c_3 x_{2,i}) = 0 \quad (5.10)$$

$$\frac{\partial SE}{\partial c_2} = -2 \sum_{i=1}^n (f_i - c_1 - c_2 x_{1,i} - c_3 x_{2,i}) x_{1,i} = 0 \quad (5.11)$$

$$\frac{\partial SE}{\partial c_3} = -2 \sum_{i=1}^n (f_i - c_1 - c_2 x_{1,i} - c_3 x_{2,i}) x_{2,i} = 0 \quad (5.12)$$

Which leads to the three regression equations:

$$n c_1 + c_2 \sum_{i=1}^n x_{1,i} + c_3 \sum_{i=1}^n x_{2,i} = \sum_{i=1}^n f_i \quad (5.13)$$

$$c_1 \sum_{i=1}^n x_{1,i} + c_2 \sum_{i=1}^n x_{1,i}^2 + c_3 \sum_{i=1}^n x_{1,i} x_{2,i} = \sum_{i=1}^n f_i x_{1,i} \quad (5.14)$$

$$c_1 \sum_{i=1}^n x_{2,i} + c_2 \sum_{i=1}^n x_{1,i} x_{2,i} + c_3 \sum_{i=1}^n x_{2,i}^2 = \sum_{i=1}^n f_i x_{2,i} \quad (5.15)$$

Equations above will be solved to obtain the regression coefficients c_1, c_2, c_3 . Least square method is widely used to estimate the numerical values of the parameters to fit a function to a set of data and to characterise the statistical properties of estimates. Its simpler version is called ordinary least squares and a more sophisticated version is called weighted least squares [89].

5.3.3. Moving Least Square Method

Another type of Response Surface modeling is moving least square method (MLSM) which was proposed by Lancaster and Salkauskas [111] for smoothing and interpolating data. This model has been suggested for the use in the mesh-less form of finite element method [115] and recently proposed for the design optimisation applications [127]. It is similar to the traditional weighted least square method but weights do not remain constant and are the function of Euclidian distance from a sampling point to a point x where the surrogate is evaluated and the weight decays

as a point x moves away from x_i . Since the magnitude of the weight function changes or moves with x , the approximation is called Moving Least Squares. This is a modified method for estimating a function, f , at an arbitrary point $\{x\} = \{x_1, x_2, \dots, x_{ndv}\}$ based on the values at a series of sampling points $\{f_i\} = \{f_1, f_2, \dots, f_n\}$ at a series of design points $\{x_{1,i}, x_{2,i}, \dots, x_{ndv,i}\}$ in order to estimate the following:

$$\hat{f}(x) = \sum_{i=1}^n w_i(\|x - x_i\|) f_i \quad (5.16)$$

where $r_i = \|x - x_i\|$ is the Euclidean norm. Hence the estimate to the response function would take the form:

$$\hat{y}(x) = \sum_{i=1}^n w_i(r_i) f_i \quad (5.17)$$

It is possible to control the closeness of the fit of the approximation by changing a parameter in a weight decay function $w_i(r)$ where i is the distance from the i -th sampling point. This feature allows the model to handle the issue of numerical noise in the response by adjusting the closeness of fit, setting it to a close fit in a noiseless situation or changing it to a loose fit when the response contains considerable amounts of numerical or experimental noise. The weighting of points in the regression coefficients calculation are determined using a Gaussian decay function, which is the most popular decay function, see equation (5.18) [128]:

$$w_i = \exp(-qr_i^2). \quad (5.18)$$

where w is the weighting of the DoE build point, θ is a closeness-of-fit parameter, i , r_i is the normalised distance from the current point to model building point i , and, with the value $\theta = 0$ equivalent to traditional least squares regression and when the parameter θ is large it is possible to obtain a very close fit through the sampling points. Other typical functions for weight decay are as below [128]:

$$\text{Cubic polynomial} \quad w_i = 1 - 3p_i^2 + 2p_i^3 \quad (5.19)$$

$$\text{fourth order polynomial} \quad w_i = 1 - 6p_i^2 + 8p_i^3 - 3p_i^4 \quad (5.20)$$

Where $p_i = r_i/R_{max}$, R_{max} is the normalised radius of the sphere of the influence which is inversely related to the closeness of fit parameter, with the smaller value of R_{max} , closer fit will be obtained. Toropov [128] mentions that the moving least squares method is powerful approximation technique and has a great potential for many design optimisation applications and stochastic analysis. It can produce a high quality surrogate model for a highly nonlinear behaviour of an engineering system and it can efficiently handle the issue of numerical noise by adjusting the closeness of the fit.

5.4. Optimisation Techniques

Once a Response Surface is constructed using an appropriate number and distribution of points, the next step, in the process, is to optimise the Response Surface in search of the global minimum. Optimisation is the act of obtaining the best result under given circumstances the ultimate goal of such a process is normally to find the minimum or maximum. Therefore optimisation can be defined as the process of finding a condition that gives the minimum or maximum. Some of the engineering applications of optimisation are, design of the aircraft for minimum weight, design of civil engineering structures such as frames, bridges, towers and dams for minimum cost [124]. Optimisation can be traced to as early days as Newton, Lagrange and Cauchy. Some of the foundations were laid by Bernoulli, Euler, Lagrange and Weierstrass. Only little progress were made until the twenty century when high speed digital computers appeared. In 1960s, major developments were made in United Kingdom such as development of simplex method by Dantzig in 1947 [129] for linear programming, and the introducing the principle of optimality by Bellman in 1957 [126] for dynamic programming problems. Multi-objective programming was developed as a result of desire to optimise more than one objective while satisfying the physical limitation. Goal programming (well-known technique for solving multi-objective optimisation problems) was proposed by Charnes and Cooper in 1961. In recent year the modern optimisation techniques have been emerged which include Genetic Algorithms, ant colony optimisation, particle swarm optimisation, neural network based optimisation, simulated annealing and fuzzy optimisation. Genetic Algorithms were first introduced by John Holland in 1975 [130]. It is a computerised search and optimisation algorithm based on the mechanics of natural genetics and natural selection. Simulated annealing was developed by Kirkpatrick et al. [131] which is based on the mechanics of the cooling

process of molten metals through annealing. The particle swarm optimisation algorithm was inspired by the behaviour of social organisms such as swarms or insects and it was proposed in 1995 by Eberhart and Kennedy [132]. The ant colony optimisation was first developed by Marco Dorigo in 1992 [125] and is based on the cooperative behaviour of ant colonies. Neural network method is based on immense computational power of the nerves system to solve the parallel processing capabilities which was used first for the optimisation by Tank and Hopfield in 1985 [127]. The fuzzy optimisation method was first presented by Rao in 1986 [124] and it was developed to solve optimisation problems which involved design data, objective function and constraints. An optimisation problem can be defined and stated mathematically as follows:

$$\text{Find } X = \begin{Bmatrix} x_1 \\ \vdots \\ x_n \end{Bmatrix} \text{ which minimizes } f(X) \quad (5.21)$$

Subject to the constraints

$$a_j(X) \leq 0, \quad j = 1, 2, \dots, n \quad (5.22)$$

$$b_j(X) = 0, \quad j = 1, 2, \dots, m \quad (5.23)$$

Where X is an n -dimensional vector called the design vector and $f(X)$ is called objective function. $a_j(X)$ and $b_j(X)$ are termed as inequality and equality constraints respectively. The problem stated above is called constrained optimisation problem. Some problems are without any mentioned constrained and called unconstrained optimisation problem.

5.4.1. Design constraints

The design variables, in many practical problems, have to satisfy certain functions and other requirements and cannot be chosen arbitrarily. These restrictions are called design constraints and need to be satisfied to produce an acceptable design. Some constraints represent behaviour or performance limitations and other represents physical limitations which are called functional and geometric

constraints. Figure 4.8 shows a two-dimensional design space where the infeasible region is indicated by hatch lines [112].

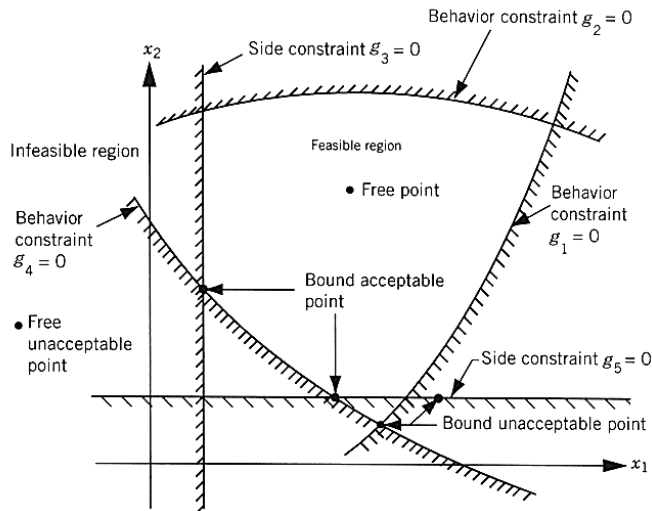


Figure 5.8 Constraint surface in a hypothetical two-dimensional design space [124]

5.4.2. Objective function

The aim of the conventional design procedure is to find an acceptable design that satisfies the constraints. There is normally more than one acceptable design in a design procedure and the goal of the optimisation is to choose the best one. Therefore there should be some criterion in order to compare the different acceptable designs and choose the best one. This criterion is called criterion or objective function. The choice of the objective function is governed by the nature of the problem. For example minimization of the weight is normally taken for the application of aircraft and aerospace structure design problems. For the mechanical engineering system, maximization of mechanical efficiency is often the choice of objective function. The surfaces created by the member of a family (C) is called objective function surface and are shown in a two-dimensional design space in Figure 5.9. Once the objective function surfaces are drawn with the constraint surfaces, the optimum point can be determined without much difficulty. Although as the number of design variables exceeds two or three it becomes very complex to visualize and the problem has to be solved purely mathematically.

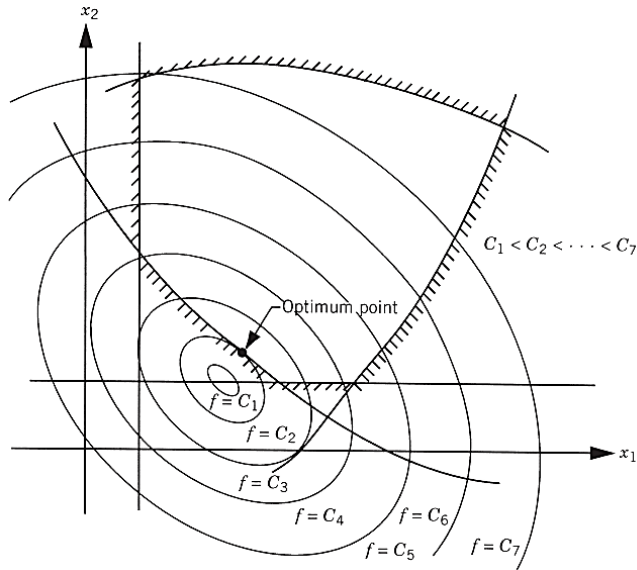


Figure 5.9 Contours of objective function [124]

5.5. Optimisation Approaches

Numerical optimisation techniques can be broadly classified as either deterministic or stochastic [107, 133] and stochastic programming problems [112]. The nature of the flow phenomena inside the enclosed spaces, such as in a wind tunnel, generates noisy outputs which in turn causes problems for deterministic method [117]. In most cases they are prone to find the local extreme and the convergence speed and final result are strongly dependent on the initial guess values [134]. In contrast, stochastic methods, also referred to as global methods are better suited to building or indoor environment applications. One of the most popular in this category and a widely accepted global optimisation technique is the Genetic Algorithms [135]. Inspired from Darwin's theory of natural selection, this method has demonstrated its capability to handle discontinuous variables and also noisy objective functions [136]. Furthermore, GA being a stochastic method has a better chance to explore the entire design space. Hence GA was chosen as the optimisation engine in all our study. The optimisation approach can be written mathematically as follows:

<i>Objective</i>	$\min(f(x))$
<i>Constraints</i>	$g_i(x) \leq 0$
<i>Design space</i>	$X^L \leq X \leq X^U$

There are two types of optimisation approach as mentioned below:

- Deterministic optimisation approach
- Stochastic optimisation approach

5.5.1. Deterministic optimisation approaches

Deterministic optimisation approaches try to find an acceptable solution to the design problem that minimizes the objective function. Deterministic optimisation problem formulation DoEs not consider uncertainty of design variables and response surfaces models tend to smooth the noisy behaviour. The design variables are deterministic and can be continuous or discrete quantities. Most optimisation algorithms push the constraints to the bounds in search of optimal solution and this in general leads to a not robust design, where any small change can make the system fail.

5.5.2. Stochastic optimisation approaches

Stochastic optimisation approaches attempt to model uncertainty in the data by assuming that (part of) the input is specified in terms of a probability distribution. Objective of the robust design problem is to bring the mean on target and minimize the variance. There are two objectives for robust designs [137]:

1. Minimize the variance of performance
2. Bring the mean on target or optimising the “mean of performance”

A deterministic model assumes that its outcome is certain if the input to the model is fixed and if the optimisation is repeated few times the same results will be obtained. robust model is more informative than a deterministic model since the former accounts for uncertainty due to varying behaviour characteristics. Stochastic is random and based on chance.

5.6. Optimisation Methods

There are several different methods of optimisation, two main optimisation methods will be discussed below and the focus will be on Genetic Algorithm which will be used in this optimisation study:

- (GA) Genetic Algorithm
- (SQP) Sequential Quadratic Programming
- Multi Approximation Method (MAM)

GA is a global search algorithm and SQP is an efficient local search algorithm.

5.6.1. Sequential Quadratic programming (SQP)

For SQP the objective function is replaced with a quadratic approximation [131] and the constraints of the problem are approximated linearly. The quadratic function is then solved in the search direction, leading to the local optimum. Sequential quadratic programming (SQP) is a method for solving non-linear and constrained optimisation problems. It attempts to solve a non-linear problem directly rather than convert it to a sequence of unconstrained minimization problems [132]. The solution of the problem indicates the search direction along which the next design that improves the objective function and DoEs not violate the constraint can be found [132].

5.6.2. Multi Approximation Method (MAM)

Multi approximation is an optimisation method where the original problem is replaced by succession of a simpler mathematical programming problem. The functions in each iteration present mid-range multipoint approximations of the corresponding original functions. These functions are noise-free or, at least, the level of noise DoEs not cause problems with convergence of an individual optimisation sub-problem. The solution of an individual sub-problem becomes a starting point for the next step, the move limits are changed and the optimisation is repeated iteratively until the optimum is reached. Various optimisation techniques can be used to solve the sub-problems because the approximation functions are chosen to be simple [138].

The technique allows to use in each iterations the information gained in several previous design points. It allows to consider, instead of the initial stochastic optimisation problem, a sequence of simpler mathematical programming problems and it results in reduction of number of simulations[138, 139].

5.6.3. Genetic Algorithm

Genetic Algorithm is a branch of Evolutionary computation which involves the reproduction, competition, random variation and selection of the individuals. since optimisation DoEs not imply perfection, evolution can only discover very precise solutions to certain problems [140]. Genetic Algorithm and Sequential Quadratic Programing are mainly used to find the global and local minima or maxima respectively, see Figure 4.11 [140]. Genetic Algorithms work on a whole population of individual, and encode candidate solutions using a specific representation scheme.

Genetic Algorithms operate on a set of possible solutions. Because of the random nature of Genetic Algorithms, solutions found by an algorithm can be good, poor, or infeasible, so there should be a way to specify how good that solution is. This is done by assigning fitness to the solution. Chromosomes represent solutions within the Genetic Algorithm. The two basic components of chromosomes are the coded solution and its fitness value [141-143]. Chromosomes are grouped into population on which the Genetic Algorithm operates (Population). In each step or generation, the Genetic Algorithm selects chromosomes from a population which is based on the fitness value of the chromosome and combines them to produce new chromosomes which are called offspring. These offspring chromosomes form a new population or replace some of the chromosomes in the existing population in the hope that the new population will be better than the previous ones. Populations keep track of the worst and the best chromosomes, and stores additional statistical information which can be used by the Genetic Algorithm to determine the stop criteria. A chromosome, in some way, stores the solution which it represents. This is called the representation or encoding of the solution. There are a number of probable ways to represent a solution in such a way that it is suitable for the Genetic Algorithm as stated below and they mostly depend on the nature of the problem [141, 144].

- binary,
- real number,
- vector of real number,
- permutations, and so on

chromosome 1	0	0	1	1
chromosome 2	0	1	0	1

binary representation

chromosome 1	3.0
chromosome 2	5.0

real-number representation

Figure 5.10 example of binary and real-number chromosome representation [144]

Genetic Algorithms produce new chromosomes or solutions by combining existing chromosomes. This operation is called crossover. A crossover operation takes parts of solution encodings from two existing parent chromosomes and combines them into a single solution which is a new chromosome [144].

chromosome 1	0	0	1	1
chromosome 2	0	1	0	1
offspring 2	0	1	1	1

binary representation
one-point crossover

chromosome 1	3.0
chromosome 2	5.0
offspring 1	4.0

real-number representation
mid-point crossover

Figure 5.11 Example of crossover operation for two different representations[144]

After crossover operation, GA performs a mutation operation before it produces the new population. A mutation operation makes small random changes to an encoded solution. This prevents the falling of all solutions into a local optimum and extends the search space of the algorithm. Mutations as well as crossover operations depend on the chosen representation [143].

chromosome 1	0	0	1	1	old
	0	1	1	0	new
chromosome 2	0	1	0	1	old
	0	1	0	0	new

Figure 5.12 Example of mutation operation for two chromosomes [144]

Crossover and mutation operations are not always performed when producing a new chromosome. If crossover is not performed, the Genetic Algorithm produces a new chromosome by copying one of the parents. The rates of crossover and mutation operations are called crossover probability and mutation probability, respectively. The crossover probability is usually high and around 80%, and the mutation probability is low and about 3%. A higher mutation probability can turn the Genetic Algorithm in to a random search algorithm[145]. The last operations defined by Genetic Algorithms used to manipulate chromosomes are fitness operations and fitness comparators. A fitness operation measures the quality of the produced solution which are chromosome. This operation is specific to the problem, and it actually tells the Genetic Algorithm what to optimise. Fitness comparators are used to compare chromosomes based on their fitness. A fitness comparator tells the Genetic Algorithm whether it should minimize or maximize the fitness values of chromosomes[145]. Choosing parents for the production of new chromosomes from a population is called selection. Selection can be based on many different criteria, but it is usually based on the fitness value. The idea behind this is to select the best chromosomes from the parents in the hope that combining them will produce better offspring chromosomes. But, selecting only the best chromosomes has one major disadvantage; all chromosomes in a population will start to look the same very quickly. This causes the followings [141, 142, 144]:

- Narrows the exploration space,
- Pushes the Genetic Algorithm into the local optimum,
- Prevents the Genetic Algorithm from finding possibly better solutions that reside in inaccessible areas of the exploration space.

To preserve the diversity of chromosomes and a wider exploration space within the population, selection operations usually introduce a factor of randomness in the selection process. Some implementations of selection operations are entirely random. One problem may occur with selection operations that are based on fitness values. When there is a chromosome with a dominant fitness value, it will be selected most of the times, thus it will cause problems similar to the existing ones.

To prevent this, fitness values can be scaled and transformed to lower the difference between dominant chromosome(s) and the rest of the population [this allows other chromosomes to be selected]. There are many ways to transform a fitness value. Usually, they are implemented by applying a mathematical transformation to the fitness value, but there are other methods like ranking based scaling that use the rank, based on the raw fitness values of chromosomes, of a chromosome as the scaled fitness value[145]. A coupling operation defines how the selected parent chromosomes are paired for mating [mating is done by performing a crossover operation over the paired parents and applying a mutation operation to the newly produced chromosome]. This operation gives better control over the production of new chromosomes, but it can be skipped and new chromosomes can be produced as the selection operation selects parents from the population [144]. The next step performed by a Genetic Algorithm is the introduction of new chromosomes into a population. Offspring chromosomes can form a new population and replace the entire previous population, or they can replace only a few chromosomes in the current population. For overlapping populations, the replacement operation defines which chromosomes are removed [usually the worst chromosomes] from the current population and which offspring chromosomes are inserted. By replacing chromosomes, there is a chance that the Genetic Algorithm will lose the best chromosomes which have been found so far and to prevent this, the concept of elitism is introduced into Genetic Algorithms. Elitism guarantees that the best chromosomes from the current generation are going to survive to the next generation [144]. An algorithm performs the previously described steps one by one in sequence, and when they have been performed, it is said that a generation has passed. At the end of each generation, the Genetic Algorithm checks the stop criteria. Because of the nature of Genetic Algorithms, most of the time, it is not clear when the algorithm should stop, so a criteria is usually based on statistical information such as the number of the generation, the fitness value of the best chromosome, or the average fitness value of the chromosomes in the population, the duration of the evolution process [142].

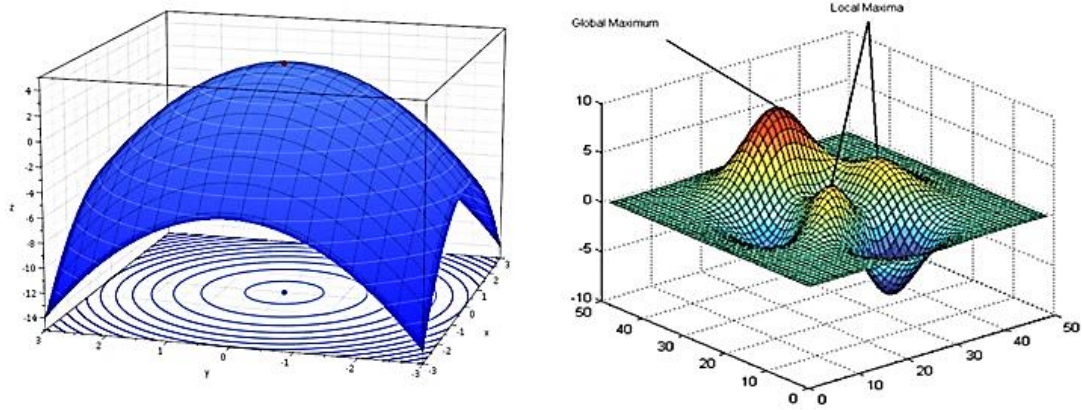


Figure 5.13 Illustration of global and local maxima [94]

Genetic Algorithms (GAs) are ideally suited to find the optimum and the local minimum because even if the location of the optimal solution is unknown, they can effectively search space to find the candidate. Conceptually GAs are based on natural selection, whereby survival of the fittest ensures that the best solution(s) are found [130]. Depending on how complex the objective function is, the application of GA may locate a solution which is very close to the global optimum, but a local gradient based search method would then be required, using GA results as a starting location. The Sequential Quadratic Programming (SQP) technique is a typical example of this but because it is limited to local optimisation for which an initial good guess of the solution is required.

6. CFD and Experimental Validation Study of Emergency Response Vehicles

For all their advantages, computational approaches are purely simulation tools and there is no substitute for working with the actual fluid itself. It follows that in order to gauge the degree to which CFD simulations correlate with reality, they should be validated against real experimental data. Not only the experimental data are used to validate the numerical simulations but they are also useful in their own right. For validating the computational results, the low speed wind tunnel of Queen Mary University of London is used. The advantage of low speed wind tunnel testing is that the environment can be controlled. However using scaled model will not yield the exact conditions of the full scale model. The scale must be chosen carefully based on the test section size of the wind tunnel. This would reduce the magnitude of aerodynamic problems introduced by the wind tunnel walls and stationary floor. Therefore resulting data is different from full-scale road testing but practice shows that wind tunnel testing when correctly proceeded has an accuracy of about 90% [17, 19, 21, 35, 37]. The purpose of this chapter is to provide data by which the accuracy of the CFD simulations can be assured.

6.1. Experimental techniques

Despite the progress in the CFD simulations with high powered computers, there are still considerable limitations and there is no simple method for prediction of the aerodynamic characteristics of road vehicle [91]. Therefore it is necessary to use wind tunnel and road testing both to generate accurate data and to validate CFD models.

6.1.1. Wind Tunnel Approach

The principle of the wind tunnel is very straightforward, rather than moving the object and measuring the flow behaviour, it just moves the air over objects; all the important flow behaviour can be observed and also measured.

6.1.2. Different Types of Wind Tunnels

Wind tunnels were originally used for aeronautic applications and in the recent years some wind tunnels have been evolved for automotive work such as the one used by

MIRA in Nuneaton and Quatro Park UK [119] with test section area of 15m length x 7.9m width x 4.4m height with a cross-sectional projected area of 35m². There are two different types of wind tunnel [85]:

- Closed-return type: air circulates around a continuous closed circuit.
- Open-return type: it consists of a tube which is open at both ends and air is drawn from and returned to the surrounding environment.

Figures 6.1 and 6.2 show the schematic drawing of these two different types of wind tunnels. They are both capable of giving accurate results, but the closed-return type is often preferred for the practical reasons such as flow not having to exit the tunnel.

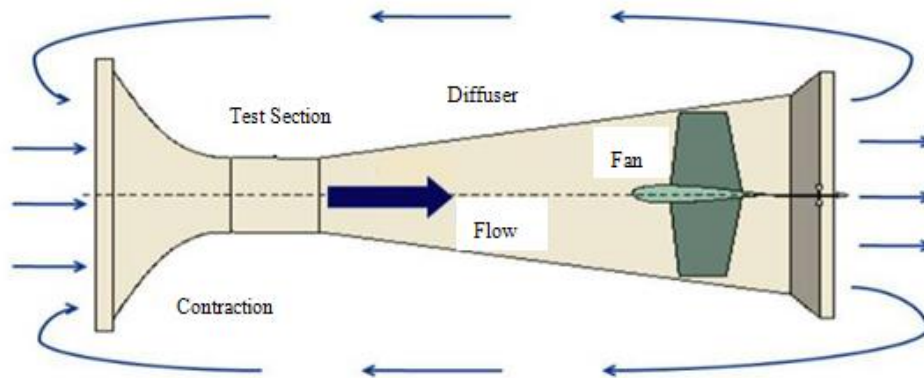


Figure 6.1 Open Return Wind Tunnel [62]

In the inlet of the wind tunnel where flow enters, there is a flow straightening device which would reduce the free stream turbulence and also stops the foreign objects entering the tunnel. The flow starts accelerating in the contraction region. Generally, large inlet contraction ratio improves the steadiness and uniformity of the flow in the test section. Fan is placed downstream of the tunnel which pulls the air through the tunnel. Typically the ground vehicles are mounted within the working section on top of a ground board to raise the model above the tunnel boundary layer or on a rotating belt which simulates the moving ground plane. Wind tunnels are normally characterised by the cross-sectional dimensions of their working section.

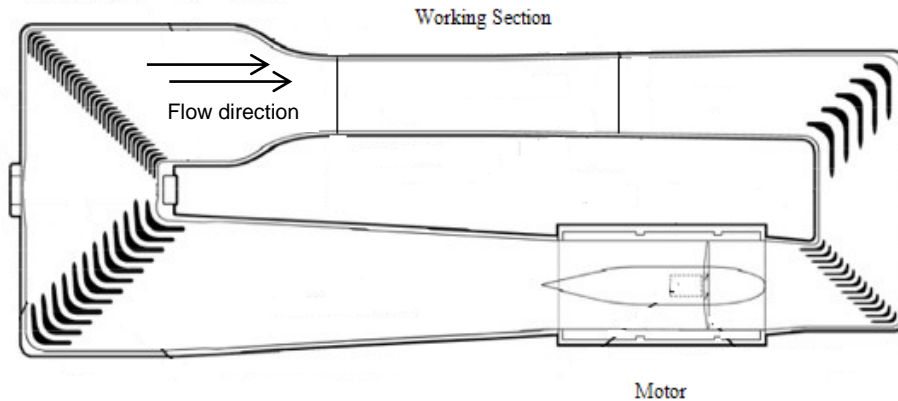


Figure 6.2 Closed Return Wind Tunnel [63]

6.2. Factors affecting the accuracy of the wind tunnel testing

In the wind tunnel testing, the flow conditions such as air velocity, relative humidity and even the density in the closed-circuit tunnels can be controlled. This is very helpful since there is no substitute for air to do the experiment with. Therefore it makes it a reliable candidate to obtain experimental data. On the other hand it has disadvantages [85, 91, 146]. There are issues that affect the accuracy of data that have been obtained using wind tunnel tests such as [85, 91, 146]:

- 1) Scale or Reynolds number effect
- 2) Road moves relative to the car instead of car moving
- 3) Blockage error
- 4) Failure to model fine detail accuracy
- 5) Difficulties to measure forces when wheels are in contact with the road

Each of these issues is described briefly below:

6.2.1. The Scale or Reynolds number effect

The effect of the scaling and or the Reynolds number is an important issue in the wind tunnel experiment. It arises from the fact that the model is scaled and the Reynolds number changes due to the length of the model. To obtain similar flow patterns and features for both full scale and model, the Reynolds number must be the same for both [79], in an example with a scaling from 5m to 0.6m, we get:

$$\frac{\rho V l}{\mu} \text{ model} = \frac{\rho V l}{\mu} \text{ full scale} \quad (6.1)$$

$$\frac{1.22 \times 26.64 \times 0.6}{2 \times 10^{-5}} \text{ model} = \frac{1.22 \times 26.64 \times 5}{2 \times 10^{-5}} \text{ full scale}$$

$$975025 \neq 8125200$$

Where, ρ is the density of air, V is the velocity of the air, l is the length of the model and μ dynamic viscosity of the air. If the Reynolds number (density, viscosity and the velocity of the air) is kept the same as the real one, then the transition of the flow would occur at the corresponding place as the real model, this can have important consequences on measurements, as shown for example in the Figure 6.3. Since the model has been scaled and is a lot smaller than the real one, it will have a greater proportion of laminar boundary layer and consequently lower drag per unit of surface area than the larger one.

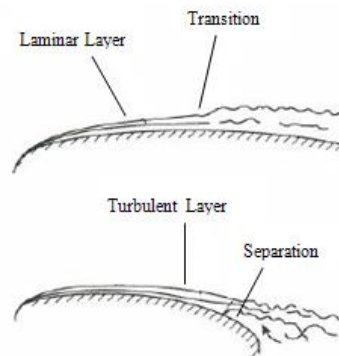


Figure 6.3 Schematic showing scale effects in vehicle aerodynamics [85]

Unless something is done to the velocity, density or the viscosity of the air, the model would not be representative of the full scale. They have to be changed in the scale of $1/8^{\text{th}}$ for our experiment in order to move forward the transition. Scaling the velocity means that the wind tunnel is run with the velocity close or even above the speed of sound (343 m/s). This would not be possible and the flow field will not be similar to the real world. Increasing the density or decreasing the viscosity of the air in order to equalise the Reynolds number to the full scale model, is also not practical. One way to bring the transition further up is to make the surface of the model not as smooth as that of the real one. Slight roughness causes the flow to become turbulent faster [79, 85, 146].

6.2.2. Road moves relative to the car instead of car moving

Under real road conditions, no boundary layer is developed on the road since there is no relative motion between the road and the air. However in wind tunnel, a boundary layer is developed on the floor and the model will be partially immersed in it and this will affect the results. Some of the correction methods are listed below in order to minimize the effects of formation of the boundary layer [100]:

- Use of ground board
- Use of belt moving at the same speed as the wind, with boundary layer removal upstream
- Use of a porous floor with suction
- The mirror image method

Each of these is described briefly in the following.

6.2.3. The ground board method

The simplest method to eliminate the effect of the boundary layer is the ground board method and can give satisfactory results [100]. The board is mounted above the tunnel boundary layer, and although there is relative motion between the air and the board, the resulting boundary layer is thin. To compensate for even this thin boundary layer, model can be raised by the amount of boundary layer displacement thickness: the amount by which the boundary layer displaces the streamlines upward [100]. The length of the board influences the drag coefficient measurement. The drag coefficient is quite sensitive to the length of the plate downstream of the rear of the model. The minimum necessary appears to be the length three times of the model and the maximum error occurs when the downstream length equals the model width. The ground board length influences the wake structure and therefore drag coefficient changes [100].

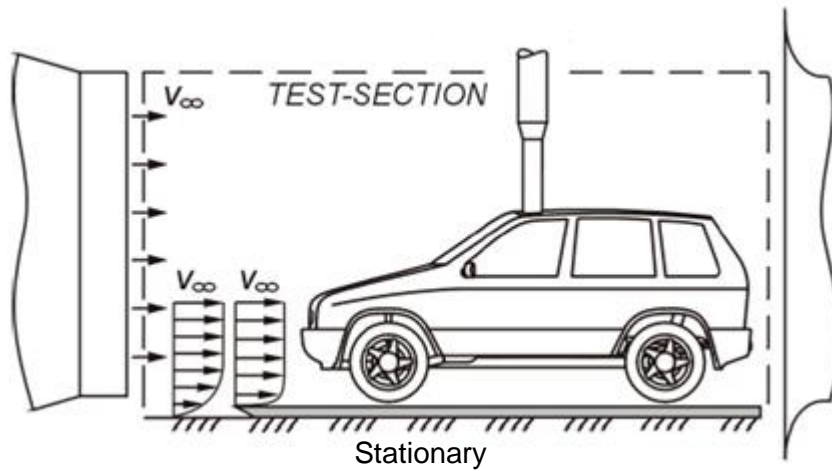


Figure 6.4 Principle of experiment, with stationary ground and wheel [18]

6.2.4. The moving belt method

The moving belt replicates the fact that there is no relative motion between the road and the air. The floor boundary layer has to be fully removed just upstream of the model by suction. There are several problems with the use of a moving belt [85, 147]:

- Belts normally vibrate and care needs to be taken to minimize belt fluctuation.
- Suction in front of the belt needs to be carefully adjusted as too much suction causes excessive friction and heating and too little suction causes the belt to billow upwards.
- Breakage of the belt can destroy an expensive model.
- Model cannot be mounted from underneath and has to be supported either from above or behind.

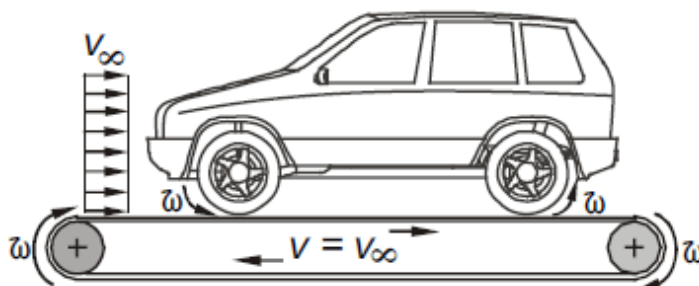


Figure 6.5 Principle of the moving belt [148]

Testing using moving belts, is complicated and expensive however if tests are conducted with sufficient care and skill, the result gives a good representation of road driving [149, 150]. Despite finding that the moving belt can produce significantly different result compared with a fixed ground, Howel [94] argues that in a comparative testing, such as early development of passenger cars where the criteria is to generate a shapes for minimum drag, to understand trends available and to avoid critical geometries, fixed ground is adequate for assessing underbody shape [151]. It is a common practise to simply mount the vehicle on the floor of the tunnel, in scale tests on anything other than the competition car, despite all the methods for removing the floor boundary layer. This is justified when comparative rather than absolute measurements are required [85].

6.2.5. Blockage effects

Blockage effect is also an important issue in wind tunnel testing. When the model is placed inside the wind tunnel it blocks the tunnel and the average air speed on that specific area is increased. The wake behind the vehicle also increases the blockage effects [100]. Since the air is speeded up around the object, the force becomes larger and therefore the corresponding drag and lift coefficient will be overestimated if no correction is applied. The blockage is defined as an effective reduction in flow area and represented by [146] :

$$Blockage = \left[1 - \left(\frac{Effective\ area}{Geometric\ area} \right) \right] \quad (6.2)$$

A blockage correction can be calculated based on the mass conservation that states the same amounts of mass of air must flow through all parts of the tunnel. Mercker (1985) gives a blockage correction expression for vehicles as follow:

$$C_D = C_D(Indicated) \left(1 - \frac{1.3A}{S} \right) \quad (6.3)$$

Where, S is the projected area of the tunnel working section and A is the projected area of the model. There cannot be any correction factor that can take full amount of the distortion that the wall imposes on the flow and it is always advisable to use small blockage ratio, ideally less than 5%. The goal of the experiments is to verify that the changes due to aerodynamic designs are significant. It is also used to validate the CFD results. For such a test, results can be obtained using scale models

in small wind tunnels and the effects of using wrong Reynolds numbers are often ignored [85]. In the real life, vehicle moves through space which is unlimited in all directions (free air), the road below being the only limiting surface. However the dimension of the wind tunnel sections is finite. Therefore the flow around the vehicle will be modified compared to the unlimited space. Angularity of the flow, the distribution of the velocity and pressure around the vehicle are all modified and consequently forces and the moments acting on the vehicle are modified. The smaller a wind tunnel relative to a vehicle, the larger are these discrepancies [79]. As long as the only objective of the specific investigation is to measure the effect of shape modifications on the flow around the vehicle, and specifically drag, these discrepancy may be tolerable, provided the wind tunnel has a reasonable size [79].

6.2.6. Importance of Modelling Fine Detail

One of the difficulties with the wind tunnel experiment is the necessity to model the object in fine details. Study done by Olson and Schaub [152] which compares the drag coefficient of a detailed model of a truck with simpler block form model found 11% drag coefficient difference between two models. Therefore detailed fine modelling is required for the wind tunnel testing despite it makes it extremely expensive [100].

6.3. Flow Measurement and Visualisation

Similar to aircraft model, car model can be mounted in the same way, either on a set of supports connected to an external force-measuring system or on a rigid sting with an internal miniature multiple-axis force measuring transducer. Overall forces can be measured in this manner. Local surface pressure can also be measured on small models by drilling a small holes or pressure tapping through the surface. Tube is connected to the hole in one end and pressure measuring device at other end. Very sensitive pressure transducer is used, in recent years, which produces an output voltage proportional to the applied pressure. Drilling pressure tapping, on full scale cars, would be a very highly destructive form of testing, and as an alternative, very small static pressure probes with 0.5 mm thick can be tapped directly on to the external surface of the vehicle. The technique will slightly affect the boundary layer flow, but to an acceptable degree [85]. There are few methods available for visualizing the structure of the airflow patterns around the vehicle [85]:

- Smoke visualisation; useful to identify the area of separation, reattachment and recirculation.
- Fine powder painting suspended in oil or paraffin; Provides information on the location of transition, separation and reattachment lines.
- Wool tufts; useful to show the indications of regions of separation, attachment, reverse flow, vertical flow and high turbulence as well as indication of the flow direction, See Figure 2.13.

Smoke visualisation is the most common method in flow visualisation. Figure 6.6 demonstrates a hand held smoke visualisation used to observe the flow behaviour over the full scale tractor-trailer in wind tunnel. The problem with smoke is that it mixes rapidly in the turbulent flow region which is area of interest and also in the case of closed return type of tunnel, the whole tunnels rapidly fills with smoke [100].



Figure 6.6 Full-Scale Wind Tunnel Tests of Production and Prototype, Second-Generation Aerodynamic Drag-reducing Devices for Tractor-Trailers [153]

As shown in Figure 6.7 small tufts of wool attached to the vehicle surface give an indication of regions of separation, attachment, reversed flow and the local flow directions.



Figure 6.7 Tufts visualisation on a real car [64]

6.4. Wind Tunnel Experiment

The aim of this experiment is to compare the drag force/coefficient of generic model of Vauxhall Vivaro with numerical CFD results and validate the optimisation work. The experimental results will also be used to assess if the aerodynamic improvements of the optimum design are significant. The experimental results will be used to compare with the numerical simulation of different turbulent models and different mesh element sizes in order to find out which turbulent model and element size is appropriate for simulating the flow around the van and calculates the drag force.



Figure 6.8 Real model of Vauxhall Vivaro [153]

The dimension of the wind tunnel used in the experiments at Queen Mary University of London, is 1m x 0.7m with the maximum velocity of 35m/s as shown in Figure 5.8. The generic model of Vauxhal Vivaro (Figure 5.9) was drawn using design modeller [93] which has a projected area of 4.22m². It was then scaled to 1/8th which would give projected area of 0.06624m². The intention of scaling was to reduce the

blockage area to an acceptable level, which is less than 10% for low speed wind tunnel [86]. The blockage area for the scaled model is 8.5% as it is calculated below.

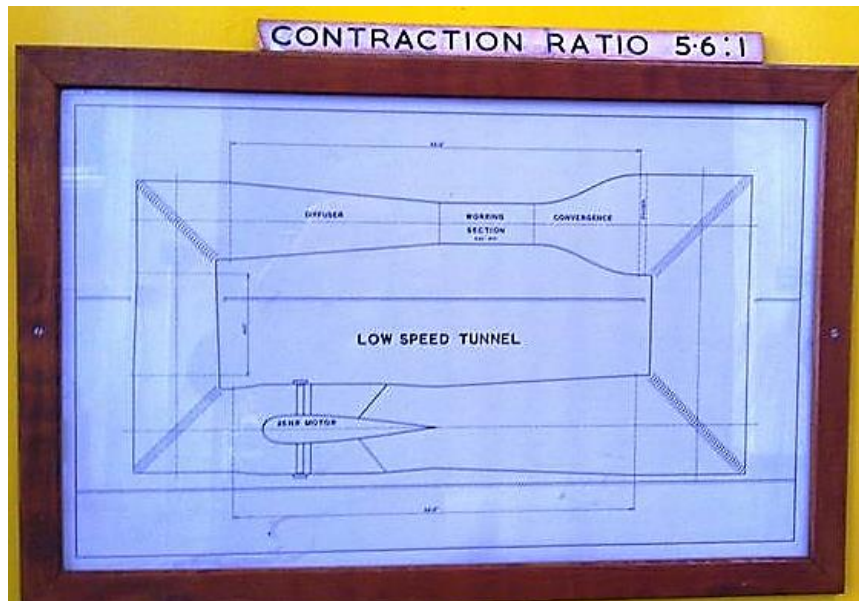


Figure 6.9 Generic Schematic of Queen Mary University of London Wind Tunnel

If projected area of the vehicle, test section area and scale ($1/8^{\text{th}}$) are known, the blockage area can then be calculated as below [85] :

$$\frac{100}{\text{Wind tunnel cross section area}} \times \frac{\text{Vehicle frontal area}}{(\text{Scale factor})^2} = \text{Blockage area}$$

$$\frac{100}{0.7} \times \frac{4.22}{(8)^2} = 8.5\%$$

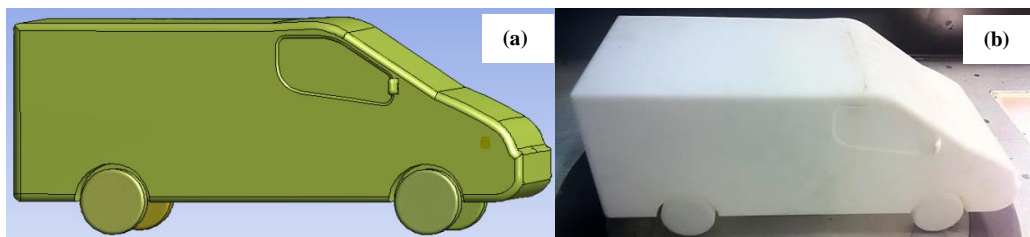


Figure 6.10 Generic model of Vauxhall Vivaro

The model was built using 3D print by ‘‘laserlines’’ Company [93]. In the later stages of the experiment, light-bars (Figure 6.11) will be added to measure the

effects of the light-bars on the drag. The work is solely focused on the effect of the light bars; other parts of the vehicle are not considered.

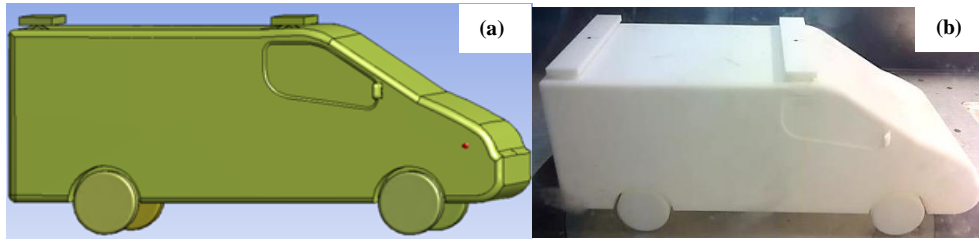


Figure 6.11 Vehicle with light-bars, (a) CAD model, (b) Physical wind tunnel model

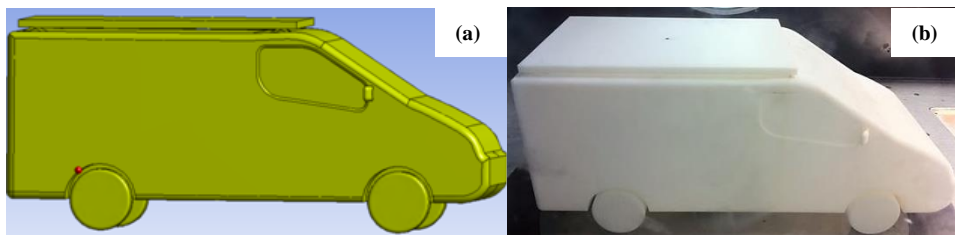


Figure 6.12 Vehicle with flat light-bars, (a) CAD model, (b) Physical wind tunnel model

6.4.1. The Queen Mary Wind Tunnel

For the present study, a low-speed facility at the Queen Mary University of London was used, see Figure 6.14. Its dimensions were measured so that a CAD model could be constructed for the subsequent CFD analysis.



Figure 6.13 Queen Mary University of London Wind tunnel

6.4.2. Experimental Methodology

Figure 6.14 shows the 1/8th scaled model inside the wind tunnel. It was placed and fixed on the scale in order to measure the drag force. As discussed below, the model was placed 3mm above the floor of the wind tunnel, above the turbulence boundary layer thickness as calculated below, in order to minimize the effect of the wind tunnel boundary layer (Figure 5.15).

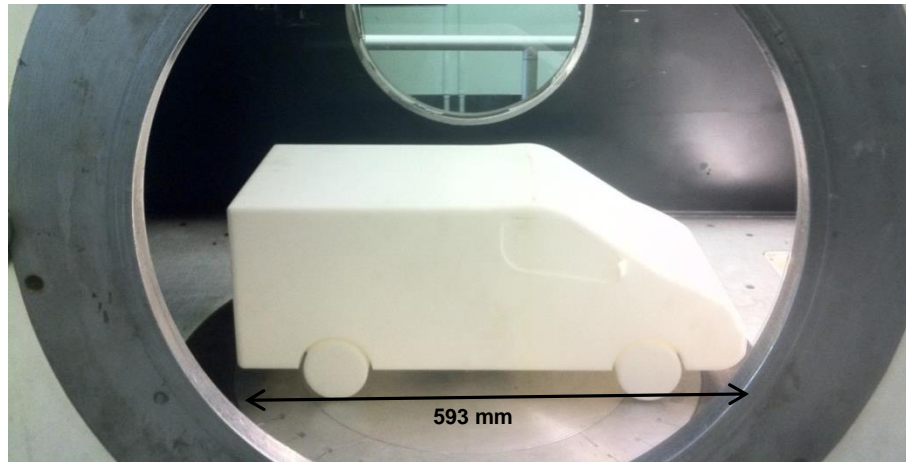


Figure 6.14 Model inside the wind tunnel

Boundary layer thickness of the wind tunnel was calculated as below:

Turbulence boundary layer thickness is defined by [81]:

$$\delta_x = 0.37 \left(\frac{U_\infty X}{\nu} \right)^{-\frac{1}{5}} \quad (6.4)$$

The front of the model is 0.852 m down the working section of the wind tunnel. Therefore:

$$\delta_x = 0.37 \left(\frac{40 \times 0.852}{20^{-6}} \right)^{-\frac{1}{5}} = 0.0178 \text{ m}$$

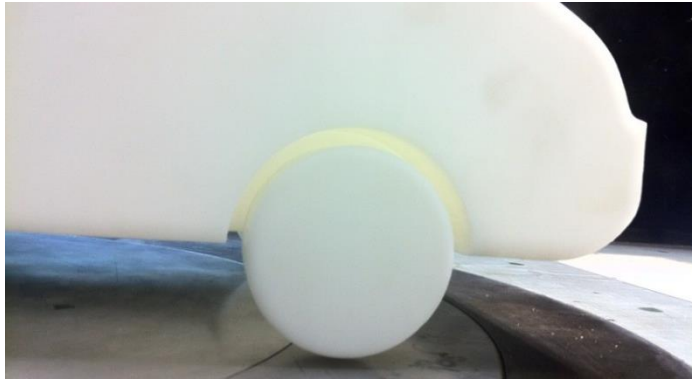


Figure 6.15 Model 3mm above the wind tunnel floor

The scale (force measurement) was connected to a computer which would record the readings (drag force). It was set to take 100 readings every 1 second for each experimental run. Calibration of the scale was carried out, by setting the reading to zero, before each experimental run to ensure that any drift in the output was minimized.

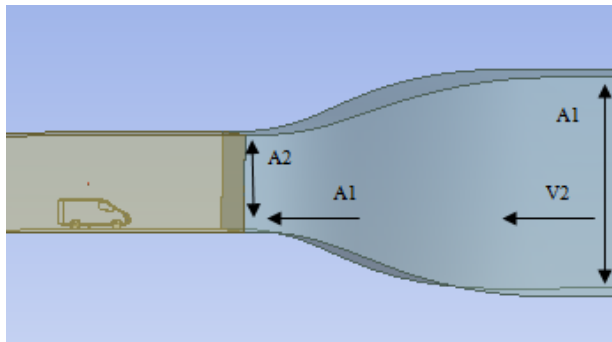


Figure 6.16 Wind tunnel contraction section

$$V_2 = \frac{\sqrt{\frac{2g}{\rho_{Air}}(P_1 - P_2)}}{\left(1 - \frac{A_2}{A_1}\right)} \quad (6.5)$$

$$T = 20^{\circ}$$

$$\rho = 1.22$$

$$V_2 = 4.11 \sqrt{(P_1 - P_2)}$$

6.5. Experimental Results

The experiment was done for four different velocities which would give the following Reynolds numbers based on the characteristic length of 0.6m which is the

length of the vehicle. This is equivalent to $1/8^{\text{th}}$ of the Reynolds number typically associated with the real, full scale Vauxhall Vivaro van, see dimensions in Figure 6.17:

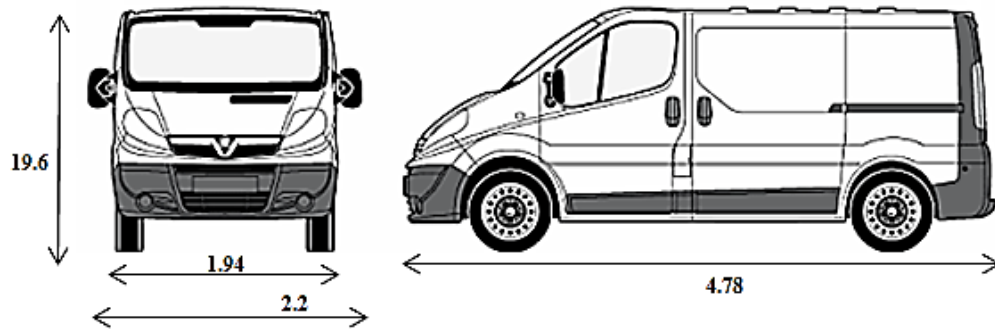


Figure 6.17 Dimensions of Vauxhall Vivaro [113]

The free stream turbulent intensity was measured to be 0.5% and this value was employed in CFD comparisons. No wind tunnel correction formula was employed since the subsequent CFD analysis include the geometry of the wind tunnel and the same velocities, were used.

(P_1-P_2) (mmHG)	V (m/s)	R_e
10	13	528666.6
25	20.55	835700.0
30	22.51	915406.6
42	26.64	1083360.0

Table 6.1 Different velocities with the corresponding Reynolds numbers

Drag force was measured for all three models (Figures 6.10, 6.11 and 6.12) for above velocities. For each case 100 readings were recorded by computer with an interval of 1 second. Figure 6.18 gives examples of 100 readings for velocity 26.64 m/s. The standard deviations of the 100 drag force measurements were measured and it only varies between 0.094 and 0.108 m/s which is small comparing to the actual drag force values which are in the range of 9 to 13 N.

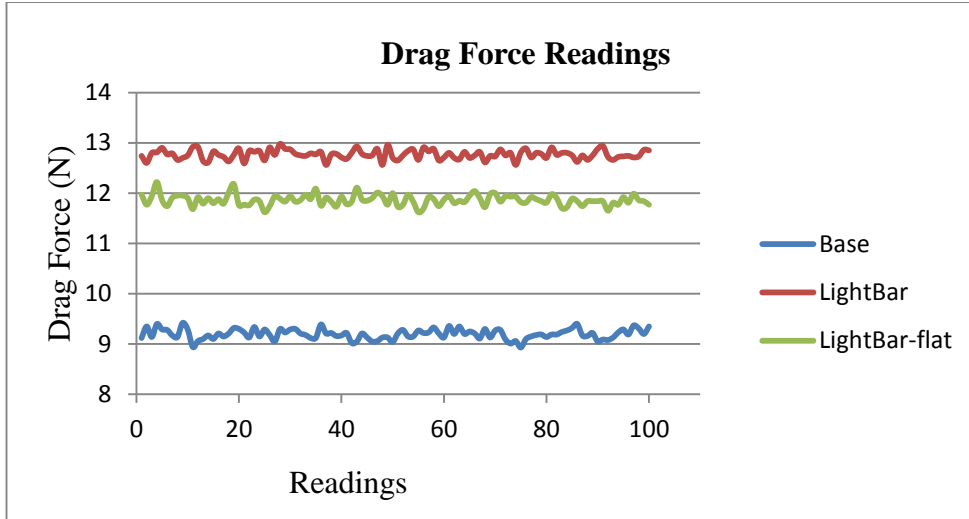


Figure 6.18 Drag force for 100 readings for 26.64 m/s

Average drag force and also drag coefficient were calculated for all four velocities and are presented below:

Model	Average Drag Force (N)	Drag Increase (%)	C _D	C _D Increase (%)
Base	2.46	0.346
Light-bar	3.26	32.0	0.436	26
Light-bar-Flat	3.08	25.0	0.412	19

Table 6.2 Average drag force for all models for 13 m/s

Model	Average Drag Force (N)	Drag Increase (%)	C _D	C _D Increase (%)
Base	5.67	0.319
Light-bar	7.82	37	0.418	31
Light-bar-Flat	7.29	28	0.390	22

Table 6.3 Average drag force for all models for 20.55 m/s

Model	Average Drag Force (N)	Drag Increase (%)	C _D	C _D Increase (%)
Base	6.76	0.317
Light-bar	9.27	37	0.413	30
Light-bar-Flat	8.65	27	0.386	21

Table 6.4 Average drag force for all models for 22.51 m/s

Model	Average Drag Force (N)	Drag Increase (%)	C_D	C_D Increase
Base	9.19	0.308
Light-bar	12.76	38	0.406	32
Light-bar-Flat	11.86	29	0.337	22

Table 6.5 Average drag force for all models for 26.64 m/s

The tables above demonstrate that the drag increase stays in the same range for all velocities apart from 13 m/s which would probably be due to the fact that the Reynolds number ($Re = 475800$) is low for this particular case compared to other cases and flow did not manage to catch the effects of the add-ons well. Figure 6.19 shows that the trend of the drag force is consistent for all four different velocities and the maximum and minimum velocities belong to the vehicle with original light-bars and the base model respectively. Least drag force belongs to the optimised light-bar amongst all the models with add-ons. As it is expected it also shows the drag force increases with the increase in the velocity and the lowest velocity of 13 m/s has the lowest drag force.

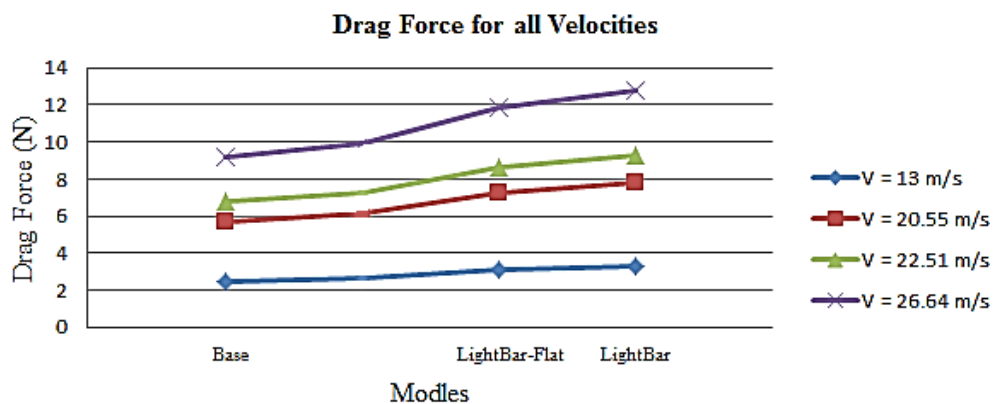


Figure 6.19 Drag force for all velocities for four models

Figure 6.20 shows the relationship between the drag coefficients with different velocities for all models. As it can be seen, the drag coefficient remains almost in the same regions for the same model with different velocities. The reason for the slight difference could be the sensitivity of the measurement machine for measuring the force which may not have functioned well for lower velocities and have been more precise for higher velocities. C_D is the indication of how aerodynamic is an object, it is non-dimensional form of the drag force as expected not to change with the variation in the velocity.

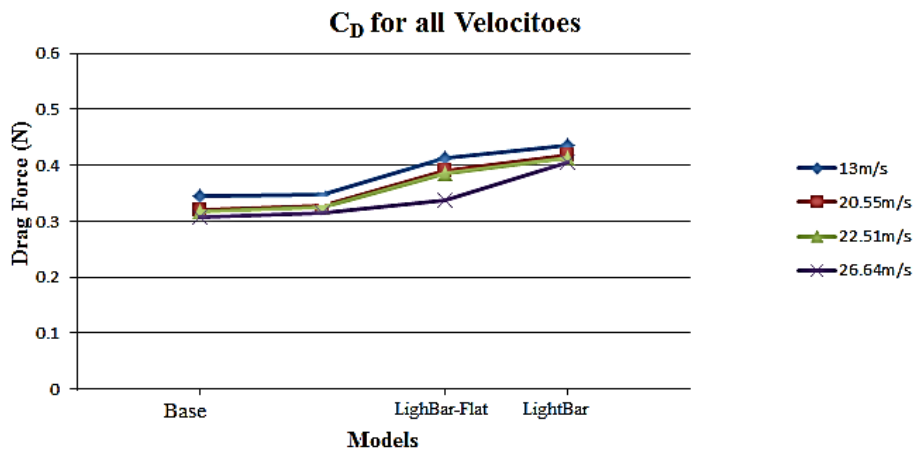


Figure 6.20 Drag Coefficient for all velocities for four models

6.5.1. Flow Visualisation

Flow visualisation was used in order to see the effects of the add-ons on the flow field and how the optimum configuration modifies the flow behaviour around the vehicle. Smoke visualisation can only be used in open wind tunnels as smoke has to exit the wind tunnel in order that the flow stays clear. The wind tunnel used at Queen Mary University of London was a closed circuit one and the only practicable way to visualize the flow is, by using tufts. Small tufts of wool were attached to the area of interest on the vehicle and the behaviour of the flow was observed. Figure 6.21 shows the flow visualisation for the baseline model for the velocity of 26.64 m/s. A small flow disturbance can be seen on the rear of the vehicle and that can be assumed is as a results of separation and circulation; but the flow remains streamline on the top of the vehicle.



Figure 6.21 Flow visualisation using tufts for baseline model

As it is demonstrated on Figures 6.22 and 6.23, the flow is completely disturbed on the top and the rear of the vehicle with the light-bar which causes the drag force to increase as much as 37%. Immediate separation and recirculation can be seen after the front light-bar. There is also increase in the flow separation on the rear which is the main cause of the increase in drag force.



Figure 6.22 Flow visualisation using tufts for model with light-bars (rear view)



Figure 6.23 Flow visualisation using tufts for model with light-bars (top view)

6.6. CFD Validations

The data produced by the experiment, will now be used to assess the accuracy of the CFD simulations. An important first step was to generate an accurate reproduction of the column of air which is contained within the tunnel walls. Physical measurements of the scale model, the working section and the extension of the wind tunnel to the inlet and the outlet formed the basis of the CAD model, see Figure 6.24. Since attention is restricted to steady-state solution of symmetric flow at zero yaw, a symmetry plane was introduced to reduce the computational effort.

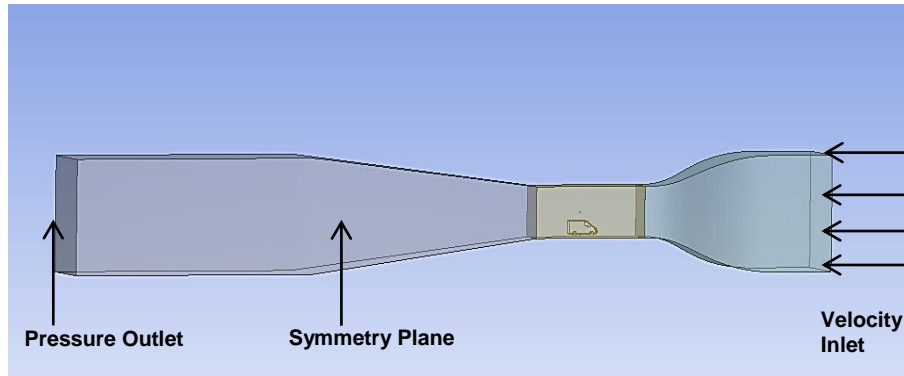


Figure 6.24 Computational geometry of the wind tunnel domain including boundary conditions

The geometry was constructed above the floor of the wind tunnel, see Fig. 6.25 in addition to the symmetry plane, velocity and pressure outlet were employed with wall type boundary conditions on all remaining surfaces.

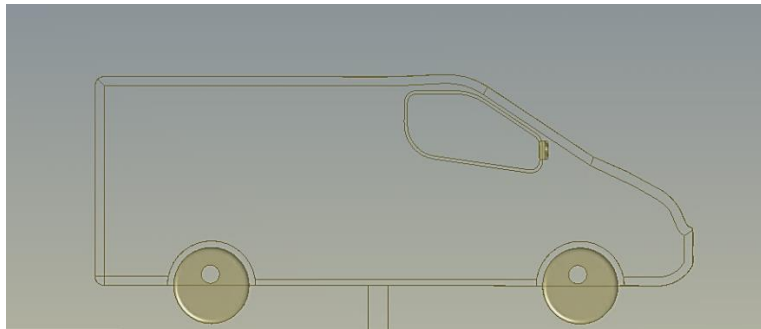


Figure 6.25 Geometry of the vehicle inside the wind tunnel above the floor

Each domain was decomposed into a series of zones which permitted appropriate cell types to be used in various regions. A fully block structured grid (hexahedral cells) would be ideal as it would decrease the computational effort, however this proved too difficult to implement because of complication arising from the smaller features of the vehicle. Thus, a hex-tet grid combined the clear advantages of structured cells with the flexibility of unstructured ones. This strategy allowed the majority of the air volume to be discretised using structured elements, see Fig. 5.8 in addition, the upstream and downstream section were meshed with line controls, thereby stretching the grid longitudinally such that the cell density increased immediately ahead of and behind the vehicle, see Fig. 6.26.

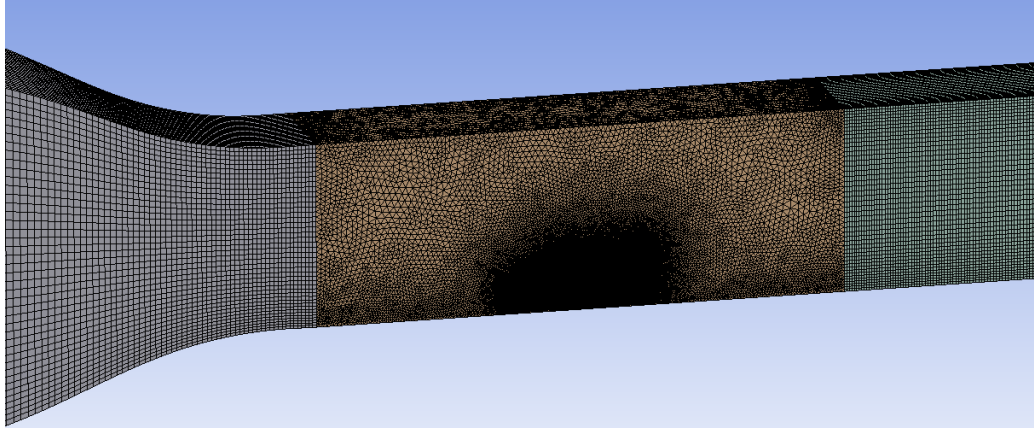


Figure 6.26 Illustration showing the grid on the symmetry plane and top wall

A region of relatively fine hex cells was placed above the model vehicles. The grid in remaining fluid volume was constructed by firstly applying a fine 2-D triangular grid to the surfaces of the vehicle before constructing an unstructured volume grid, see Fig 6.27.

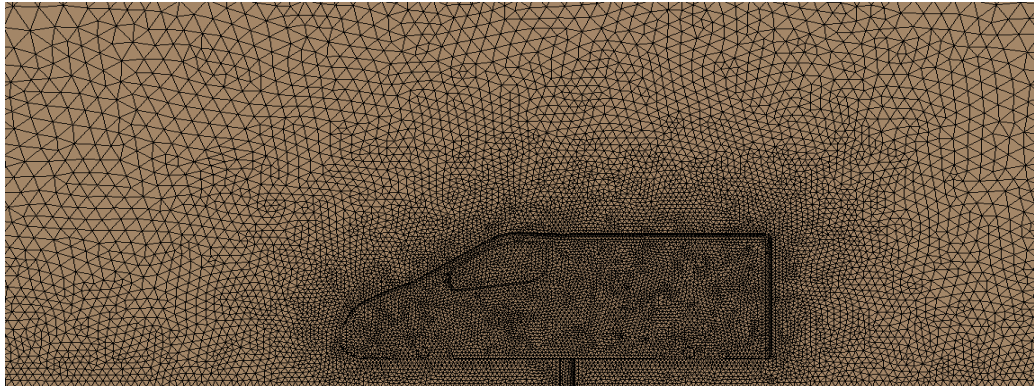


Figure 6.27 Illustration showing the grid around the vehicle

6.6.1. Inlet and outlet sensitivity

The length of the domain in terms of where to place the inlet and outlet can have an important effect on the flow. Inlet boundary condition is prescribed with the free stream velocity and the turbulent intensity. It is important to ensure that the airflow fully develops before and after the vehicle. To ensure this, the length of the inlet and outlet were extended, giving the solution domain length, $L = 26\text{m}$.

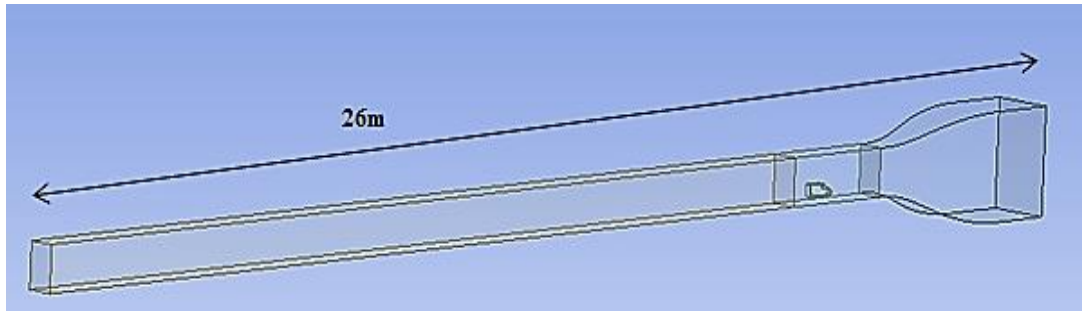


Figure 6.28 Solution domain dimensions with extended inlet and outlet

6.6.2. Grid Independence Study

A mesh dependency study was carried out on the baseline model to assess the dependency of the CFD results on the mesh size used to mesh the domain and in particular the area surrounding the vehicle. The above method of producing unstructured grids around the vehicle was repeated, producing 3 different grid sizes with the global cell count increasing from 4 – 8.5 millions. This was achieved by refining the surface mesh on the vehicles from 5 to 3 mm. Second order steady-state simulations were conducted for each grid using SIMPLE algorithm and S-A turbulence model was used. Solution for drag force was computed as a function of the cell count, see Figure 6.29. Despite this grid dependence, the densest grid was the maximum possible with the computational resources available at the time of the computations and so further refinements could not be made. This study indicates the relative independency of the results from the mesh density and shows as the mesh grid density changes that the drag force only varies for 1 to 2%. In particular, the mesh density used throughout the optimisation is a compromise between computational time and the solution accuracy.

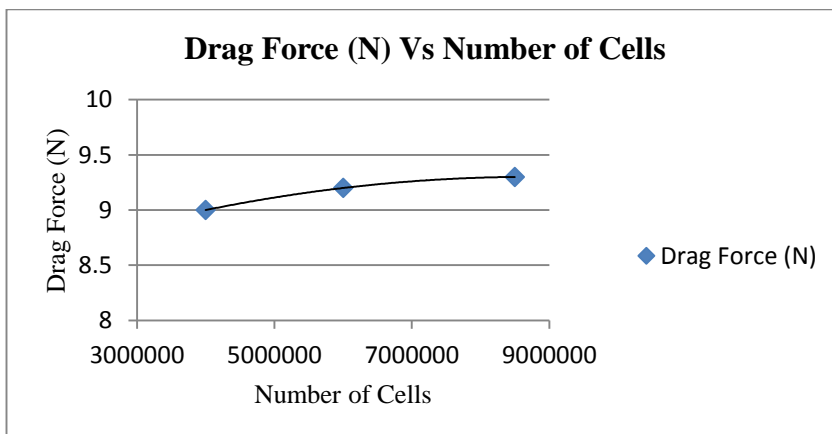


Figure 6.29 Drag force vs number of cells

6.6.3. Y^+ analysis

Since all of the solutions were obtained using standard wall functions, it was necessary to check that the wall y^+ values adjacent to the surfaces of the vehicle were in the correct range. Figure 5.35 shows contours of wall y^+ generated by S-A turbulence models. It is recommended that wall y^+ values should be in the range of 30-500 [114]. The main factor influencing y^+ is the near-wall grid spacing so as the grid is refined, y^+ will reduce accordingly. From Figure 6.30 it is evident that the y^+ value is less than 100 (average 43) around the vehicle for the fine mesh and average of 65 for the medium mesh size. The values lie within the recommended range of 30-500. The average value of y^+ on the surface of the vehicle increases from 43 to 65 as the mesh size increases from fine to medium. The increase in the y^+ value is expected since the distance of the first node increases for the medium mesh size. For both cases, the values are still within the acceptable range as it was mentioned above.

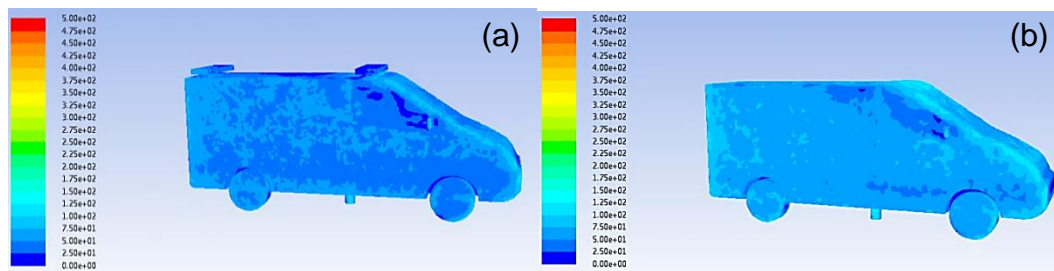


Figure 6.30 Contour of y^+ value for S-A turbulence model for a) fine mesh, b) medium mesh

6.6.4. Turbulence Model Performance

- Baseline model

Simulations were conducted for four turbulence models, namely : S – A, K – ϵ (Standard), K – ϵ (Realisable) and K – ω for baseline model. The motivation for selecting these turbulence models was to observe how S-A model is compared with the KE (Standard) together with more advanced KE (Realisable) and K – ω . Solutions for all four were compared with the experimental drag force values of the vehicle. All the simulations were conducted with three different grid size of coarse, medium and fine. Results are presented in table 6.6:

	Drag Force (N)				Experiment
	S – A	K – ϵ (S)	K – ϵ (Re)	K – ω	
Fine (8500000 cells)	9.0	15.2	8.1	10.4	9.2
Medium (6000000 cells)	9.2	15.0	8.2	12.2	9.2
Coarse (4500000 cells)	9.3	16.2	8.5	12.0	9.2

Table 6.6 Drag force results of the mesh grid size and turbulent models comparison for baseline model for 26m/s

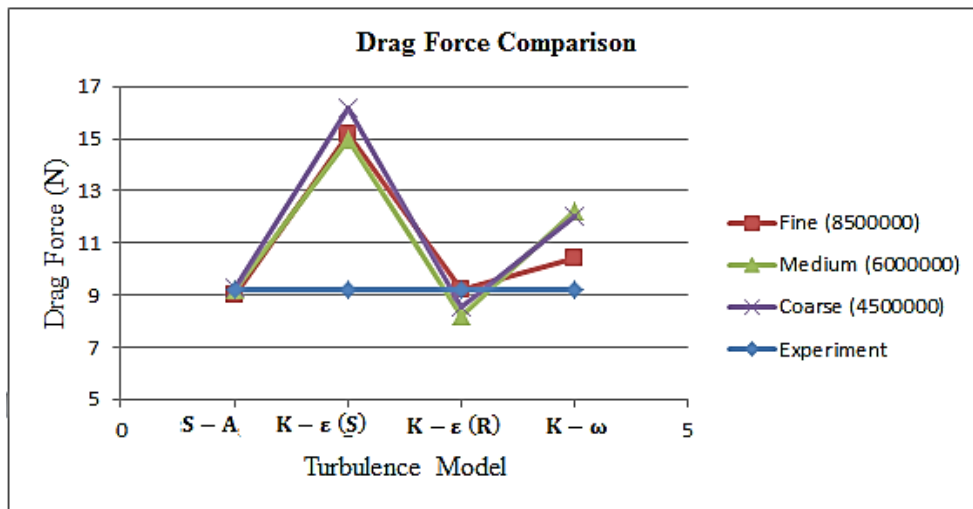


Figure 6.31 Turbulence and mesh grid density comparison with the experiment for the Baseline model

Here, the S – A and K – ϵ (Realisable) clearly match the experimental drag force value (9.19), though less accurate, K – ϵ (Standard) and K – ω models are also in reasonable agreement with the experimental drag force value. It would appear from Table 5.36 that the S – A exhibits superior performance compared with the other turbulence models. Thus S – A and K – ϵ (Realisable) turbulent models are the best at predicting drag force of the four types of turbulence models considered. Due to the fact that S – A only uses one transport equation and it is faster and therefore cheaper, this turbulent model is considered to be the most suitable one for use on the optimisation studies.

- Models with Light-bars

Another set of simulations were conducted for two different grid sizes, fine and medium. Similar four turbulent models were used again this time for baseline model,

models with add-ons as well as the optimised configurations. The results for the drag force and coefficients are presented in tables 6.7 and 6.8.

	Drag Force (N)			C_D		
	Baseline	Light-bar	Light-bar-flat	Baseline	Light-bar	Light-bar-flat
S – A	9.0	13.47	12.32	0.305	0.450	0.412
K – ϵ (Re)	8.10	12.68	11.60	0.270	0.420	0.388
K – ϵ (S)	15.2	19.46	18.70	0.500	0.640	0.625
K – ω	10.40	16.32	15.74	0.350	0.540	0.526
Experiment	9.19	12.76	11.86	0.308	0.406	0.377

Table 6.7 Comparison of the drag force and coefficients of the fine mesh density for different turbulent models for all models with add-ons for 26m/s.

	Drag Force (N)			C_D		
	Baseline	Light-bar	Light-bar-flat	Baseline	Light-bar	Light-bar-flat
S – A	9.20	13.90	12.78	0.312	0.466	0.427
K – ϵ (Re)	8.20	12.85	11.94	0.275	0.429	0.399
K – ϵ (S)	15.0	19.56	18.86	0.500	0.650	0.635
K – ω	12.20	16.52	15.44	0.410	0.560	0.510
Experiment	9.19	12.76	11.86	0.308	0.406	0.377

Table 6.8 Comparison of the drag force results of the medium mesh density for different turbulent models for all models with add-ons for 26 m/s.

From Figures 6.32 and 6.33, it can be seen that S – A and K – ϵ (Realisable) almost match the experimental values for all four different models. K – ϵ (Standard) and K – ω are not as good agreement as the previous mentioned models. Therefore as it was mentioned before, it can be concluded that S – A is the most suitable turbulence model to predict the drag force of the vehicle and assess its aerodynamics characters.

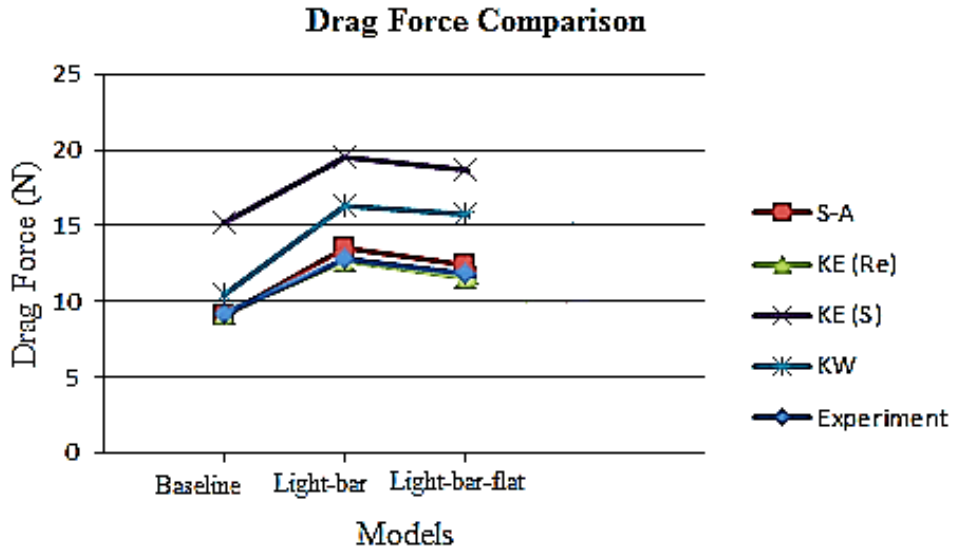


Figure 6.32 Drag force comparison for the medium mesh density for different turbulent models for all models with add-ons

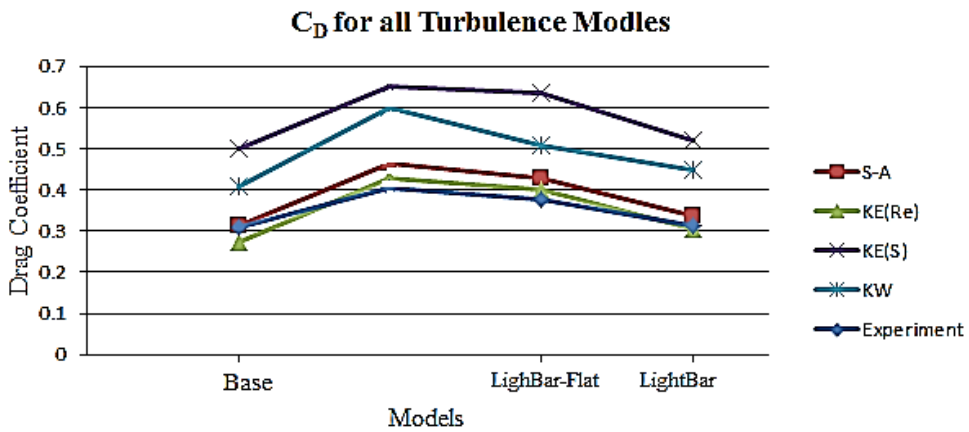


Figure 6.33 Drag coefficients comparison for the medium mesh density for different turbulent models for all models with add-ons

	Experimental C_D	Difference %
Baseline	0.308
Light-bar	0.406	32
Light-bar-flat	0.377	22

Table 6.9 Comparison of the experimental drag coefficient

Table 6.10 contains the experimental drag coefficient for 26.64 m/s. the drag coefficient increase by 32% by adding the light-bars similar to the drag force increase. It can be seen that there is only slight increase in the value of drag

coefficient for optimised model comparing to the base model. The drag coefficient increase by adding the add-ons, reduces from 32% to 2.2% by means of CFD optimisation.

6.6.5. CFD Simulation Flow Behaviour

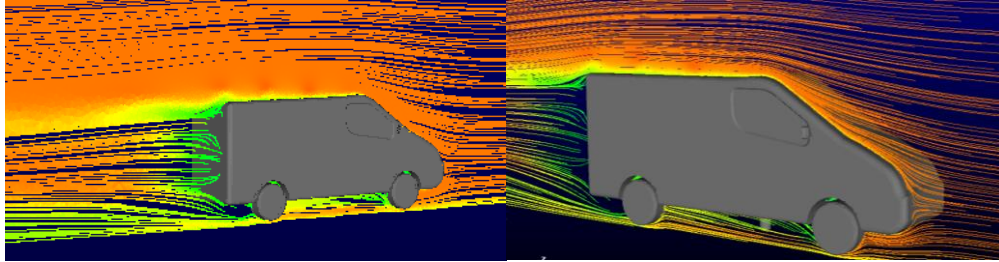


Figure 6.34 Behaviour of the flow in front and rear of the baseline model

Streamlines on the Figure 6.34, shows the path that flow takes to move around the vehicle. It can be seen that the flow moves around the baseline model smoothly and there is region of separation on the rear.

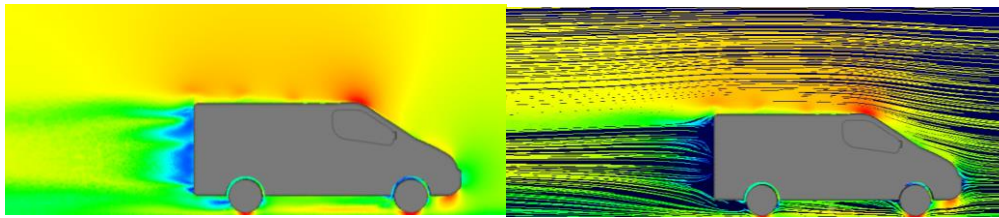


Figure 6.35 Velocity contour and streamline of the baseline model

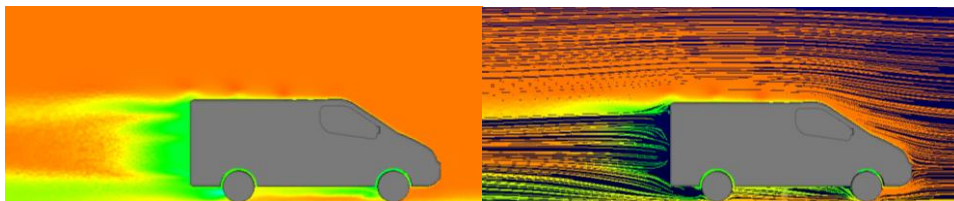


Figure 6.36 Pressure contour and streamline of the baseline model

Behaviour of the flow around the baseline is shown on Figures 6.35 and 6.36. Similar to the experimental flow visualisation (Figure 6.21), flow stays attached on the top and low pressure due to separation and circulations is experienced on the rear.

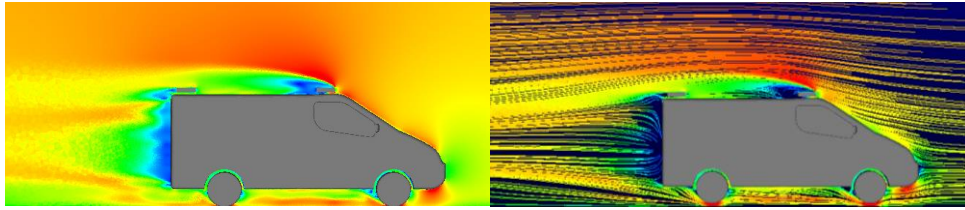


Figure 6.37 Velocity contour and streamline of the model with light-bars

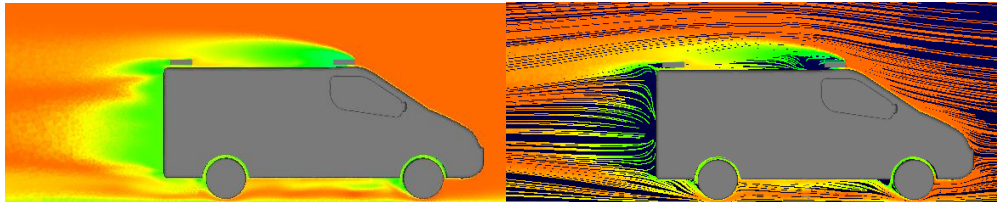


Figure 6.38 Pressure contour and streamline of the model with light-bars

Figures 6.37 and 6.38 shows the velocity and pressure contours and streamlines for the model with light-bars. Similar to the experimental results and the flow visualisation in the wind tunnel (Figures 6.22 and 6.23), the flow separation and region in low pressure can be seen immediately after the front light-bar. Rear light-bar also makes the circulation and separation region to increase as it was also shown in the experimental flow visualisation Figures 6.22 and 6.23.

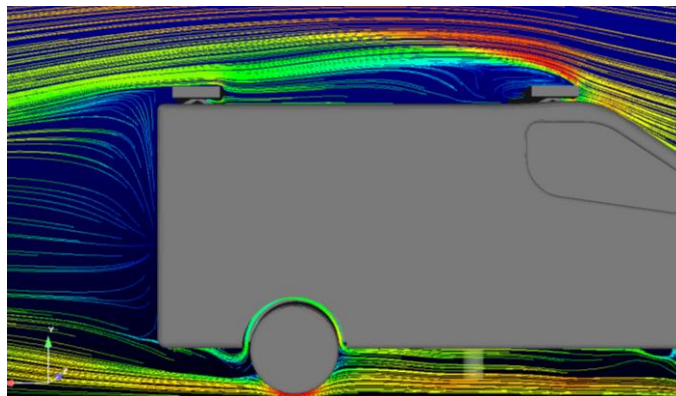


Figure 6.39 Closed view of the velocity contour around the light-bar and rear of the vehicle

Closed up view of the behaviour of the flow around the light-bars and how the flow is disturbed is shown on Figure 6.40. Likewise the experimental flow visualisation, the region of flow separation after the light-bars is evident. Blue streamline indicate the region of low pressure which are due to the separation of the flow from the vehicles body on the top and the rear. Figures 6.40 and 6.41 show the velocity and

pressure contours for the modified flat light-bars. It shows the reduction in separation and low pressure area on after the front light-bar and on the rear.

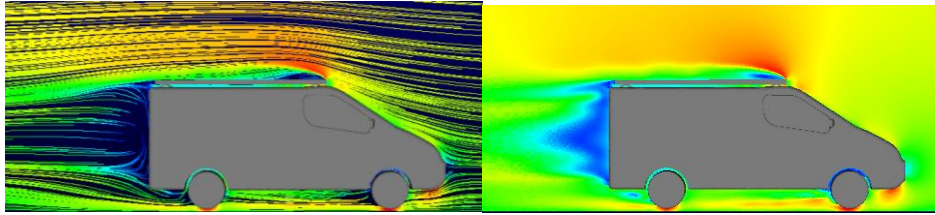


Figure 6.40 Velocity contour and streamline of the model with light-bars flat

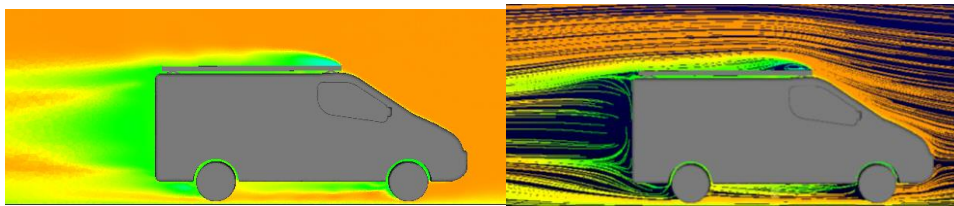


Figure 6.41 Pressure contour and streamline of the model with light-bars flat

Closed up view on Figure 6.42 also shows the small area of the circulation of the top front of the modified light-bar.

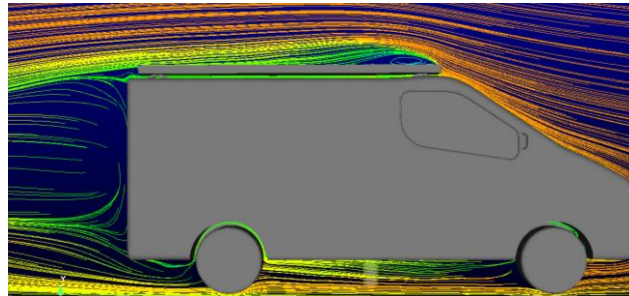


Figure 6.42 Close view of the velocity contour around the light-bar flat and rear of the vehicle

6.7. Conclusion

The wind tunnel experiments and the CFD simulations show very good agreement in terms of flow behaviour around the vehicle and the drag force measurements. Tables 5.7, 5.8 and 5.9 shows that the drag force measurement by CFD simulations with $S-A$ and $K-\epsilon$ realisable give very close drag force results very close to the experimental results. Comparing Figures 6.34 to 6.42 from CFD simulations with

the Figure 6.21 to 6.23 from experimental flow visualisation also shows very good agreement and the regions of low pressure and separations have been outlined by both methods and they give consistent results. In summary the flow field from the CFD results are consistent with the experimental flow visualisations. It can therefore be concluded that CFD simulation can be used in order to measure the aerodynamic characters of the vehicles such as drag force and the flow behaviour can also be assessed by means of CFD simulations. This enables aerodynamic optimisation to be carried out effectively using CFD.

7. Design Optimisation of Emergency Response Vehicle

The aerodynamic and optimisation analyses carried out in previous chapter are now extended in order to undertake a formal optimisation study of trailer design. Coupling the CFD methodology outlined in previous chapters with optimisation techniques in search of the best design offers potentially huge benefits. The focus, therefore, of this chapter is on the formulation of an optimisation problem followed by three studies aimed at reducing drag force of Emergency Response Vehicle. The model used in these studies will be a van-conversion ambulance (Figure 7.1), van-conversion Police (Figure 7.2) and a sedan Police car (BMW 5series) (Figure 7.3).



Figure 7.1 Side view of a Fiat ambulance (courtesy of P. Occardi)



Figure 7.2 Side view of a Vauxhall Police van [89]



Figure 7.3 BMW Police car [13]

7.1. Problem Formulation

The bluff nature of current, commercially available Emergency Response Vehicles induce highly separated flows and significant levels of form drag. However, recent substantial increases in fuel prices have brought the need for minimal aerodynamic drag into much sharper focus [6, 17]. Applying aerodynamic shape optimisation to modify the design of Emergency Response Vehicles has the potential to significantly reduce drag and hence fuel consumption. Such a strategy should, of course, ensure that any proposed design changes do not adversely compromise the purpose and effectiveness of such vehicles. The following section discusses the considerations in formulating the optimisation problems.

7.1.1. Objective function and Parameterisation

Identifying an optimum design involves a number of steps. Results from the baseline configuration with light-bars (i.e. the standard Ambulance or Police vehicle case), show that almost 30% of the vehicle drag is attributable to the added light-bars alone. Therefore focusing on modification of the shape of the light-bars in order to make them aerodynamic seems reasonable. With these considerations in mind two different parameterisation techniques were proposed with two and three design variables for different models which will be discussed in the following.

7.2. Ambulance Van-conversion

The following study focuses on the aerodynamic design optimisation of a specific type of light truck, namely emergency response vehicles for providing patient transport to hospital (generally referred to as *ambulances*), that have not been considered previously nor reported in the literature. This part consists of a formal

optimisation of the aerodynamic design of van-conversion ambulance, typically encountered within the United Kingdom. The benefits of employing an airfoil-based roof design which minimizes the deleterious aerodynamic effects of the required front and rear light-bars is investigated using a formal optimisation study based on Computational Fluid Dynamics (CFD), Optimal Latin Hypercube (OLH) Design of Experiments (DoEs) and the Multipoint Approximation Method (MAM), (refer to chapter 5.6.2). The roof is parameterized in terms of three design variables which represent a roof airfoil's size and orientation and the extent of the rear light-bar. Optimisation is done on the generic van-type ambulance conversion design and the results are then implemented on a practical Fiat (Ducato) van chassis (Figure 1) to see the effectiveness of the optimisation on the real model. In practice, due to a range of existing regulations, the shape of ambulances cannot be changed radically due to constraints on features such as the maximum vehicle height and the minimum vehicle height at the rear in order to provide adequate access to the vehicle. An additional complicating feature for aerodynamic design optimisation of ambulances is the need for warning lights at the front and rear of the roof. These require a flexible shape parameterisation scheme with appropriate bound constraints on the associated design variables.

This research is focused on aerodynamic drag reduction based on shape optimisation of an ambulance's roof. Other parts of the vehicle (e.g. the lower surface, underbody features) were not considered in the present study. The computational procedure involves a sequence of CFD simulations for the drag estimation automatically controlled by the optimiser. The latter is based on the Multipoint Approximation Method (MAM) optimisation technique (refer to chapter 5.6.2) [101] which is very efficient when dealing with noisy analysis responses. The roof is parameterized using three design variables that represent a new design based on an airfoil (symmetric) profile concept. The optimisation is first performed on a generic (simplified) model of an ambulance, before the optimal design concept (pattern) for the minimal drag is applied to a more realistic model based on the Fiat van chassis (Ducato), see Figure 7.1. Finally, the effect of the obtained drag reduction for the Fiat ambulance on its overall fuel consumption is predicted using a simplified ambulance duty cycle.

7.2.1. CFD Optimisation Methodology

The CFD-based optimisation methodology was developed by considering a simplified, generic ambulance design. Van type chassis are of increasing interest for

ambulance conversions since they are lighter and more aerodynamic than conventional box-body vehicles, which are essentially small trucks with box trailers placed at the rear. The main steps of the optimisation methodology are described below.

7.2.2. CFD Modelling

The geometry of the generic model is shown in Figure 7.4 and was based on a typical Mercedes Sprinter ambulance conversion used by the YAST. In order to reduce computational costs, symmetrical, only zero yaw angle air flow cases are considered, enabling the flow domain to be reduced by half. The symmetric flow simulation domain has a semi-elliptical cross section surrounding the vehicle whose height (18.5 m), width (22.5 m) and length (85.5 m) are sufficiently large to minimize any flow blockage effects and to adequately capture turbulent flow behind the vehicle.

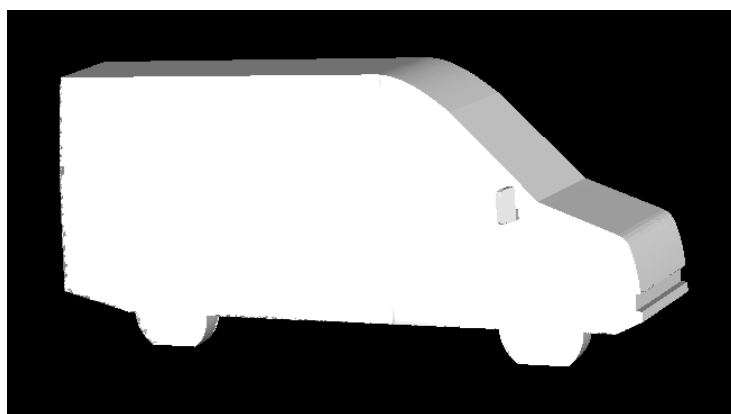


Figure 7.4 Generic model of van-type vehicle

Prior to meshing, the domain was decomposed into 6 zones (volumes) to apply different discretization schemes. The volume immediately surrounding the vehicle was discretized by tetrahedral elements, in order to represent the complex of vehicle geometry, with element refinement towards the vehicle surface. Other volumes were meshed using structured elements, see Figure 7.5 and 7.6. In practice, the mesh density used throughout the optimisation is a compromise between computation time (as many CFD analyses will be required during the optimisation process) and the simulation accuracy. In this example, the generated mesh contains around 2 million of elements with a cell size of 4 cm on the vehicle surface.

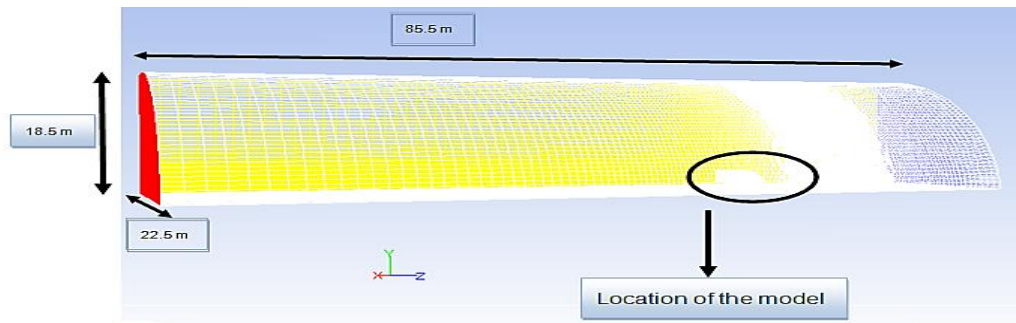


Figure 7.5 Wind tunnel domain and its dimensions

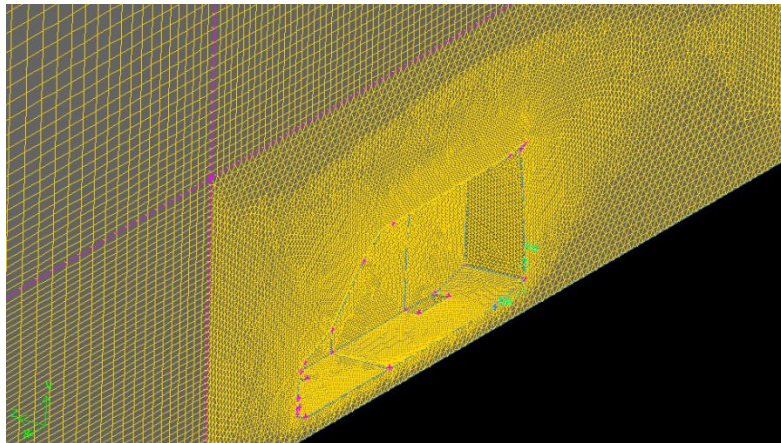


Figure 7.6 Mesh structure surrounding the vehicle

Since several previous studies have shown that the two equation $k - \varepsilon$ turbulence model can successfully simulate exterior airflows past vehicles with dimensions similar to ambulance geometries, see e.g. [8, 10, 11, 30], this model is also used here to model air flows past ambulances. Comparison with aerodynamic drag data provided by Kinetic Special Vehicles for box body conversions showed that the CFD modelling carried out here typically predicts drag to within 2.5% of experimental values.

7.2.3. Boundary Conditions

At the inlet flow boundary a uniform horizontal velocity of 26.8 m/s (60 mph) was prescribed, while at the outlet an atmospheric pressure condition was specified. The same velocity was set for the moving ground and rotational, moving boundary conditions were imposed on the wheels. On the surface of the vehicle, no-slip wall boundary conditions were specified. The boundary conditions are summarised in Table 7.1.

Boundary	Boundary type	Parameters
Inlet	Velocity	26.8 m/s
Outlet	Pressure	0 Pa
Road	Moving wall	26.8 m/s
Tyres	Rotating wall	70.5 rpm
Vehicle surface	Stationary wall	No slip
Domain top	Stationary wall	Zero shear stress

Table 7.1 Boundary conditions applied for the generic ambulance model

7.2.4. Ambulance Conversion Schemes

Two typical ambulance conversion schemes that are widely used in emergency response fleets (e.g. in the YAST) are illustrated in Fig 7.7. The first design represents an ambulance with detached front and rear lights bars, while the second design represents an ambulance with the lights integrated under the vehicle's roof. It is worth noting here that these ambulance conversions always increase the aerodynamic drag since the addition of the lights leads to an increase in the effective projected area.

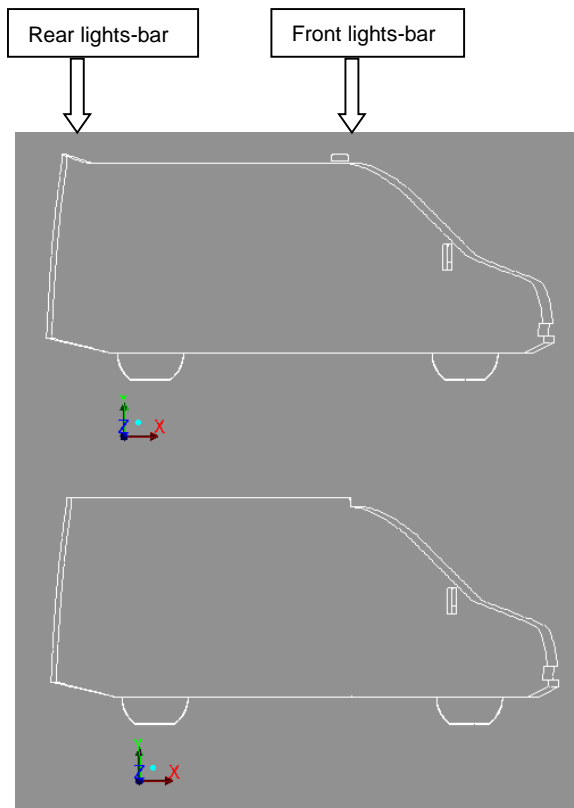


Figure 7.7 Conversion schemes for a generic ambulance model: with detached rear (Conversion A, top picture) and front lights bars and with the integrated (under the roof) lights (Conversion B, bottom picture)

CFD analysis of Conversion scheme A (Figure 7.7, top picture) applied to the generic model with the maximum height of the light bars equal to 10cm, predicted that this increases drag by 12.1%, whereas the second conversion (B) with the integrated lights bars (Figure 7.7, bottom picture) is significantly more aerodynamically efficient since it increases the drag by only 6.2%. This can be explained by the fact that the detached front light bar is an obstacle for the oncoming flow, forcing it to change its direction abruptly. As a result, immediately after the front light bar, the flow separation takes place developing the area of low pressure. By integrating the front and rear bars, this area of flow separation is eliminated, thereby avoiding the associated aerodynamic drag.

7.2.5. Optimisation Problem Formulation

The key issue prior to carrying out design optimisation on the vehicle's roof is to choose an efficient parameterisation scheme for modifying its shape. In the optimisation process the parameterisation should be automated and provide consistent (feasible) geometries and meshes for the sequence of designs generated by the optimiser towards an optimum. As 3-dimensional CFD simulations are computationally expensive, it is very desirable that the parameterisation is based on a small set of design variables since adding design variables will increase optimisation time dramatically (this is known as “the curse” of dimensionality).

In the present work, the parameterisation is based on the tools provided by the commercial CFD software Fluent's Gambit which was used for importing geometry, modelling and mesh generation. The approach may be categorised as feature-based as it involves the creation of individual entities (volumes) that can be moved, rotated and subsequently intersected (subtracted) and/or united (merged) with each other. These entities have simple geometries which can be modified using a small number of feature sizes, such as length, height, thickness, etc. The particular geometry entities have been chosen in order to represent a potential (optimal) configuration of the roof of the generic van conversion that embeds the front and rear lights bars.

The first entity is a symmetric airfoil, which replaces the vehicle's flat roof. In our design concept, a front part of the airfoil (its thickest part next to the leading edge) represents the integrated front lights. The airfoil volume was created by sweeping a two-dimensional airfoil profile in the z-direction (a direction normal to a symmetry plane of the generic model). The sweep distance was chosen as 98.5% of the width of the van roof in front so that the designed front light bar was slightly narrower than

the roof width in front. The airfoil is a simple NACA (National Advisory Committee for Aeronautics) symmetric 4-digit profile [16] which is described by the following expression:

$$y = \left(f \times \left(0.2969 \times \sqrt{xc} \right) \right) - 0.1260 \times xc - 0.3516 \times (xc)^2 + 0.2843 \times (xc)^3 - 0.1036 \times (xc)^4 \quad (7.1)$$

where: c is the chord length of the airfoil $xc = x/c$ is a scaled position along the chord, f is the maximum thickness fraction (% of chord length) and y is the half thickness at a point xc . The airfoil profile contour (namely its upper symmetry edge) was generated using 1000 equally distributed points along the airfoil chord. The lower edge of the airfoil was obtained by simply reflecting the upper edge in respect to the airfoil chord. Finally, a face between two edges was created and swept to produce the airfoil entity (volume). The second entity is the rear light bar, which was generated by sweeping a triangular cross section (of length and height 10cm) in the z -direction. Using the Gambit journal script language, the newly created entities were moved to the location on the roof as shown in Figure 7.8 and then subsequently subtracted from the volume surrounding the generic model of the van.

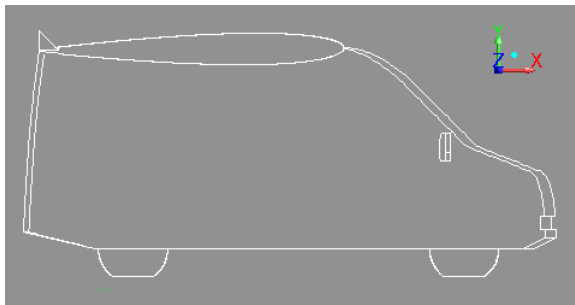


Figure 7.8 The generic ambulance model with the airfoil and light bar concepts.

The flow-chart of the geometry modelling is summarised in the following:

1. Create wind tunnel computational domain (geometry/mesh and boundary types) for the generic van
2. Execute Gambit by reading a journal script file that automatically performs the following steps:
 - a. read preliminary created model (wind tunnel domain)

- b. create individual entities (airfoil and rear light bar)
- c. move (rotate) entities
- d. subtract the entities from volume surrounding vehicle
- e. re-mesh the volume surrounding vehicle
- f. update boundary types
- g. save model in Fluent case (msh) format

It should be pointed out here that only the second phase is involved in the optimisation procedure. The first modelling stage is outside the optimisation loop and only has to be completed once, prior to the optimisation procedure. Note also that during the optimisation just one volume (that is adjacent to the vehicle surface) needs to be re-meshed while a mesh of the rest of the wind tunnel domain remains unchanged.

7.2.6. Definition of the Design Variables

Three design variables were used for shape optimisation of the vehicle roof, Figure 7.9. The first two design variables are linked to the width and orientation of the airfoil entity, namely its angle of attack x_1 (degree) and thickness fraction x_2 (% of the chord length as defined in Equation 6.1). The third design variable x_3 is the horizontal length of the triangular cross section representing the shape of the rear light bar.

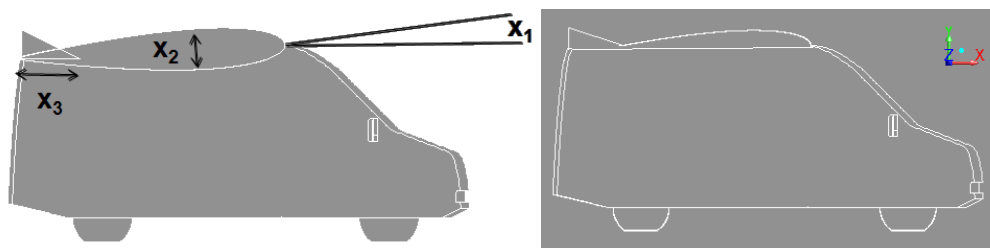


Figure 7.9 The parameterisation scheme used for shape optimisation of the ambulance roof

In order to meet regulations that the rear height of the ambulance should not be reduced, it is not changed during the optimisation. This constraint was imposed in the journal script file by removing any part of the rotated airfoil volume that recessed below the original flat roof. To illustrate the consequences of the airfoil rotation, roof configurations with $x_1 = -2$ and 2 degrees are shown in Figure 7.10.

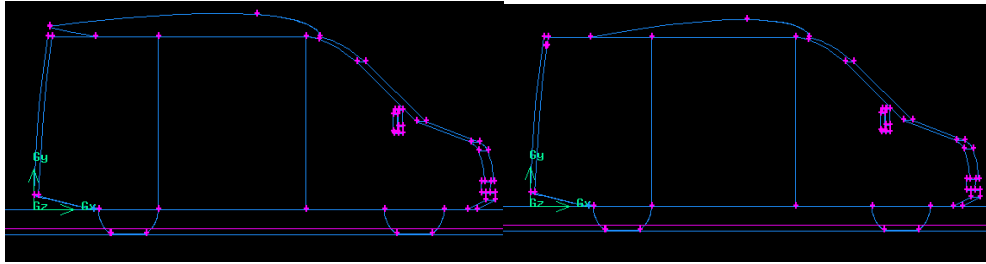


Figure 7.10 Ambulance roof shapes obtained with: (left) $x_1 = -2$ degrees and (right) $x_1 = 2$ degrees.

After preliminary consideration of a number of possible roof configurations generated by the vector $\mathbf{x} = (x_1, x_2 \text{ and } x_3)$, the boundary constraints on the design variables were assigned. These were chosen in order to: (i) prevent cardinal geometry altering (e.g. resulting in wrong topology and mesh failure) during optimisation and (ii) prevent the maximum height of an optimised roof being significantly higher than the original flat roof. The latter is also important in order to comply with ambulance size regulations. These constraints are given in Table 7.2.

Design variable	Lower bound	Upper bound
x_1 (deg)	-1.5	3.00
x_2 (m)	0.1	0.15
x_3 (m)	0.1	1.00

Table 7.2 Boundary constraints on the design variables

7.2.7. Optimisation Method

The objective function to be minimized is the aerodynamic drag force D (in Newton). Since D is proportional to the product of the vehicle projected area and the drag coefficient, this objective function represents a compromise between the size and aerodynamic performance of the vehicle. In the present study, the focus is on aerodynamic performance only and the influence of other important factors such as the rolling and acceleration resistances are not considered. The choice of an optimisation method depends on the problem formulation, the number of design variables, and a type of a response function. In present study, an unconstrained minimization problem with one objective function is considered involving three designs variables. Genetic Algorithms (GAs) or direct optimisation methods [149, 154] is used. An obstacle for the use of direct optimisation methods is that some

level of numerical noise may be contained in the objective function (drag) values that are derived from CFD computations [11]. In the present work Multipoint Approximation Method (MAM) has been used [147]. This method is based on a mid-range approximation framework that replaces the original optimisation problem by a succession of simpler mathematical programming problems. The functions in each iteration present high quality, noise free mid-range approximations to the corresponding original functions. The solution of an individual sub-problem becomes the starting point for the next step, which is repeated iteratively until the optimum is reached. MAM minimizes the number of expensive function evaluations and deals effectively with the numerical noise.

7.2.8. Optimisation Results

Since the parameterisation scheme may result in a non-unique solution, i.e. lead to an objective function with multiple optima, and in order to improve the likelihood of finding a global optimum, the optimisation problem has been solved using several restarts from different initial conditions. Two different designs were obtained after a number of the optimisation runs with corresponding design vectors $x_1=(0.71,0.12,0.85)$ and $x_2=(-1.5,0.12,0.85)$. The results are summarized in Table 7.3, which shows the drags calculated for the generic van (Figure 6.11) and its conversions with detached (Conversion A) and integrated (Conversion B) front and rear light bars.

Designs	Projected area (m ²)	Drag (N)
Van	2.87	599
Conversion A	2.98	672
Conversion B	2.98	636
Optimal 1	3.10	631
Optimal 2	3.09	617

Table 7.3 Drag comparison for the original and optimised designs

The profiles of the optimised designs (Optimal 1 and Optimal 2) are shown in Figure 7.11. A common feature of the optimal configurations is a trend to close the space (gap) between two entities (airfoil and rear light bar). This has been achieved in different ways.

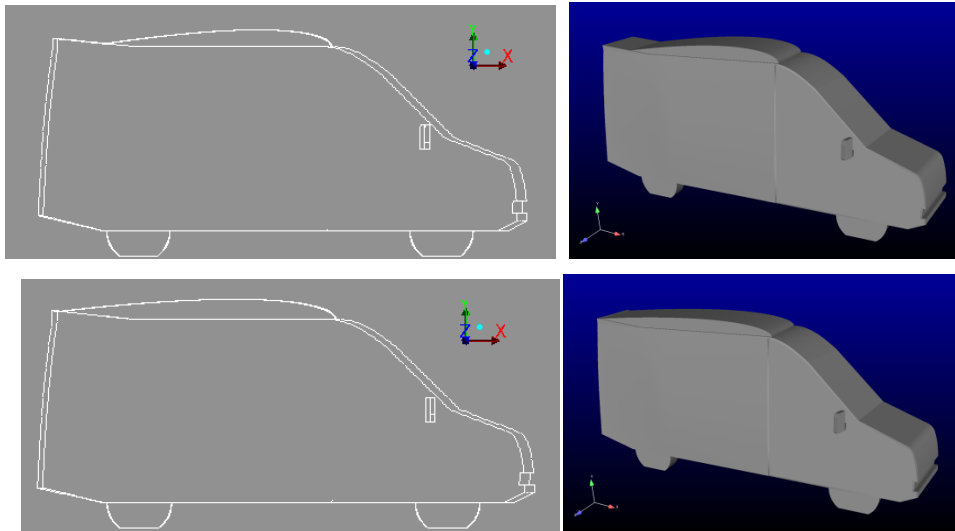


Figure 7.11 The profiles of optimised designs of the generic model: Optimal 1 (above) and Optimal 2 (below)

In the first case, the optimal configuration has been obtained by rotating the airfoil in a positive direction (i.e. recessing the profile deeper into the original flat roof) and simultaneously extending the length of the rear light bar. In the second case, the angle of attack is negative so the airfoil's trailing edge has approached the upper edge of the rear light bar. In this way the rear light bar has been completely integrated into the airfoil roof. (Note that in latter case, the impact of the third design variable x_3 on the objective is negligible). The second design has produced a better drag reduction. The corresponding improvement is 8.2% in comparison with Conversion A and 2.9% in comparison with Conversion B. Note that the restrictions on the design variables, to take account of practical constraints on the size of ambulances, limit the scope for achieving greater drag reductions. For example, reducing the vehicle height (and/or decreasing width) at the rear offers significant opportunities to achieve significantly larger reductions in aerodynamic drag [7].

7.2.9. Practical Application

In this section the optimisation concepts developed for the generic ambulance model are applied to a more realistic ambulance based on a Fiat (Ducato) van chassis, see Figure 7.1, and important practical aspects of carrying out the optimisation within industry are highlighted. In the present study this was done using Fluent's Gambit . Figure 7.12 also shows a preliminary mesh that was generated on several panels after repairing the geometry.

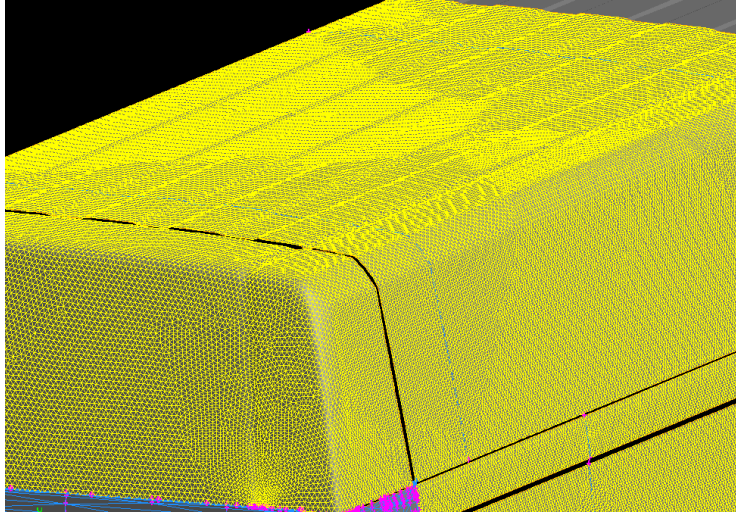


Figure 7.12 Examples of CAD model geometry

A computational domain (the wind tunnel) and CFD mesh of the Fiat van were built using the schemes which had been previously used in the generic van modelling. The CFD analysis was performed based on the realisable $k-\varepsilon$ turbulence model with a dense mesh containing approximately 6.5 million elements that results in a typical cell size of 1.5cm on the van surface. Although up to 10,000 iterations were allowed, convergence was typically obtained after 4000 iterations.

7.2.10. New Roof Design and Aerodynamic Performance

Figure 7.13 compares the CFD model of a Fiat van conversion with a real-life example, showing the front and rear light bars.

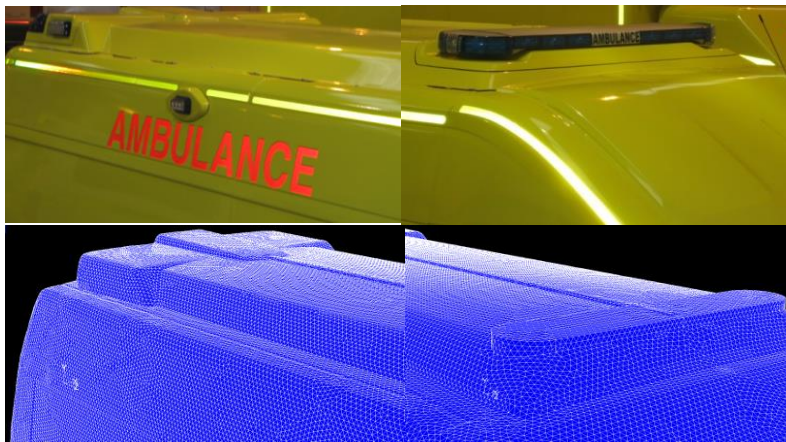


Figure 7.13 Rear and front light-bars of the Fiat ambulance: actual (above) and CFD model (below).

A new roof design incorporating the optimal design concept developed for the generic van conversion (Optimal 2) has been implemented for the Fiat ambulance conversion. In order to minimize manufacturing effort in implementing any design changes, the rear light-bar is unchanged throughout the optimisation while the original front light-bar is removed and replaced by an airfoil part next to the leading edge. The airfoil has a negative angle of attack, while was tuned so that airfoil's trailing edge is just below the top surface of the rear light- bar in order to leave the shape of the rear part of the roof unaffected. An example of the new roof design is shown in Figure 7.14.

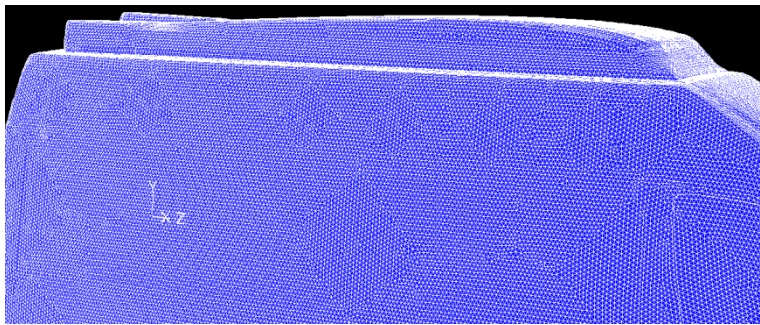


Figure 7.14 Ambulance roof profile based on airfoil design concept

Any conversion increases the aerodynamic drag in comparison with the non-converted (baseline) vehicle. Table 7.4 shows that the original conversion design results in a 20% increase in aerodynamic drag, whereas the roof optimisation concept developed would enable the increase in aerodynamic drag to be limited to just over 3%. Note also that this reduction in drag penalty is achieved even with a slightly increased projected area compared to the original conversion.

Fiat design	Projected area	C_D	Drag (N)	Drag difference (%)
Non-converted	5.92	0.29	760.5
Original	6.24	0.33	915.7	+20.4
Optimised	6.32	0.28	785.4	+3.2

Table 7.4 Aerodynamic performance for the original and optimised conversion designs

The reason for the improvement in the aerodynamic performance is shown by the flow field comparison in Figure 7.15. In the original conversion design the air flow separates immediately after the front light-bar whereas separation is delayed until

the rear of the vehicle in the optimised conversion. In addition, the height of the low pressure wake region is significantly smaller in the optimised conversion, as indicated by the arrows in Figure 7.16.

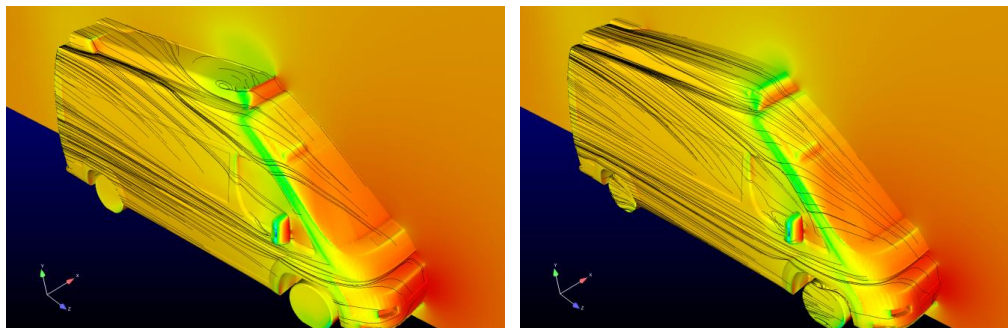


Figure 7.15 Pressure contours and velocity streamlines on the vehicle surface for the original (left) and optimised (right) design conversion.

Figure 7.16 shows flow path-lines and pressure contours on the vehicle surfaces. It shows how the optimised design avoids recirculating flow and reduces the low pressure area over the roof behind front light-bar

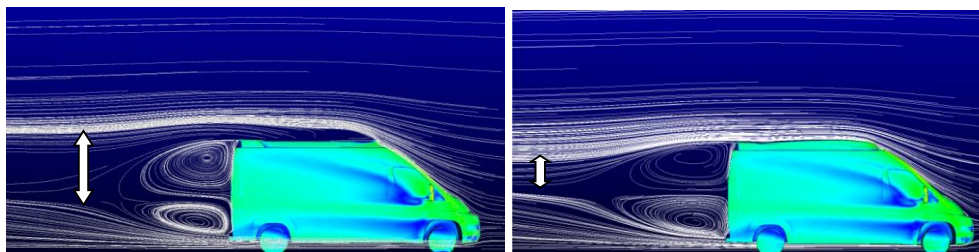


Figure 7.16 Velocity contours and streamlines for the original and airfoil based designs.

7.3. Police Van-conversion

This part consists of a formal optimisation of the aerodynamic design of van-conversion Police vehicle (Vauxhall Vivaro, see Figure 6.2), typically encountered within the United Kingdom. Similar to previous study, a flexible airfoil-derived parameterisation method is employed to derive roof designs which minimize the deleterious aerodynamic effects of the compulsory front and rear light-bars. A design parameterisation of a three-dimensional generic van model is carried out to enable optimisation, for a wide range of roof configurations. Optimal Latin Hypercubes for Response Surface Model building and model validation points are constructed using a permutation Genetic Algorithm and design points are evaluated

using CFD. Response Surface Models are built using a MLS approach. A series of optimisations for various roof configurations are performed using a Genetic Algorithm with responses calculated from the surrogates. This approach results in a set of optimised designs, from which appropriate roof design with lower drag can be obtained. The results presented show significant potential for aerodynamic drag and emissions reductions for Police vans. In practice, similar to the ambulance and due to a range of existing regulations, the shape of Police vehicle cannot be changed radically due to constraints on features such as the maximum vehicle height and the minimum vehicle. An additional complicating feature for aerodynamic design optimisation of Police vehicle is the need for warning lights at the front and rear of the roof. These require a flexible shape parameterisation scheme with appropriate bound constraints on the associated design variables. The computational procedure involves a sequence of CFD simulations for the drag estimation and unlike the previous study the optimiser will not control the CFD simulations and the drag force extracted from the CFD simulations will be used to obtain the Response Surface. The optimiser will then find the optimum using the Response Surface created using MLSM. RSM was used in this study in order to be able to see the behaviour of the design variables in relation to each other as well as visually observe the location of the local and global optimum which was not possible with the previous method.

7.3.1. CFD Modelling

The geometry of the generic Police van is shown in Figure 7.1 and is based on a typical Vauxhall Vivaro conversion used by Police Fleets (e.g. in West Yorkshire) in the UK. Figure 7.17 shows the schematic of the generic model. Similar technique and dimensions to the previous section were used in this work.

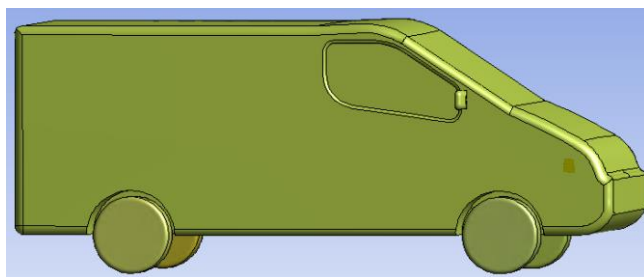


Figure 7.17 Generic model based on Vauxhall Vivaro

As discussed in previous chapter, the dimensions are sufficiently large to minimize any flow blockage effects and to adequately capture turbulent flow behind the

vehicle. Since several previous studies have shown that the family of two equation $k-\varepsilon$ models can be used to successfully predict aerodynamic drag on vehicles with dimensions similar to ambulance geometries, see e.g [10, 11, 30]. These are also used here to predict the aerodynamic drag of the Police van.

7.3.2. Boundary Condition and Mesh Generation

Similar boundary condition, as previous study, mentioned in table 1 was imposed on the model. In the study of the generic ambulance design an intermediate mesh, with approximately 7 million cells and a cell size of 30mm on the vehicle surface, was found to be satisfactory for the purpose of predicting the aerodynamic drag.

7.3.3. Model Configuration

An important example that is considered in this thesis is the addition of front and rear light-bars. The addition of light-bars to Conversion A in Figure 7.18, results in a 32% increase in the drag force.

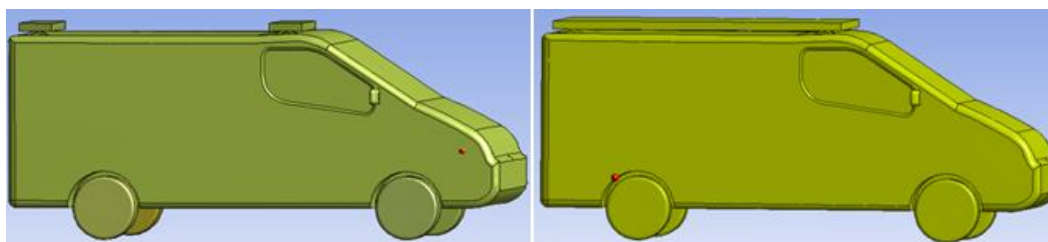


Figure 7.18 Van with light-bars Conversion A,(Original left), Conversion B(Right)

Although such increases in drag are inevitable when adding light-bars, simple design changes can reduce the magnitude of such increases. For example, connecting the front light bar to the rear one (Conversion B) is very effective in reducing the drag forces, this idea reduces the increase in the drag coefficient from the baseline Figure to only 7% (Figure 18). From a fluid mechanical perspective, the front light bar is an obstacle for the oncoming flow and it causes the flow separate, leading to the formation of a significant pressure drag. The rear light-bar also acts as a further obstacle to the flow and thereby contributes to a further increase in drag. By connecting two light bars together this area of flow separation is reduced, resulting in a lower aerodynamic drag.

7.3.4. Model Parameterisation

In the present work, the parameterisation is based on the tools provided by the commercial CFD software ANSYS Work-Bench [155] which was used to create the geometry and to carry out the modeling and mesh generation as the Gambit was not available anymore. A geometrical entity, based on a symmetric airfoil, has been chosen to represent a more aerodynamic roof configuration of the generic van conversion that embeds the front and rear light bars into the roof. In our design concept, the location of the maximum airfoil thickness represents the integrated front lights, see Figure 7.19.

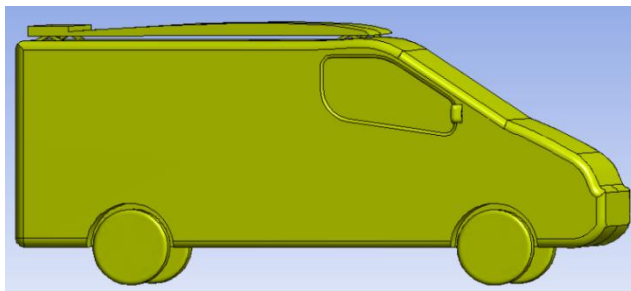


Figure 7.19 Model with airfoil configuration

The airfoil parameterisation used a simple NACA symmetric 4-digit profile [156] which was described in the previous section by equation 1 with two design variables as previous study, see Figure 7.20.



Figure 7.20 Design parameters

After preliminary consideration of a number of possible roof configurations generated by the vector $\mathbf{x}=(x_1, x_2)$, the boundary constraints on the design variables were assigned. These constraints are: $0 \leq x_1 \leq 1.5$ and $0.05 \leq x_2 \leq 0.15$.

7.3.5. Optimisation Method and Strategies

The objective function to be minimized is the aerodynamic drag force D (in Newton). Hence, in order to save computational time associated with GA, a

Response Surface Method (RSM) method is used to mimic the behaviour of the system response with respect to the change in design variables. DoE is carried out using an Optimal Latin Hypercube containing build and validation points. The surrogate is rebuilt using the combined building and validation DoEs. Global optimisation is performed using a Genetic Algorithm (GA) (refer to chapter 5.6.3) with responses calculated using the Response Surface Models

7.3.6. Optimisation Results

A 25 point optimal Latin hypercube DoE is constructed with three dimensions using the approach described earlier. Of the 25 points, 15 are building points and 10 are validation points. Equal weights are used in equation 4. The distribution of points in the design variable space is shown in Figure 6.21 and minimum distances in Figure 6.22. The values of standard deviation of minimum distances σ_b , σ_v and σ_m for building, validation and merged DoEs are found to be $\sigma_b= 0.56$, $\sigma_v= 1.26$ and $\sigma_m=0.54$ respectively, see Figure 7.21.

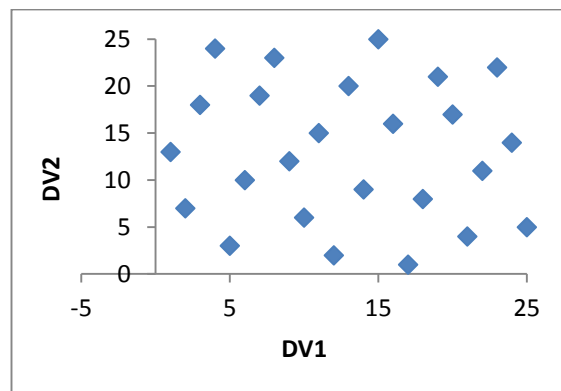


Figure 7.21 Distribution of normalised design points in the design variable space.

Optimisation was carried out using HyperStudy v11 software [157]. The drag force for each design point is extracted from the CFD data and MLS approximations of the response is then constructed using a second order base polynomial and the 15 model building points. The closeness of fit parameter is optimised using the 10 model validation points. MLS surfaces gave equally good agreement with building and combined DoEs (R^2 values of 0.996 and 0.986 for DOE_b and DOE_m respectively). However there was a slight difference in agreement with the validation points (R^2 values of 0.816). The surrogate function was then used in conjunction with GA to find the minima[158].

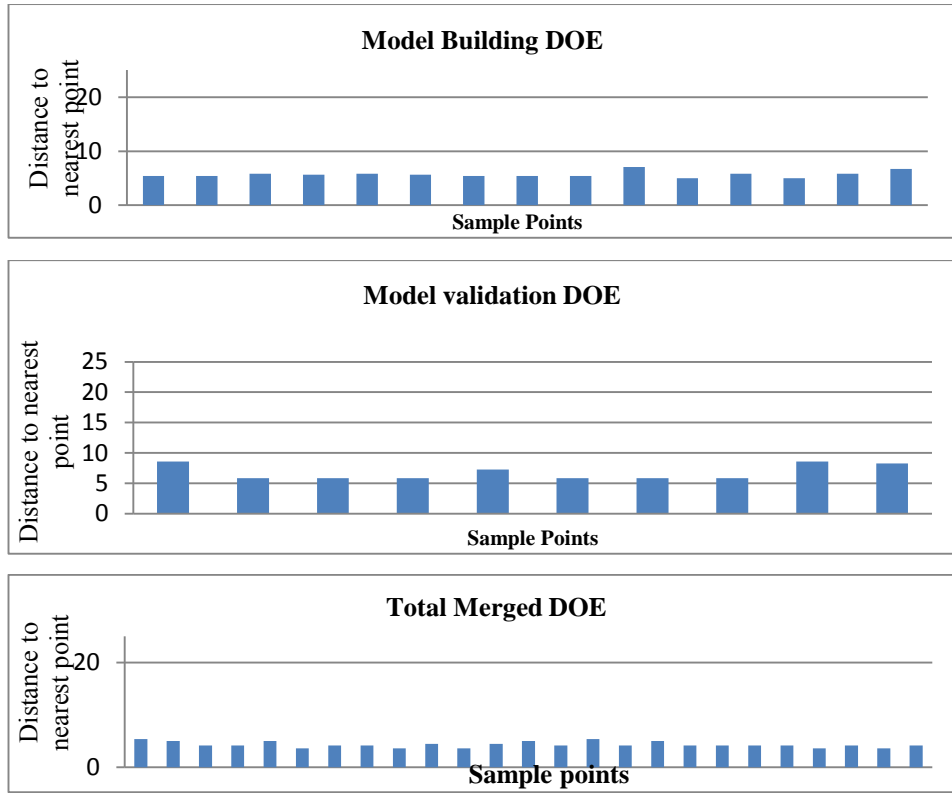


Figure 7.22 Sample points minimum distance plot for model building, validation and total merged DoEs.

The optimisation problem was formulated in order to minimize the objective function D (Drag Force). A GA was used to find a global minimum with fitness evaluations carried out by the Response Surface Models. The GA produced a design which, as predicted by the Response Surface Model, would reduce the drag force. CFD simulations of the optimised design was conducted and they showed a good agreement with the Response Surface Models with a $D = 438.36$ and $D = 437.244$ which are within 0.2% of the Response Surface' predictions. The agreement is summarised in Table 7.5.

	Responses
Optimised design after GA	438.36 (N)
CFD validation of the optimum	437.44 (N)
Error (Percentage)	0.2%

Table 7.5 Comparison of the responses obtained from the optimisation and CFD

The response surface is shown in Figure 7.23. The dark blue area corresponds to the minimum drag, indicating that the minimum drag mainly depends on the angle of

the airfoil and where the light bar is covered with the maximum angle of attack, the thickness is less influential.

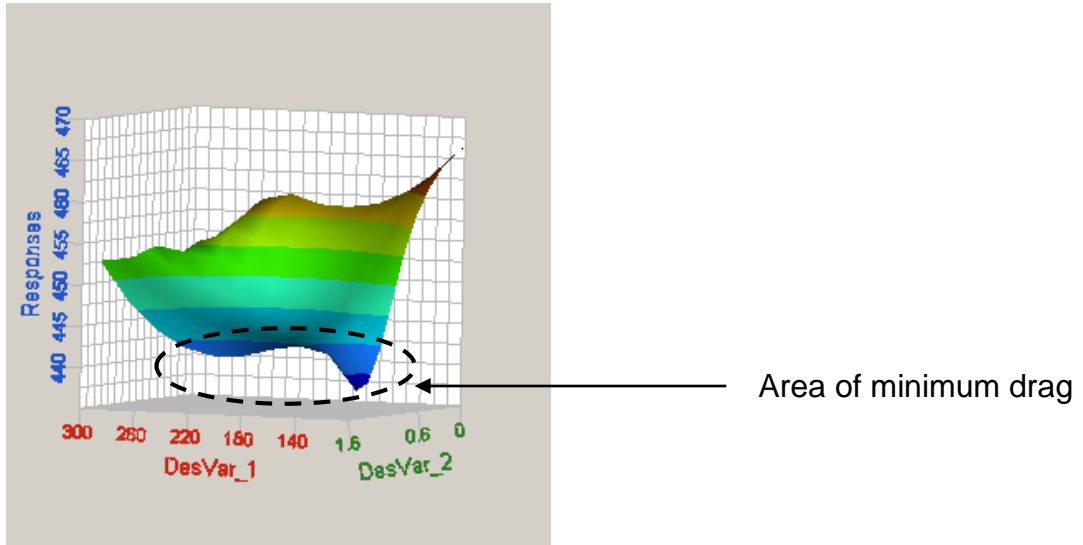


Figure 7.23 Minimum Drag force in Response surface of the Response Surface Model

Figure 7.24 shows the CFD model of the optimised design with the angle of 1.5° and the thickness of 5cm. The results of the optimisation are summarized in Table 7.6 which shows the drag calculation for the generic (unconverted) van, its conversion A with light-bars and the optimised design. The third column shows the difference in drag compared to the unconverted van without light-bars.

Designs	Drag force (N)	Drag Difference (%)
Van	408
Conversion A	540	+32
Optimised design	437	+7

Table 7.6 Drag comparison for the original and optimised design

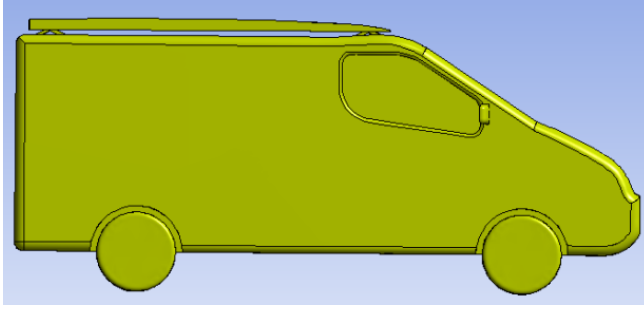


Figure 7.24 Optimum configuration of the light-bars

Figures 7.25 and 7.26 show the contours and streamlines of the velocity for the original conversion and the airfoil based design. The small red areas in front of the front light-bar for the original design indicates the increase in the pressure caused by the light bar's projected area and the blue area in the middle of two light bars, shows the low pressure and separation of the flow.

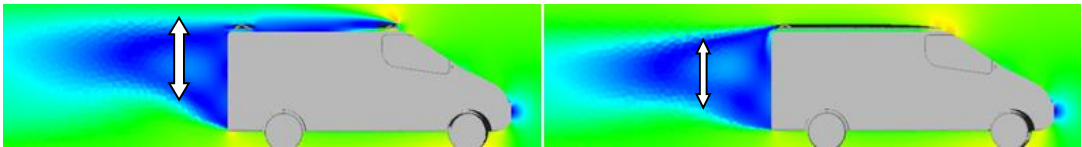


Figure 7.25 Contours of velocity for original and airfoil-based design

Modification of the roof shape, via the airfoil design, decreases the increase in the pressure in front of the vehicle and also minimizes the area of separation and low pressure between the light bars, which are mainly responsible for the drag production. Implying the airfoil design, as it can be seen in the Figures 7.25 and 7.26, would decrease the area of low pressure and circulation in the rear of the vehicle since the airfoil would redirect the flow downward. Eliminating the area of low pressure caused by separation, on the top and rear of the vehicle and well as removing the circulation on the rear, would decrease the drag force.

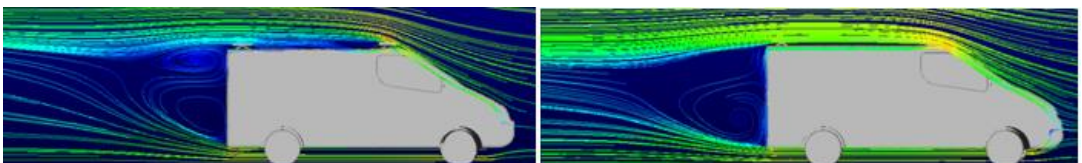


Figure 7.26 Velocity streamlines for original and airfoil-based design

The common feature of the optimal configurations is a trend to close the space (gap) between two entities (airfoil and rear light-bar). This has been achieved by the airfoil's trailing edge approaching the upper edge of the rear light-bar. In this way the rear light-bar has been completely integrated into the airfoil roof. This design resulted in a 25% drag reduction compared to the baseline drag of the unconverted van. Note that the restrictions on the design variables, to take account of practical constraints on the size of Police van, limit the scope for achieving greater drag reductions. For example, reducing the vehicle height (and/or decreasing its width) at its rear also offers significant drag reducing potential [7].

7.4. Police BMW 5series-conversion

The following is a formal optimisation study of the aerodynamic design of Police car. The car specified for this study is sedan BMW 5series which is used in some fleets within UK. In the present study, a third order Bezier curve is used as a tool to improve the existing design of the light- bars in order to reduce the drag force. The advantage of this choice is that, with only two design variables, all the design space can be searched [43]. A design parameterisation of a three-dimensional real car model is carried out to enable optimisation for a wide range of the configuration of the roof. Exactly similar method to section 7.3 were used in this study for the purpose of optimization.

7.4.1. CFD Modelling

The geometry of the model is shown in Figure 7.3 which is based on the real model of BMW 5series used in Police fleet, see Figure 7.27. Geometry clean-up of the CAD data was done using design modeller inside work-bench [93].

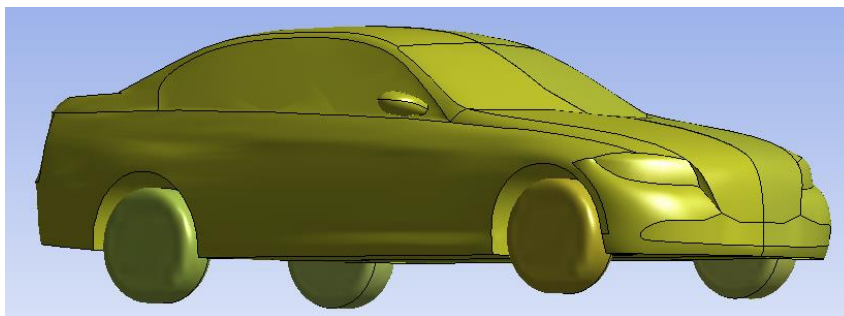


Figure 7.27 Real model of BMW 5series

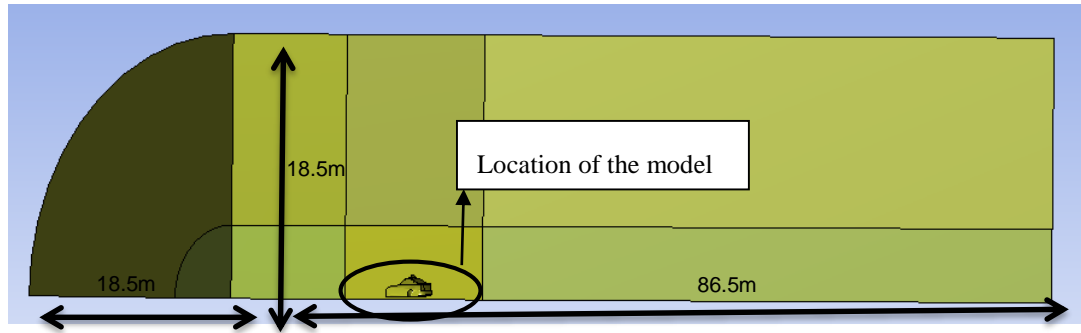


Figure 7.28 Wind tunnel domain

These dimensions are large enough to minimize any flow blockage effects (1%) and to adequately capture turbulent flow behind the vehicle, see Figure 7.28. Figure 7.29 also shows the mesh type and size around the vehicle in wind tunnel.

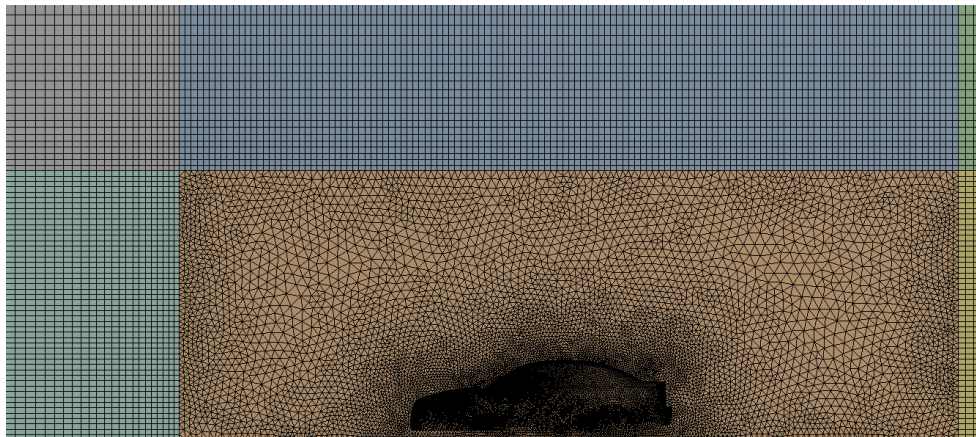


Figure 7.29 Illustration of the mesh type and size around the vehicle

7.4.2. Turbulence Model Comparison

The following study was also done in order to check the validity of the $k-\varepsilon$ models. BMW 5-series has a drag coefficient of 0.27 [150]. Following different turbulence models were used to simulate the drag coefficient and find the most suitable with the closest drag coefficient with the real one:

- $k - \varepsilon$ standard
- $k - \varepsilon$ Realisable
- $k - \varepsilon$ RNG
- $k - \omega$
- Spalart-Allmaras

Table 7.7 presents the results obtained from the simulations with the above turbulence models:

Turbulence Model	Drag Coefficient
$k - \varepsilon$ standard	0.25
$k - \varepsilon$ Realisable	0.19
$k - \varepsilon$ RNG	0.215
$k - \omega$	0.20
Spalart-Allmaras	0.21

Table 7.7 Drag coefficients for different turbulent models

The closest value to the real drag coefficient belongs to $k - \varepsilon$ standard with 0.25. The difference between the real drag coefficient of BMW 5-series with the one computed with $k - \varepsilon$ standard turbulence model is 7%. The main sources of error can be listed as below:

- 1) The main source of error comes from the fact that the model was simplified in order to be made suitable for the CFD simulation. As the model was simplified by removing the windows and so on..., therefore flow would move smoother around it and the drag coefficient would be lower.
- 2) Numerical simulation with CFD may not be able to capture the total behaviour of the flow around the vehicle therefore there is always some difference between the values.

Along with the previous literature, the following result confirms $k - \varepsilon$ (in this case, standard) can be an accurate method to capture the flow behaviour around the vehicle which contains separation, reattachment and circulation.

7.4.3. Model ConFiguration

Adding the light bar (Conversion A, Figure 7.30) to the benchmark model would increase the drag force by 34% as it is shown in table 7.8. Such a conFiguration of the light bars is used in one fleet in West Yorkshire.

Model	Drag force (N)	Drag difference (%)
Base	172.80
Converted	232.10	+34

Table 7.8 Drag forces comparison for car with and without light bar

The light bar which is located on the middle of the roof is an obstacle for the oncoming flow and it forces the flow to change its direction when moving forward. That causes the drag force to increase. Immediately after the light bar, there will be an area of separation as the flow moves down, see Figure 31.

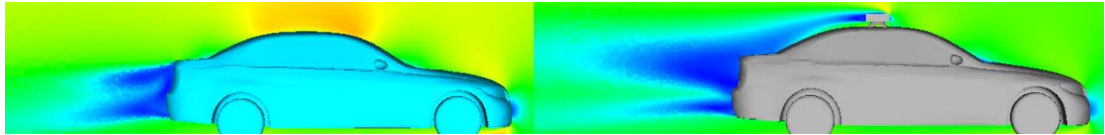


Figure 7.30 Velocity contour for base car and converted one with light bar

7.4.4. Parametric Study

In order to find the effects of the different parameters on the drag force produced by the light-bar, a parametric study was done on the following parameters; see an example in Figure 7.31.

- Radius of curvature (0 to 50 mm)
- Height (50 to 100 mm)
- Width (200 to 310 mm)



Figure 7.31 Light bar with and without rounded edge

Since the simulation is expensive, complete parametric study cannot be done and therefore only corner points were modelled and simulations were done only for these

cases in order to find, not only the best possible combination, but also to see how effective they are in regards to drag force production:

Radius of curvature (degree)	Heigh (mm)	Width (mm)	Drag (N)
0	50	200	195
0	50	310	194
0	100	200	241
0	100	310	232
50	50	200	181
50	50	310	181
50	100	200	196
50	100	310	199

Table 7.9 Results of parametric study

From the above results, it can be seen that as the radius of curvature changes from 0 to the maximum of 50 mm while other parameters are still the same; the drag force reduces considerably by as much as 24% from the maximum 241N to the minimum 181N. By also looking at the height of the light bar, it can be seen that, the drag force increases as the height changes from 50 mm to 100 mm. It is interesting to see that the width of the light bar DoEs not influence the drag force and it only increases the drag force slightly as it moves from 200 mm to 310 mm. Optimisation was also performed with the above results and the minimum dimensions and drag force was confirmed. Figure 7.32 is the approximation surface (MLS) for the design variable 1 (radius of curvature) and design variable 2 (height) versus drag force. It clearly shows the minimum drag force is where the radius of curvature is at its maximum and height is at its minimum and the drag force increases as we move from these points.

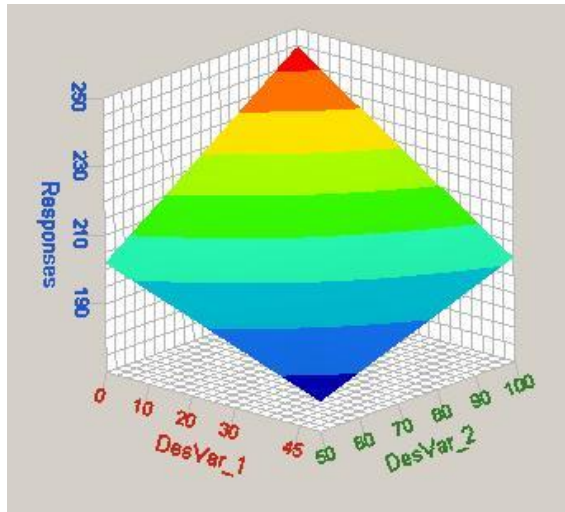


Figure 7.32 Approximation surface for DV1 and DV2 versus drag force

Figure 7.33 also shows the approximation surface for design variable 2 (height) and design variable 3 (width) versus drag force. It again confirms that the minimum drag belongs to the points where the height is the minimum. It also shows that as the width moves from 200 mm to 310 mm the drag force DoEs only change slightly and therefore the projected area plays an important role in drag production and width DoEs not influence it much. Figures 7.32 and 7.33 are effectively planar and optima are at the design space boundaries.

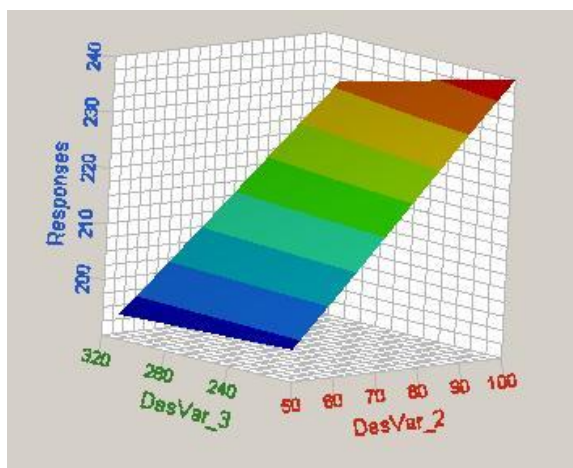


Figure 7.33 Approximation surface for DV1 and DV2 versus drag force

Another study was conducted on the effect of the height of the light-bar on the drag force it produces. The light bar was placed directly on the roof without any stands to see the effect it has on the drag force. Figure 7.34 shows the example of light bar distanced from the roof and the one attached to it and the result indicates that by

placing the light bar on the roof, which would not be against the regulation, the drag force will be slightly reduced therefore the optimisation was done on the model with zero height roof.



Figure 7.34 Light bar with 0 and 48 mm height

Table 7.10 contains the results of the above study:

Height of the light bar (mm)	Drag force
48	232
0	225

Table 7.10 Results for the height of light bar study

7.4.5. Model Parameterisation

The parameterisation, in this work, is based on the tools provided by the commercial CFD software Work-Bench which was used for Creating the geometry, modeling and mesh generation. Bezier curve has been chosen in order to represent the potential (Optimal) conFIGuration of the roof of the BMW 5series Police car conversion that embeds the light bar. Cubic Bezier curve which has 4 control points was used and has been described by the following expression:

$$B(t) = (1 - t)^3 P_0 + 3(1 - t)^2 t P_1 + 3(1 - t) t^2 P_2 + t^3 P_3, t \in [0,1] \quad (7.2)$$

Where t is the parameter that varies between 0 to 1 and p is represents the control points. The Bezier curve profile was defined using 100 equally distributed points. Two design variables were used for shape optimisation of the vehicle roof, the design variables are linked to the length (see Figure 7.35) and sharpness (see Figure 7.36) of the curve and the height of the light bar remains unchanged during the optimisation.

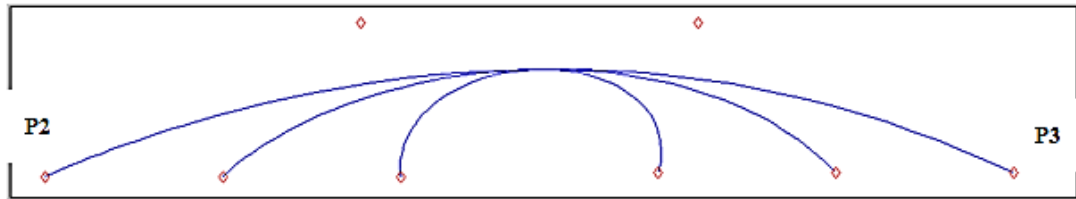


Figure 7.35 Design parameter 2, length

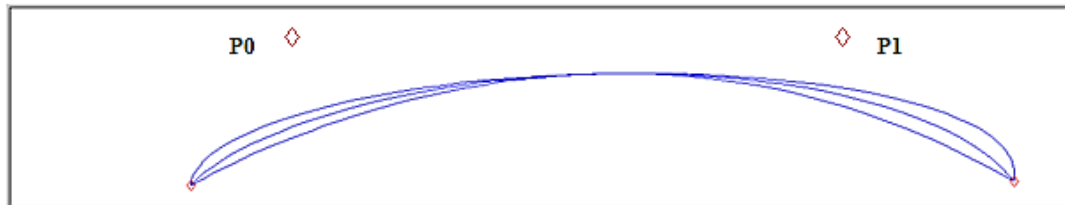


Figure 7.36 Design parameter 1, sharpness

Therefore the distance between P_0 and P_1 determines the sharpness of the curve and distance between P_2 and P_3 determines the length of the curve.

7.4.6. Optimisation method and Results

Similar method and strategies as previous model in section 6.3 have been implemented as the optimisation method and strategies. The objective function also remains as drag force. 25 DoE points were generated similar to the previous study, see table 7.21 and 7.22. Values of standard deviation of minimum distances σ_b , σ_v and σ_m for building, validation and merged *DoEs* are found to be $\sigma_b=0.56$, $\sigma_v=1.26$ and $\sigma_m=0.54$ respectively.

Similar method, techniques and values to the previous section were used for the optimization study. MLS surfaces gave equally good agreement with building and combined *DoEs* (R^2 values of 0.9883 and 0.904 for *DoE_b* and *DoE_m* respectively). However there was a slight difference in agreement with the validation points (R^2 values of 0.811). The surrogate function was then used in conjunction with GA to find the minima, using a second order base polynomial and the 15 model building points.

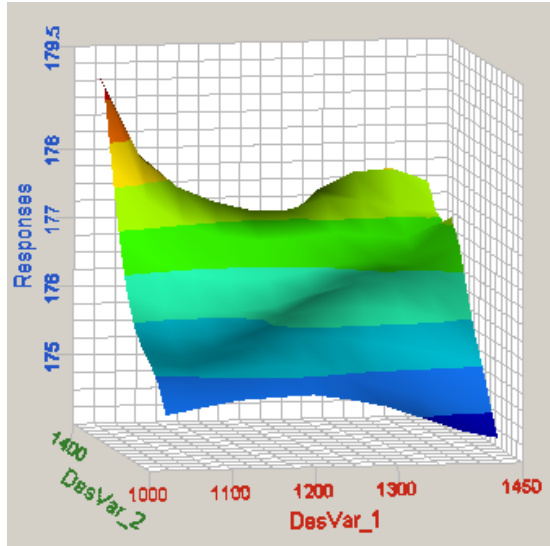


Figure 7.37 Response surface Model

The optimisation problem was formulated in order to minimize the objective function which is drag force. Genetic Algorithm (GA) (refer to chapter 5.6.3) was used to find a global minimum with fitness evaluations carried out by the Response Surface Models. The GA produced a design which, as predicted by the Response Surface Model, would reduce drag force. CFD studies were made of the optimised designs. They showed good agreement with the Response Surface Models with a $\sigma_D = 174.36$ and $\sigma_D = 173.43$ which are within 0.5% of the surrogates' predictions. A summary is given in Table 7.11.

	Response (N)
Optimised design after GA	174.36
CFD validation from optimum	173.43
Error (Percentage)	0.5%

Table 7.11 Comparison of the responses obtained from the optimisation and CFD

Dark blue area in Figure 7.39 corresponds to the minimum drag which indicated the minimum drag mainly depends on the sharpness of the Bezier curve (Figure 7.35) and the length of the curve (Figure 7.36) is less influential on the variation of the drag force and plays a less important rule. Therefore the minimum drag is when the length and the sharpness of the curve are at their maximum. Figure 7.40 shows the CFD model of the optimised design. The results of the optimisation are summarized

in table 7.12, which shows the drag calculation for the Generic police car, its conversion with light-bars and the optimised design.

Designs	Drag force (N)	Drag Difference (%)
Base Car	172.80
Conversion A (48 mm height)	232.00	+34
Conversion B (0 mm height)	225.00	+30
Optimised design	173.43	+0.5

Table 7.12 Drag comparison for the original and optimised design

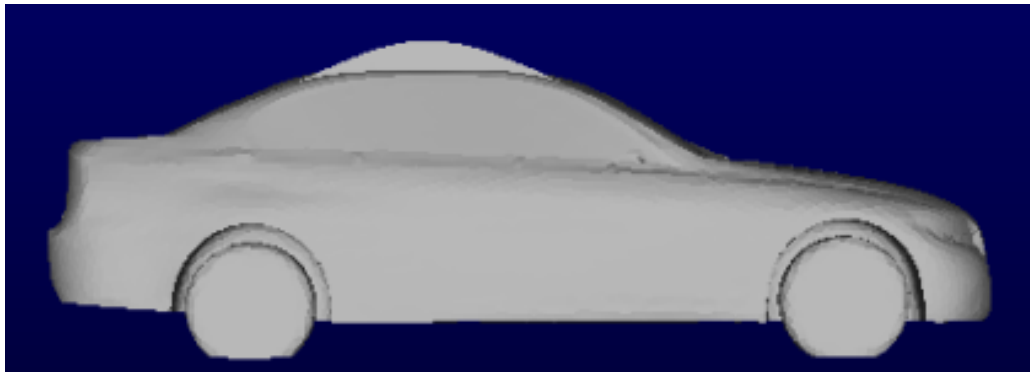


Figure 7.38 Optimum conFiguration of the car with light bar

Figure 7.41 and 7.42 show the contours and streamlines of the velocity for the original conversion and the Bezier curve based design. Blue colour in the Figures indicates the area of low pressure which is the main cause of drag production. For the base car, this area is only at the rear of the vehicle and is a result of separation and circulation of the flow. For the car with light bar, blue area extends to the roof and just after the light bar, since the light bar acts as an obstacle and the flow separates from the roof and circulates which cause the drag to increase. As it can be seen in the Figure for the optimum case, the blue colour on the roof disappears and since the flow is more directed towards the ground with new configuration of the roof, there is a reduction in the low pressure and circulation area on the rear of the vehicle. That is why the drag force for the new configuration (optimum case) is almost as low as for the base car.

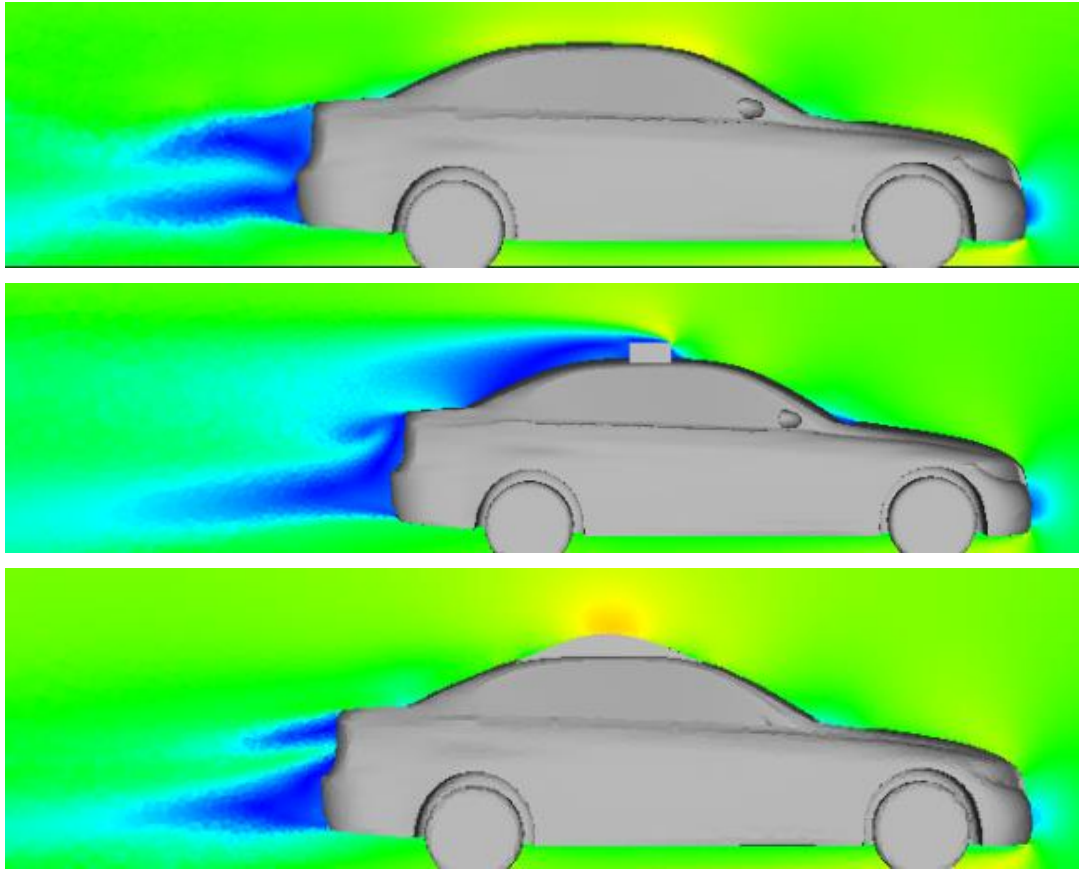


Figure 7.39 Contours of velocity for original and airfoil-based design

Modification of the shape, by placing the Bezier curve, will decrease the pressure in front of the light bar and also completely removes the area of separation and low pressure after the light bars, which are mainly responsible for the drag production. By implying the Bezier curve design, as it can be seen in the Figures 7.41 and 7.42, the flow is redirected downward. Eliminating the area of low pressure caused by separation, on the top and rear of the vehicle, and removing as well the circulation on the rear, would decrease the drag force.

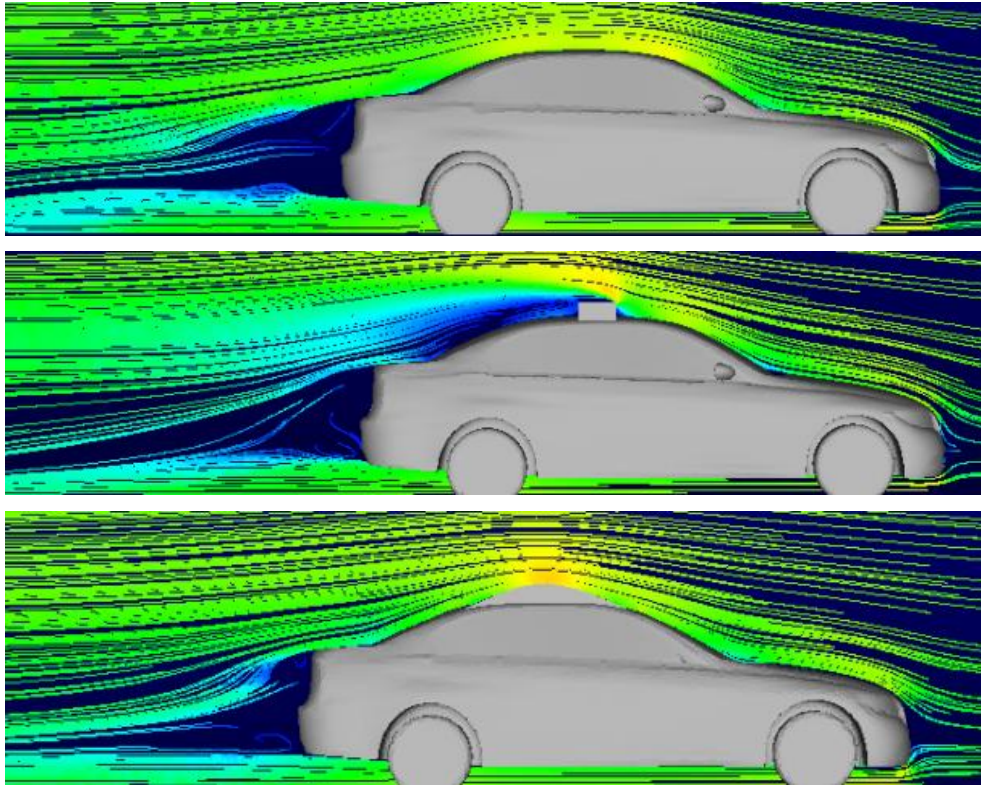


Figure 7.40 Velocity streamlines for original and airfoil-based design

The common feature of the optimal configurations is that they eliminate the area of the low pressure after the light bar and reduces the circulation on the rear of the vehicle by directing the flow downwards. This design has corresponded to improvement of 23%. Note that the restrictions on the design variables, to take account of practical constraints on the size of Police car, limit the scope for achieving greater drag reductions. For example, reducing the vehicle height (and/or decreasing its width) at its rear also offers significant drag reducing potential [7].

7.5. Experimental and CFD Analysis of Optimised Model

Following the experiments and CFD validation for base model the model with light bars in chapter 6, similar study was conducted for the optimised version of the exact model. The experiment was conducted at the same facility with the same condition.

The aim of this experiment was to compare the drag force and coefficient of the optimised model of Vauxhall Vivaro with numerical CFD results for the validation purpose as well as assessing the aerodynamic improvements of the optimum design and measure their significance. Similar to the chapter 6 the experimental results were compared with the numerical simulations of different turbulent models and

different mesh element size. Figure 7.43 shows the 1/8 scaled model used for the experiment with its corresponding CAD model.

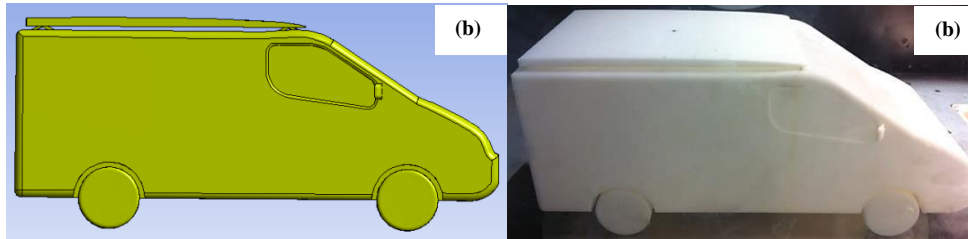


Figure 7.41 Optimum configuration of the light-bars, (a) CAD model, (b) Physical wind tunnel model

Table below contains the experimental drag force and coefficient for different velocities for the model with optimised light bar:

Velocity (m/s)	Drag Force (N)	C_D
13	2.61	0.348
20.55	6.13	0.327
22.51	7.23	0.315
26.64	9.91	0.315

Table 7.13 Drag force and coefficient for different Velocities for optimum design

Flow visualisation was also used in order to see the effect of the optimisation of the flow field and how it controls the flow behaviour. Figure 7.44 shows the flow visualisation using tufts of wool for the optimum design for the velocity of 26.64 m/s.



Figure 7.42 Flow visualisation using tufts for optimised model (rear view)

By means of optimisation the flow has been controlled and the separation and the circulation have been completely eliminated on the top of the vehicle. The amount of the circulation has also been reduced on the rear of the vehicle as it can be seen on Figure 7.44 and 7.45.



Figure 7.43 Flow visualisation using tufts for optimised model (side view)

The flow is attached to the roof of the vehicle and there is only minor circulation on the rear. This reduces the drag force by almost 30% compared with the original light-bar set up. Similar method as chapter 6 was used for the CFD simulation of the optimised model and the experimental data was used to assess the accuracy of the simulation. Table below contains the drag force and coefficient for 4 different turbulence model compared with the experimental value for velocity of 6 m/s.

Turbulence Model	Drag Force (N)	C_D
S – A	10.1	0.337
K – ϵ (Re)	9.10	0.304
K – ϵ (S)	15.88	0.520
K – ω	13.04	0.450
Experiment	9.91	0.315

Table 7.14 Comparison of the Drag force results of the medium mesh density for different turbulent models for the optimised model for 26 m/s.

Similar to the previous finding in chapter 6, that S – A and K – ϵ (Realisable) almost match the experimental values for all four different models. K – ϵ (Standard) and K – ω are not as good agreement as the previous mentioned

models. Therefore as it was mentioned before, it can be concluded that S – A is the most suitable turbulence model to predict the drag force of the vehicle and assess its aerodynamics characters. Table 7.15 compares the results of the experiment for the baseline, light-bar, flat light-bar and the optimised model for 26.64 m/s.

Model	Experimental C_D	Difference %
Baseline	0.308
Light-bar	0.406	32
Light-bar-flat	0.377	22
Optimised	0.315	2.2

Table 7.15 Comparison of the experimental drag coefficient

The drag coefficient increases by 32% by adding the light-bars similar to the drag force increase. It can be seen that there is only slight increase in the value of drag coefficient for optimised model comparing to the base model. The drag coefficient increase by adding the add-ons, reduces from 32% to 2.2% by means of CFD optimisation. As Figures 7.46 and 7.47 show similar to the experimental flow visualisations on Figures 6.22 and 6.23, the separation and the low pressure region is controlled by placing the optimised light-bar. As wind tunnel experiment showed the flow stays attached to the top of the vehicle and the circulation region on the rear is also reduced. Low pressure region (blue streamlines) are completely eliminated on the top of the vehicle as it was previously seen on Figures 7.46 and 7.47 from the wind tunnel experiment.

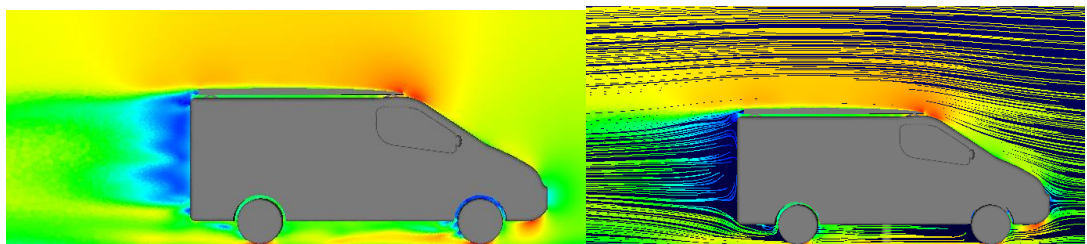


Figure 6.46 Velocity contour and streamline of the optimised model

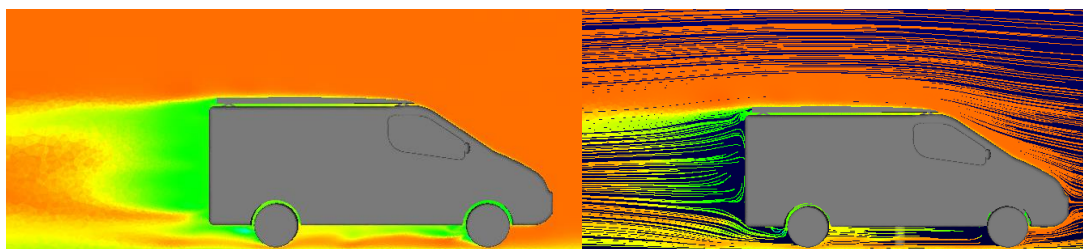


Figure 6.47 Pressure contour and streamline of the optimised model

The flow field from the CFD results are consistent with the experimental flow visualisation and it can therefore be concluded that CFD simulation has been used successfully in order to measure the aerodynamic characters of the vehicles such as drag force. This enables aerodynamic optimisation to be carried out effectively using CFD.

7.6. Concluding Remarks

Rising fuel costs, coupled with the need to reduce the need to reduce the environmental impact of its fleet operations, are now stimulating interest in improving the aerodynamic design of ambulances and Police car for the first time. CFD is now capable of predicting the drag on a range of vehicles accurately. The above studies are the first to combine CFD with formal optimisation methods to investigate the potential for reducing the aerodynamic design of Emergency Response Vehicles. It has shown that, although industrial users will need to invest substantial effort in providing CAD models that are suitable for CFD packages, improving the aerodynamic design of the roof and light-bars in Emergency Response Vehicle conversions offer a significant opportunity for reducing the fuel consumption resulting from ambulance and Police fleet operations.

8. Discussion and Conclusions

The focus of the research reported in this thesis is Computational Fluid Dynamic Based Optimisation of Emergency Response Vehicles with the aim of reducing the drag force of the vehicles in interest and consequently lowering the fuel consumption of their fleet. This was achieved by using computational and experimental techniques to assess and control the flow behaviour around the vehicles. The main findings of the investigation are summarised below together with suggestions for future work and closing concluding remarks.

8.1. Validation

First, a preliminary study demonstrated the feasibility of using RANS turbulence models for predicting the drag force of Emergency Response Vehicles. For the scale model considered, a good match was found between the experimental and computational results, in terms of the drag force and coefficient. The Spalart Allmaras (S-A) turbulence model exhibited the best overall performance in terms of obtaining quantitative results. The standard $K - \varepsilon$ and the $K - \omega$ were found to over-predict the magnitude of the drag force and $K - \varepsilon$ (Realisable) over-predicted the value of drag force. Broadly speaking, grid independence study was also conducted and the medium grid size provided the best prediction of the drag force. As a result of this, the good match with experimental data and suitable wall y^+ values, the S - A model on the medium density tet-hex grid proved to be the most suitable. The strong aspect of the experiment was that the 100 readings were taken for each test and average value was used for the comparison with the CFD calculations. Another strong aspect of the experiment was that the model was placed above the boundary layer thickness in order to prevent the result to be affected by the formation of the boundary layer on the floor of the wind tunnel. The CFD simulations comparison was done with a like-for-like model which would again strengthen the experiment and CFD comparison study. In summary the flow field from the CFD results are also consistent with the experimental flow visualisations. It can therefore be concluded that CFD simulation can be used in order to measure the aerodynamic characters of the vehicles such as drag force and the flow behaviour can also be assessed by means of CFD simulations.

8.2. Emergency Response Vehicles Design Optimisation

In chapter 7, aerodynamic shape optimisation was applied to roof with light-bars of three different Emergency Response Vehicles. The feasibility of applying formal optimisation techniques in search of the best design for minimum drag was considered. Multi Approximation method and Response Surface method was used to optimise the vehicles of interest in this study. Moving least squares (MLS) Response Surface was constructed using a series of High-fidelity CFD solutions in an effort to model the CFD responses. Response Surface was used through traditional optimisation techniques, giving a potential candidate for minimum drag. Subsequent CFD simulations on the proposed designs gave the desired result with overall drag reductions. Concluding remarks of the studies on chapter 7 are as below:

8.3. Optimization Techniques

The first optimization study (ambulance van conversion) was based on the Computational Fluid Dynamics (CFD), and the Multipoint Approximation Method (MAM), which is a direct optimization method. This method is based on a mid-range approximation framework that replaces the original optimisation problem by a succession of simpler mathematical programming problems. The functions in each iteration present high quality, noise free mid-range approximations to the corresponding original functions. The solution of an individual sub-problem becomes the starting point for the next step, which is repeated iteratively until the optimum is reached. MAM minimizes the number of expensive function evaluations and deals effectively with the numerical noise. The relationship between the design variables and also their behaviour cannot be seen and local optimum may be achieved rather than the global optimum and it is suitable for problems with high number of design variables.

For the two remaining studies (Police van-conversion and Police BMW 5series-conversion), response surface method (virtual optimization) was used. The optimisation study was based on Computational Fluid Dynamics (CFD), Optimal Latin Hypercube (OLH) Design of Experiments (DoEs) and the Response Surface Modelling. The roof with light bar design is parameterized into two key design variables and a number of designs are produced using an Optimal Latin Hypercube design of experiments. Each design is evaluated using CFD analysis and Moving Least Squares Response Surface Models of primary and entrained flow rates are built. Finally a set of optimisations using a Genetic Algorithm and sequential quadratic programming are performed to define a front along which optimal designs

exist. Despite this method require more high fidelity CFD simulations, but it allows to observing the behavior and also using response surface and the optimum point can see the relationship between the design variables by using response surface and the optimum point visually. This method is desirable when the numbers of design variables are low.

8.4. Results

Adding the light-bars on the roof on the fiat van (ambulance van conversion), as table 8.1 shows, results in a 20% increase in aerodynamics drag. Whereas the roof optimization concept developed would enable the increase in aerodynamic drag to be limited to just over 3%.

Design	Drag (N)	Drag difference (%)
Non-converted	760.5
Original	915.7	+20.4
Optimized	785.4	+3.2

Table 8.1 Drag comparison of base-line, original and optimized Fiat ambulance van conversion

For the second study (Police van-conversion), the results are shown in table 8.2. The drag reduction is in the order of 25%. Adding the light-bars will increase the drag by 32% and as it can be seen in table 8.2, the optimized model only increases the drag force by 7%.

Design	Drag (N)	Drag difference (%)
Base-line model	408
Conversion A	540	+32
Optimized design	437	+7

Table 8.2 Drag comparison of base-line, original and optimized Fiat ambulance van conversion

Results of the final study (Police BMW 5series-conversion) are included in table 8.3. It shows the greatest improvement possibly because of the type of the vehicle

(sedan) studied. The increase in the drag force is from 30% for the vehicle with the light-bar to only 0.5% for the optimized model.

Design	Drag (N)	Drag difference (%)
Base-line model	172.80
Conversion A	540	+32
Optimized design	437	+7

Table 8.3 Drag comparison of base-line, original and optimized Fiat ambulance van conversion

The use of CFD within an optimisation framework, where a suitable objective function is chosen to represent the desired outcome, allows efficient use of computational resource. The choice of objective function is crucial in determining what constitutes an optimal design; the challenge is to interpret the physical parameters (velocities, pressure, etc) from the CFD solution in a way that links with the objective function of choice. The CFD based optimization, therefore, shows an effective way to optimized the shapes of the emergency response vehicles and consequently can achieve lower fuel consumptions for a particular vehicle as follows:

8.5. Fuel Consumption

As noted earlier, interest in the aerodynamic performance of Emergency Response Vehicles, is stimulated by the need to improve fuel economy and reduce emissions from their fleet operations. Since there are not any previous study on the fuel consumption of the Emergency Response Vehicles, the improvements in fuel consumption resulting from the reduced aerodynamic drag of the optimised design are quantified based on the trends identified for HGVs. Comprehensive data on the fuel consumption of the HGVs are available in studies [16, 19, 37]. The relationship between drag reduction and fuel economy improvement for speeds of 30, 60 and 90 km/h presented in [16] are shown in Table 8.1, with similar findings presented in [37].

Vehicle Speed (mph)	Aerodynamic Drag Reduction to Increase Fuel Economy 1%
60	2%
40	3%
20	6%

Table 8.4 Relationship between drag reductions and fuel economy improvement for tractor-trailer trucks [16]

Table 8.2 shows the benefits of the optimised design of the models considered, in terms of drag force reduction compared to the baseline conversion for vehicle speeds up to 60 mph, together with the predicted benefits in terms of reduced fuel consumption for a range of vehicle. This shows that, compared to the baseline model, there is fuel consumption reduction in the range of 8.6% to 12.5% for different vehicles at 90 km/h.

Model	Drag Reductions (%)	Fuel Consumption Reduction (60m/h) (%)
Ambulance Van-conversion	17.2	8.6
Police Van-conversion	25	12.5
Police BMW conversion	23	11.5

Table 8.5 Drag and Fuel consumption reductions for optimised Emergency Response Vehicles

The data shown in table 7.4 is in the form that can be used to predict actual fuel savings, once a representative ambulance duty cycle has been obtained.

8.6. Future work

Since recessing the light-bars into the body of the vehicle would affect the structure of it, manipulation of the geometry above the roof was only investigated. It is worth investigating of placing the light-bars into the roof of the different Emergency Response Vehicles to measure its effect on the Drag force, when proper structure analysis can take place.

Further improvements can be obtained by optimising other parts of the vehicle, such as the lower surface and under-body features, and focussing on weight reduction, as

is common in the aerospace industry, would also have a significant beneficial effect on overall fuel consumption.

There is also a need for identifying realistic ambulance duty cycles where the predicted drag reductions, as a function of vehicle speed, can be used to predict the fuel savings achievable in practice.

It is also important to note that the aerodynamic modifications proposed have to be assessed in terms of the practical costs of manufacturing them. Following are also weakness of the work:

- Low number of design parameters
- Result strongly depended on parameterisation, which can be removed by the method of Jens Muller [72] and Carsten Othmer [52, 53, 65, 69]
- More efficient optimisation method may be used

8.7. Conclusion

The complementary nature of experimental and computational analysis has facilitated a detailed and systematic investigation into the passive manipulation of Emergency Response Vehicles exterior design in order to minimise the drag force and consequently lowering the fuel consumption. Light-bars are found to increase the drag force by almost 30% for different vehicles due to the increase in the projected area and separation of the flow.

At the speed of 90 km/h which is the typical speed of Emergency Response Vehicles, 30% increase in the drag force account for 15% increase for the fuel consumption.

Aerodynamic shape optimisation has been applied successfully to the design of light-bars reducing the drag acting on the vehicle by 25%, leading to a fuel consumption reduction of 12.5%.

Emergency Response Vehicles such as ambulance and Police cars can benefit from the application of the optimisation methods that have been developed in this thesis.

9. References

1. Mohamed-Kassim, Z. and A. Filippone, Fuel savings on a heavy vehicle via aerodynamic drag reduction. *Transportation Research Part D: Transport and Environment*, 2010. 15(5): p. 275-284.
2. Wood, R.M., Impact of Advanced Aerodynamic Technology on Transportation Energy Consumption, 2004, SAE International 10.4271/2004-01-1306.
3. Shankleman, J. "BusinessGreen Leaders Awards 2011: Yorkshire Ambulance Service changing the shape of UK's emergency services," [cited 2011 1 August]; www.businessgreen.com].
4. Soto, O. and R. Loehner, CFD shape optimization using an incomplete-gradient adjoint formulation. *International Journal for Numerical Methods in Engineering*, 2001. 51(6): p. 735-753.
5. McCallen, R.B., F. Ross, J., *The Aerodynamics of Heavy Vehicles: Trucks, Buses, and Trains*. 2004: Springer.
6. McCallen, R.C.S., K. Ortega, J. DeChant, L. Hassan, B. Roy, C. Pointer, W.D. Browand, F. Hammache, M. Hsu, T.Y. Leonard, A. Rubel, M. Chatalian, P. Englar, R. Ross, J. Satran, D. Heineck, J. T. Walker, S. Yaste, D. Storms B., DOE's Effort to Reduce Truck Aerodynamic Drag - Joint Experiments and Computations Lead to Smart Design. 34th AIAA Fluid Dynamics Conference and Exhibit W-7405-ENG-48, 2004.
7. Raveendran, A.S., S. N. Rakesh, D. Shankapal, S. R., Exterior Styling of an Intercity Transport Bus For Improved Aerodynamic Performance. SAE International 2009-28-0060, 2009.
8. Bayraktar, I. and T. Bayraktar, Guideline for CFD Simulation of Ground Vehicle Aerodynamics. SAE International 10.4271/2006-01-3544, 2006.
9. Muyl, F.D., L. Herbert, V., Hybrid method for aerodynamic shape optimization in automotive industry. *Computers & Fluids*, 2004. 33(5-6): p. 849-858.
10. Williams, N.A.G., J. H. Letherwood, M., Drag Optimization of Light Trucks Using Computational Fluid Dynamics. SAE International 2004-01-2617, 2004.
11. Gilkeson, C.A., Thompson, H.M, Wilson, M.C.T, Gaskell, P. H. and Barnard, R.H. , An Experimental and Comutational Study of the Aerodynamic and Passive Ventilation Characteristics of small Livestock Trailers. *Journals of Wind Engineering & Industrial Aerodynamics*, 2009. 97: p. 415-425.
12. Buil, R.M. and L.C. Herrer, Aerodynamic Analysis of a Vehicle Tanker. *Journal of Fluids Engineering*, 2009. 131(4): p. 041204-041204.
13. surreywebmaster. 2011 BMW 5 Series Police Car. 2014 [cited 2014 17 June]; <http://blog.old-and-bold.info/?p=1424>].

14. Triantafyllou, M.B., D. S. Needham,, Method and Apparatus for Reducing Drag on a Moving Body 5740750, 1998, Massachusetts Institute of Technology, Cambridge, Mass: United States.
15. Reynolds, O., An Experimental Investigation of the Circumstances Which Determine Whether the motion of the Water Shall Be Direct or Sinuous, and of the Law of resistance in Parallel Channels. Philosophical Transactions of the Royal Society of London, 1883: p. 935-982.
16. Bauer, S.R., M. Wood, X. Steven, X., Simple and Low Cost Aerodynamic Drag Reduction Devices for Tractor-trailer Trucks. SAE International Truck and Bus 2003-01-3377, 2003.
17. Pointer, W.D.S., T. Weber, D., Development of Guidelines for the Use of Commercial CFD in Tractor-Trailer Aerodynamic Design. Commercial Vehicle Engineering Congress and Exhibition Chicago, Illinois, 2005.
18. Huminic, A. and G. Huminic, CFD Study concerning the Influence of the Underbody Components on Total Drag for a SUV. SAE International, 2009.
19. McCallen, R.C., R. Hsu, J. Browand, F. Hammache, M. Leonard, A. Brady, M. Salari, K. Rutledge, W. Ross, J. Storms, B. Heineck, J. Driver, D. Bell, J. Zilliac, G., Progress in Reducing Aerodynamic Drag for Higher Efficiency of Heavy Duty Trucks. SAE Technical Paper 1999-01-2238, 1999.
20. Verzicco, R.F., M. Iaccarino, G. Khalighi, B. Moin, P., Large Eddy Simulation of a Road Vehicle with Drag-Reduction Devices. AIAA Journal 10.2514/2.1613, 2002. 40(12): p. 2447-2455.
21. Duncan, B.K., S.Sbeih, K.Lounsberry, T.Gleason, M., Further CFD Studies for Detailed Tires using aerodynamics Simulation with Rolling Road Condition. SAE International 2010-01-0756, 2010.
22. Robert H. Walter, K.G., T. Hassan, B. Suazo, J. E. Riggins, A. J., Experimental Investigation of the Ground Transportation Systems (GTS) Project for Heavy Vehicle Reduction, 1995.
23. Schoon, R. and P.F. Peter, Practical Devices for Heavy Truck Aerodynamic Drag Reduction. SAE International 2007-01-1781, 2007.
24. Aider, J. and J.F. Beaudoin, Drag and Lift Reduction of a 3D Bluff Body Using Flaps. Experiments in Fluid 10.1007/s00348-007-0392-1, 2008.
25. Leuschen, J. and K.R. Cooper, Full-Scale Wind Tunnel Test of Production and Prototype, Second-Generation Aerodynamic Drag-Reduction Devices for Tractor-Trailers SAE International 2006-01-3456, 2006.
26. Masaru Koike, T.N., Naoki Hamamoto, Research on Aerodynamic Drag Reduction by Vortex Generators, 2004: Mitsubishi Motors Technical Review.
27. Aider, J.L.B., J. F. Wesfreid, J. E., Drag and Lift Reduction of a 3D Bluff-Body Using active Vortex Generators. Experiments in Fluid 10.1007/s00348-009-0770-y, 2009.
28. Duriez, T.A., J. L. Wesfreid, J. E., Base Flow Modification by Streamwise Vortices. Application of the Control of the Separation Flow FEDSM2006-98541, pp. 791-796; 6 pages ASME, 2006.

29. Roy, S. and P. Srinivasan, External Flow Analysis of a Truck for Drag Reduction. SAE International 2000-01-3500, 2000.
30. Feng, Y.W., S. Zhang, L. Xu, L. Fu, J., Study on Influence of Mesh Parameters on Vehicle Aerodynamic Drag Coefficient 2008-01-0100. 2008.
31. Christopher J. Roy, L.J.D., Jeffrey L. Payne, and Frederick G. Blotter, Bluff-Body Flow Simulations Using Hybrid RANS/LES. AIAA Paper 2003-3889, 2003.
32. Khaleghi, B.Z., Koromilas, S. Balkanyi, C. Luis, S. R. Bernal, p. Laccarino, G. Moin, p., Experimental and Computational Study of Unsteady Wake Flow Behind a Bluff Body with a Drag Reduction Device. Vehicle Aerodynamic Design and Technology 2001-01B-207, 2001.
33. McCallen, R.C.S., K. Ortega, J. DeChant, L. Hassan, B. Roy, C. Pointer, W.D. Browand, F. Hammache, M. Hsu, T.Y. Leonard, A. Rubel, M. Chatalian, P. Englar, R. Ross, J. Satran, D. Heineck, J. T. Walker, S. Yaste, D. Storms B., DOE's Effort to Reduce Truck Aerodynamic Drag-Joint Experiments and Computations Lead to Smart Design. 2004.
34. Huminic, A. and A. Chiru, On CFD Investigations of Vehicle Aerodynamics with Rotating Wheels' Simulation. SAE International 2006-01-0804, 2006.
35. Verzicco, R.F., M. Iaccarino, G. Khalighi, B. Moin, P., Large Eddy Simulation of a Road Vehicle with Drag-Reduction Devices. AIAA, 2002. 40.
36. Ortega, J.D., M. McCallen, T. Salari, R., Computational Simulation of a Heavy Vehicle Trailer Wake. The Aerodynamics of Heavy Vehicles: Trucks, Buses and Trains, 2002. Volume 19, 2004, pp 219-233.
37. McCallen, R.C., R. Hsu, J. Browand, F. Hammache, M. Leonard, A. Brady, M. Salari, K. Rutledge, W. Ross, J. Storms, B. Heineck, J. Driver, D. Bell, J. Zilliac, G., Aerodynamic Drag of Heavy Vehicles (Class 7-8) Simulation and Benchmarking. SAE International 2000-01-2209, 2000.
38. Pankajakshan, R.S., K. Mitchel, B. J. Whitfield, D. L., CFD Simulation of Class 8 Trucks. SAE International 2007-01-4293, 2007.
39. Josh, B.R., C. Hartfield, R., Aerodynamic Optimization for Freight Trucks Using Genetic Algorithm and CFD. AIAA 2008-323, 2009.
40. Gilkeson, C.A., Toropov, V.V., Thompson, H.M, Wilson, M.C.T, Foxley, N. A. and Gaskell, P. H., Aerodynamic Shape Optimization of a Low Drag Fairing for Small Livestock Trailers. AIAA 2008-5903, 2008.
41. Lietz, R.L., Vehicle Aerodynamic Shape Optimization. SAE International 2011-01-0169, 2011.
42. Chen, Q.W., H. Zhou, J. liu, J., A Combined Digital and Experimental Process for the Aerodynamic Optimization of the New Lavida. SaE International 2013-01-0204, 2013.
43. Bizzarrini, N.G., F. Coiro, D. P., Genetic Algorithm in wind Turbine Airfoil Design, in EWEA 2011, , E.R.C.o.t.N. ECN, Editor 2011, Europe's Premier Wind Energy Event: Brussels, Belgium.

44. Karpowitz, D., Bezier Curve Fitting Method for Existing Turbine Blade Design. *Journal of Applied Engineering Mathematics*, 2005. Volume 3.
45. Sederberg, T.W., Computer Aided Geometric Design course notes, 1997, Department of Computer Science Brigham Young University.
46. Giannakoglou, K.C., A Design Method For Turbine Blades Using Genetic Algorithms On Parallel Computers. *ECCOMAS 98*, 1998.
47. Giannakoglou, K.C., Designing Turbomachinery Blades Using Evolutionary Methods. *ASME 1999 International Gas Turbine and Aeroengine Congress and Exhibition 99-GT-181*, 1999(Presented at the International Gas Turbine & Aeroengine Congress & Exhibition Indianapolis).
48. Pal, S.B., P. K. Abraham, A., Face recognition using interpolated Bezier curve based representation. *Information Technology: Coding and Computing*, 2004. *Proceedings. ITCC 2004. International Conference on*, 2004. 1: p. 45-49 Vol.1.
49. Mohammadi, B.P., O. Mohammadi, B. Pironneau, O., *Applied shape optimization for fluids*. Vol. 28. 2001: Oxford University Press Oxford.
50. Nadarajah, S. and A. Jameson, A comparison of the continuous and discrete adjoint approach to automatic aerodynamic optimization. *AIAA-2000-0667*, 2000. 667: p. 2000.
51. Antony, J.S., S. Luigi, M., An Unstructured Adjoint Method for Transonic Flow. *16th AIAA Computational Fluid Dynamics Conference 2003-3955*, 2003.
52. Hinterberger, C. and M. Olesen, Industrial application of continuous adjoint flow solvers for the optimization of automotive exhaust systems. *CFD & Optimization*, Antalya, Turkey, 2011.
53. Othmer, C., Adjoint methods for car aerodynamics. *Journal of Mathematics in Industry* 2190-5983-4-6, 2014. 4(1): p. 6.
54. Poloni, C., Multi Objective Aerodynamic Optimisation by Means of Robust and Efficient Genetic Algorithm, in *Recent Development of Aerodynamic Design Methodologies*, K. Fujii and G. Dulikravich, Editors. 1999, Vieweg+Teubner Verlag. p. 1-24.
55. Quagliarella, D. and A. Della Cioppa, Genetic algorithms applied to the aerodynamic design of transonic airfoils. *Journal of Aircraft*, 1995. 32(4): p. 889-891.
56. Toropov, V.V., Simulation approach to structural optimization. *Structural optimization*, 1989. 1(1): p. 37-46.
57. Narducci, R.G., B. Valorani, M. Dadone, A. Haftka, RT., Optimization methods for non-smooth or noisy objective functions in fluid design problems. *AIAA paper*, 1995. 1648.
58. Baysal, O. and M.E. Eleshaky, Aerodynamic Sensitivity Analysis Methods for the Compressible Euler Equations. *Journal of Fluids Engineering*, 1991. 113(4): p. 681-688.
59. Borggaard, J.B., J. Cliff, E. Gunzburger, M., Sensitivity calculations for a 2D, inviscid, supersonic forebody problem. *Identification and control of systems governed by partial differential equations*, 1993: p. 14-24.
60. Soto, O. and R. Löhner, CFD shape optimization using an incomplete-gradient adjoint formulation. *International Journal for Numerical Methods in Engineering*, 2001. 51(6): p. 735-753.

61. Pironneau, O., On optimum profiles in Stokes flow. *Journal of Fluid Mechanics Digital Archive*, 2006. 59(01): p. 117-128.
62. Reuther, J.J., A. Martinelli, L. Saunders, D., Aerodynamic shape optimization of complex aircraft configurations via an adjoint formulation. *AIAA AIAA, Aerospace Sciences Meeting and Exhibit*, 34th, Reno, NV, Jan. 15-18,, 1996.
63. Jemcov, A.S., D. Sideroff, C., Application of Time Symmetry Preserving Adjoint Solver in External Car Aerodynamics. *SAE International 2014-01-0412*, 2014.
64. Anderson, W.K. and V. Venkatakrisnan, Aerodynamic design optimization on unstructured grids with a continuous adjoint formulation. *Computers & Fluids*, 1999. 28(4–5): p. 443-480.
65. Othmer, C., A continuous adjoint formulation for the computation of topological and surface sensitivities of ducted flows. *International Journal for Numerical Methods in Fluids*, 2008. 58(8): p. 861-877.
66. Giannakoglou, K. and D. Papadimitriou, Adjoint Methods for Shape Optimization, in *Optimization and Computational Fluid Dynamics*, D. Thévenin and G. Janiga, Editors. 2008, Springer Berlin Heidelberg. p. 79-108.
67. Jameson, A., Aerodynamic shape optimization using the adjoint method, in *Lectures at the Von Karman Institute, Brussels2003*.
68. Löhner, R.S., O. Yang, Chi., An adjoint-based design methodology for CFD optimization problems. *AIAA-030299*, 2003.
69. Othmer, C.V.A., Wolfsburg., CFD Topology and Shape Optimization with Adjoint Methods, in *13. Internationaler Kongress Berechnung und Simulation2006: Fahrzeugbau Wu rzburg,*.
70. Schneider, R., Applications of the discrete adjoint method in computational fluid dynamics, 2006, The University of Leeds.
71. Nielsen, E.J. and W.L. Kleb, Efficient construction of discrete adjoint operators on unstructured grids using complex variables. *AIAA Journal*, 2006. 44(4): p. 827-836.
72. Xu, S.J., W. Müller, J.D., CAD-based shape optimisation with CFD using a discrete adjoint. *International Journal for Numerical Methods in Fluids*, 2014. 74(3): p. 153-168.
73. Giles, M.G., D. Duta, M., Using automatic differentiation for adjoint CFD code development, 2005: Oxford University Computing Laboratory.
74. Union, P.O.o.t.E. FLOWHEAD Result In Brief. 2015 [cited 2015 10/02/2015]; Available from: http://cordis.europa.eu/result/rcn/87544_en.html.
75. Müller, J. FLOWHEAD, Fluid Optimisation Workflows for Highly Effective Automotive Development Processes. 2015 [cited 2015 10/02/2015]; Available from: <http://flowhead.sems.qmul.ac.uk/>.
76. http://cordis.europa.eu/result/rcn/87544_en.html. 2015 [cited 2015 10/02/2015].
77. Lorriaux, E.B., N.Monnoyer, F., Aerodynamic optimization of railway motor coaches, in *Laboratoire de Mécanique et d’Energétique*, Université de Valenciennes: France.
78. Krajnović, S., Shape optimization of high-speed trains for improved aerodynamic performance. *Proceedings of the Institution of*

- Mechanical Engineers, Part F: Journal of Rail and Rapid Transit, 2009. 223(5): p. 439-452.
79. Fan, J.E., J. Thompson, H. M. Toropov, V. V. Kapur, N. Copley, D. Mincher, A., Computational fluid dynamic analysis and design optimization of jet pumps. *Computers & Fluids*, 2011. 46(1): p. 212-217.
 80. Khan, M.A.N., C. Toropov, V. V., Development of a numerical optimization approach to ventilation system design to control airborne contaminant dispersion and occupant comfort. *Building Simulation*, 2012. 5(1): p. 39-50.
 81. Schlichting, H.G., K. Gersten, K., *Boundary-Layer Theory*. 2000: MacGraw-Hill.
 82. Bixler, B.P., D. and Fairhurst, F., The accuracy of computational fluid dynamics analysis of the passive drag of a male swimmer. *Sports Biomechanics*, 2007. 6(1): p. 81-98.
 83. Vakil, A. and S.I. Green, Drag and lift coefficients of inclined finite circular cylinders at moderate Reynolds numbers. *Computers & Fluids*, 2009. 38(9): p. 1771-1781.
 84. Faber, T.E., *Fluid Dynamics for Psycists*. 1995, New York City: Cambridge University Press.
 85. <http://kahuna.sdsu.edu/>. *Vehicle Aerodynamics*. [cited 2014 07/05/2014].
 86. Barlow, J.B. and W.H. Rae, *Low-speed wind tunnel testing*. 1999: Wiley.
 87. Richardson L. F, *Weather Prediction by Numerical Progress*. 1922: Cambridge University Press.
 88. Lesieur, M., *Turbulence in Fluids* 4th ed. 2008: Springer
 89. Reynolds, A.J., *Turbulent Flows in Engineeing*, John Wiley & Sons. 1th ed. 1974.
 90. Tennekes, H.L., J. L., *A first Course in Turbulence*. 1st ed. 1971: MIT Press.
 91. Versteeg H. K and Malalasekera W, *An Introduction to Computational Fluid Dynamics: The Finite Volume Method*, , ed. n. Edition. 2007: Pearson Prentice Hall.
 92. Massey, B. and J.W. Smith, *Mechanics of Fluids*. 7th ed. 1998: Stanley Thornes Ltd.
 93. Ansys, *Ansys Workbench*, 2014.
 94. Barand, R.H., *Aircraft Flight: A Description of the Physical Principles of Aircraft Flight*. 2nd ed. 2000: Longman.
 95. Fox, R.W. and A.T. McDonald, *Introduction to Fluid Mechanics*. 4th ed. 1992: John Wiley & Sons.
 96. Morris, M.D. and T.J. Mitchell, Exploratory designs for computational experiments. *Journal of Statistical Planning and Inference*, 1995. 43(3): p. 381-402.
 97. Bates, S.S., J. Toropov, V., Formulation of the Optimal Latin Hypercube Design of Experiments Using a Permutation Genetic Algorithm, in *45th AIAA/ASME/ASCE/AHS/ASC Structures, Structural Dynamics & Materials Conference*. 2004, American Institute of Aeronautics and Astronautics.
 98. Benson, T. NASA. 2014 [cited 2014 15/02/2014]; Available from: <http://www.grc.nasa.gov/WWW/k-12/airplane/drag1.html>.

99. Barnes, W. and McCormick., Aerodynamics, Aeronautics, and flight Mechanics. 1979, John Wiley & Sons: New York. p. 24.
100. Barnard, R.H., Road Vehicle Aerodynamic Design, An Introduction. 2nd ed. 2001: Longman.
101. Samareh, J.A., Survey of Shape Parameterization Techniques for High-Fidelity Multidisciplinary Shape Optimization. AIAA Journal, 2001. 39(5): p. 877-884.
102. Gilkeson, C.A.T., V. V. Thompson, H. M. Wilson, M. C. T. Foxley, N. A. Gaskell, P. H., Dealing with numerical noise in CFD-based design optimization. Computers & Fluids, 2014. 94: p. 84-97.
103. Cooper, K.R., Commercial Vehicle Aerodynamic Drag Reduction: Historical Prospective as a Guide, United Engineering Foundation Conference on the Aerodynamic of Heavy Vehicles: Trucks, Buses and Trains 2002: Springer.
104. Gary, P.K., development of Container-Monted Devices for Reducing the Aerodynamic Drag of Commercial Vehicles Wind Engineering and Industrial Aerodynamics 1981. 9: p. 113-124.
105. Chawat, F.A., Wind-Tunnel Study of an Add-on Streamlining Bubbles on the Aerodynamics of Utility Box-Trailers. Wind Engineering and Industrial Aerodynamics, 1983. 11: p. 431-440.
106. Mair, A.W. and D.T. Wong, Boat-tailed Afterbodies of Square Section As Drag-Reduction Devices. Wind Engineering and Industrial Aerodynamics, 1983. 12: p. 229-235.
107. Ferziger, J.H. and M. Perić, Computational Methods for Fluid Dynamics. 2002: Springer London, Limited.
108. Hirsch, C., Numerical Computation of Internal and External Flows, Butterworth-Heinemann. 2nd ed. 2007.
109. Durbin, P.A. and G. Medic, Fluid Dynamics with a Computational Perspective, ed. t. Edition. 2007: Cambridge University Press.
110. Wilcox, D.C., Turbulence Modeling for CFD. Vol. Vol. 2, pp. 103-217. 1994: DCW Industries, Incorporated.
111. Pty, L.A. Inflation Layer Meshing in ANSYS. 2014 [cited 2014 24/June]; Inflation Layer Meshing in ANSYS]. Available from: <http://www.computationalfluidynamics.com.au/tips-tricks-inflation-layer-meshing-in-ansys/>.
112. Tu, J.Y., G.H. Liu, C., Computational Fluid Dynamics: A Practical Approach. 2007: Elsevier Science.
113. Pty, L.A. Wall Functions and Y+ requirements. 2014 [cited 2014 24/June]; Wall Functions and Y+ requirements]. Available from: <http://www.computationalfluidynamics.com.au/tips-tricks-turbulence-wall-functions-and-y-requirements/>.
114. Versteeg, H.K. and W. Malalasekera, An Introduction to Computational Fluid Dynamics: The Finite Volume Method. 2007: Pearson Education Limited.
115. Pty, L.A. Selection of wall functions and Y+ to best capture the Turbulent Boundary Layer. 2014 [cited 2014 24/June]; Selection of wall functions and Y+ to best capture the Turbulent Boundary Layer]. Available from: <http://www.computationalfluidynamics.com.au/turbulence-part-3-selection-of-wall-functions-and-y-to-best-capture-the-turbulent-boundary-layer/>.

116. Versteeg, H.K. and W. Malalasekera, Computational Fluid Dynamics. 2007: Pearson. 503.
117. George, W.K., Lectures in Turbulence for the 21st Century, 2005, Department of Thermo and Fluid Engineering, Chalmers University of Technology, Göteborg, Sweden: http://www.turbulence-online.com/Publications/Lecture_Notes/Turbulence_Lille/TB_16January2013.pdf. p. 64.
118. Moeng, C.-H., Large Eddy Simulation.
119. MIRA. UK - Quatro Park. 2014 [cited 2014 10/06/2014]; Available from: <http://www.mira.co.uk/contact/offices/mira-quatro-park>.
120. Hucho, W.H., Aerodynamics of Road Vehicles: From Fluid Mechanics to Vehicle Engineering. 1998: Society of Automotive Engineers, Incorporated.
121. Online, C. Convergence. 215 [cited 2015 10/02/2015]; Available from: <http://www.cfd-online.com/Forums/fluent/90281-convergence.html>.
122. Pty, L.A. Convergence and Mesh Independence Study. 2015 [cited 2015 10/02/2015]; Available from: <http://www.computationalfluidynamics.com.au/convergence-and-mesh-independent-study>.
123. Cavazzuti, M., Optimization Methods: From Theory to Scientific Design and Technological Aspects in Mechanics. 2012: Springer Berlin Heidelberg.
124. Rao, S.S. and S. Rao, Engineering optimization: theory and practice. 2009: John Wiley & Sons.
125. Dorigo, M. and T. Stützle, Ant Colony Optimization. 2004: Bradford Book.
126. Bellman, R.E., Dynamic Programming. 2003: Dover Publications.
127. Hopfield, J. and D. Tank, Computing with neural circuits: a model. Science, 1986. 233(4764): p. 625-633.
128. Toropov, V.S., U. Sahai, A. Jones, R. Zeguer, T. Design optimization and stochastic analysis based on the moving least squares method. in 6th World Congress of Structural and Multidisciplinary Optimization, Rio de Janeiro, paper. 2005. Citeseer.
129. Dantzig, G.B. and M.N. Thapa, Linear Programming 1: 1: Introduction. 1997: Springer.
130. Holland, J.H., Adaptation in natural and artificial systems: an introductory analysis with applications to biology, control, and artificial intelligence. 1975: University of Michigan Press.
131. Kirkpatrick, S.G., C. D. Vecchi, M. P., Optimization by Simulated Annealing. Science, Number 4598, 13 May 1983, 1983. 220, 4598: p. 671-680.
132. Kennedy, J. and R. Eberhart. Particle swarm optimization. in Neural Networks, 1995. Proceedings., IEEE International Conference on. 1995. Perth, WA, Australia: IEEE.
133. Deb, K., Multi-Objective Optimization Using Evolutionary Algorithms. 2001: Wiley.
134. Wind Tunnels at NASA Ames, 2014: Moffett Field, California.
135. Hoerner, S.F. and H.V. Borst, Fluid-dynamic lift: practical information on aerodynamic and hydrodynamic lift. 1985: L.A. Hoerner.
136. Renault, PSA Open Wind Tunnels, 2014: PARIS.

137. Shmoys, D.B. and C. Swamy, Stochastic Optimization is (Almost) as easy as Deterministic Optimization, in Proceedings of the 45th Annual IEEE Symposium on Foundations of Computer Science 2004, IEEE Computer Society. p. 228-237.
138. Toropov, V.K., F. Markine, V. Barkalov, K. Gergel, V. P. De Doer, H. Refinements in the multi-point approximation method to reduce the effects of noisy structural responses. in Proceedings 6th AIAA/USAF/NASA/ISSMO symposium on multidisciplinary analysis and optimization. 1996. AIAA Bellevue, WA.
139. Markine, V.B., K. Gergel, V. P., An Optimum Design Procedure Based On Multipoint Approximations And A Global Optimisation Method, in 6th World Congresses of Structural and Multidisciplinary Optimization 2005: Rio de Janeiro, Brazil.
140. National Research Council Canada, 2014: Ottawa, Ontario. p. wind tunnel in NRC.
141. Mitchell, M., An Introduction to Genetic Algorithms. 1998: Bradford Books.
142. Sivanandam, S.N. and S.N. Deepa, Introduction to Genetic Algorithms. 2007: Springer Berlin Heidelberg.
143. Back, T., Evolutionary Algorithms in Theory and Practice : Evolution Strategies, Evolutionary Programming, Genetic Algorithms. 1995: Oxford University Press, USA.
144. Janković, M. Genetic Algorithms. 2015 [cited 2015 30/02/2015]; Available from: <http://www.codeproject.com/Articles/26203/Genetic-Algorithm-Library#Populations5>.
145. Eiben, A.E. and J.E. Smith, Introduction to Evolutionary Computing. 2003: Springer.
146. United States. National, A., A. Space, and K.L. Suder, Blockage development in a transonic, axial compressor rotor. 1997, [Washington, D.C. : Springfield, Va.: National Aeronautics and Space Administration ; National Technical Information Service, distributor.
147. Polynkin, A. and V. Toropov, Mid-range metamodel assembly building based on linear regression for large scale optimization problems. Structural and Multidisciplinary Optimization, 2012. 45(4): p. 515-527.
148. Khatir, Z.T., H. Kapur, N. Toropov, V. Paton, J., Multi-Objective Computational Fluid Dynamics (CFD) Design Optimisation in Commercial Bread-Baking, in Proceedings of the 12th UK National Heat Transfer Conference–UKHTC-12, August 30-September 1, 2011, Leeds 2011: Leeds.
149. Powell, M.J.D., Direct search algorithms for optimization calculations. Acta Numerica, 1998. 7(-1): p. 287-336.
150. Zal, P. Automobile Catalog. 2013 10/07/2013; Available from: <http://www.automobile-catalog.com>.
151. Howell, J.a.H., D., The Influence of Ground Simulation on the Aerodynamics of a Simple Car Model. SAE Technical Paper 970134, 1997.
152. Olson, M.a.U.S., Aerodynamics of Trucks in Wind Tunnels: The Importance of Replicating Model Form, Model Detail, Cooling System and Test Conditions. SAE Technical Paper 920345, 1992.

153. Keynes, M. The Van Factory. 2014 [cited 2014 20/04/2014]; Vaxhual Vivaro]. Available from:
<http://thevanfactory.co.uk/searchlist.php?make=Vauxhall>.
 154. Nelder, J.A. and R. Mead, A Simplex Method for Function Minimization. *The Computer Journal*, 1965. 7(4): p. 308-313.
 155. Ansys_13.0. 2012 [cited 2012 03/05/2012]; Ansys 13.0]. Available from:
<http://www.ansys.com/Products/Workflow+Technology/ANSYS+Workbench+Platform>.
 156. Eastmann N. Jacobs, K.E.W., Robert M. Pinkerton, The characteristics of 78 related airfoil sections from tests in the variable density wind tunnel, in NACA Report No. 4601948.
 157. HyperWorks_10. 2012 03/05/2012; Available from:
<http://www.altairhyperworks.co.uk/?AspxAutoDetectCookieSupport=1>.
 158. Fluent_6.3. 2012 [cited 2012 03/05/2012]; Available from:
<http://www.ansys.com/Products/Simulation+Technology/Fluid+Dynamics/ANSYS+Fluent>.
-